

# Magnetic circular dichroism spectroscopy as a probe of the geometric and electronic structure of non-heme ferrous enzymes

Edward I. Solomon \*, Elizabeth G. Pavel, Kelly E. Loeb,  
Cecelia Campochiaro

*Department of Chemistry, Stanford University, Stanford, CA 94305, USA*

Received 11 January 1995; in revised form 27 February 1995

## Contents

Abstract	370
1. Introduction	371
2. Background	374
2.1. Bioinorganic enzymology	374
2.2. Physical methods	382
3. Methodology	385
3.1. MCD theory	386
3.1.1. Circular dichroism spectroscopy	388
3.1.2. Magnetic circular dichroism spectroscopy	389
3.1.3. Experimental considerations	394
3.2. Ligand field theory of excited-state d-orbital splittings	395
3.3. MCD saturation magnetization: determination of ground-state spin Hamiltonian parameters	401
3.3.1. Effective Kramers doublet	401
3.3.1.1. xy-Polarization effects	401
3.3.1.2. z-Polarization effects	402
3.3.1.3. Linear, temperature-independent $\mathcal{B}$ -term effects	404
3.3.2. Population of excited states for negative zero-field splitting	405
3.3.3. Negative zero-field splitting: non-Kramers doublet	407
3.3.3.1. xy-Polarization and rhombicity effects	408
3.3.3.2. z-Polarization effects	410
3.3.3.3. Linear, temperature-independent $\mathcal{B}$ -term effects	412
3.3.3.4. Population of excited states	413
3.3.4. Positive zero-field splitting	414
3.3.4.1. xy-Polarization effects in the axial limit	414
3.3.4.2. z-Polarization effects in the axial limit	416
3.3.4.3. Rhombicity effects	419

\* Corresponding author.

3.4. Ligand field origin of spin Hamiltonian parameters . . . . .	421
3.4.1. Six-coordinate geometry . . . . .	421
3.4.1.1. Distorted octahedral, $^5B_{2g}$ or $^5A_1$ ground state . . . . .	423
3.4.1.2. Distorted octahedral, $^5E_g$ ground state . . . . .	423
3.4.2. Five-coordinate geometry . . . . .	428
3.4.2.1. Square pyramidal, strong- and weak-axial . . . . .	428
3.4.2.2. Trigonal bipyramidal . . . . .	429
3.4.3. Four-coordinate geometry . . . . .	430
3.4.3.1. Distorted tetrahedral (flattened), $^5A_1$ ground state . . . . .	431
3.4.3.2. Distorted tetrahedral (elongated), $^5B_1$ ground state . . . . .	432
3.4.3.3. Square planar . . . . .	433
3.4.4. FeSOD revisited . . . . .	434
4. Structure/function applications to mononuclear non-heme ferrous enzymes . . . . .	434
4.1. Phthalate dioxygenase (PDO) . . . . .	435
4.2. Lipxygenases (LOs) . . . . .	439
4.3. Bleomycin (BLM) . . . . .	445
5. Concluding remarks . . . . .	453
Acknowledgments . . . . .	455
References . . . . .	455

## Abstract

Mononuclear non-heme iron active sites are present in a variety of enzymes involved in a wide range of important biological functions requiring dioxygen. These include superoxide dismutases, oxidases, extra- and intradiol dioxygenases, *cis*-dihydroxylases, pterin- and  $\alpha$ -ketoglutarate-dependent hydroxylases, lipxygenases, and bleomycin. Both the ferrous and ferric oxidation states are involved in catalysis for different enzymes in this class, and substrate- and oxygen-bound intermediates have been observed. Much less is known about the active sites in these enzymes relative to the heme systems as the non-heme iron centers are less spectroscopically accessible, particularly at the ferrous oxidation level. The application of magnetic circular dichroism (MCD) spectroscopy has greatly advanced the level of understanding in these systems as this technique allows the direct observation of the ferrous  $d \rightarrow d$  ligand field transitions, which are generally obscured by solvent and protein vibrations in optical absorption spectroscopy owing to the weak extinction coefficients and are often electron paramagnetic resonance silent due to relatively large ground-state sublevel splittings and fast relaxation times. The energies of the  $d \rightarrow d$  transitions give the splitting of the excited-state  $e_g$  orbitals which can be correlated with the coordination number and geometry at the ferrous center. In addition, the ground states of high-spin ferrous complexes are described as an  $S=2$  spin manifold which undergoes axial zero-field splitting into  $M_S = \pm 2, \pm 1, 0$  components separated by  $3D$  and  $D$ , respectively. The non-Kramers  $M_S = \pm 2$  doublet is lowest in energy for  $D < 0$ , and is further rhombically split by an amount  $\delta$  in the absence of a magnetic field. The unusual variable-temperature variable-field MCD saturation behavior observed for such systems can be interpreted by including the effects of  $\delta$  as well as  $z$ -polarization, linear  $B$ -terms, and the population of low-lying excited states. The non-degenerate  $M_S = 0$  state is lowest in energy for  $D > 0$  and the resulting MCD saturation behavior can be analyzed by including the effects of off-axis Zeeman terms and  $z$ -polarized electronic transitions. The spin Hamiltonian parameters obtained through analysis of the variable-temperature variable-field

MCD saturation data are further interpreted in terms of the ligand field splitting of the ground-state  $t_{2g}$  set of d-orbitals. This MCD methodology has been applied to several biologically relevant mononuclear non-heme ferrous systems to directly probe the active site geometric and electronic structures and to gain mechanistic information about their catalytic cycles. MCD spectroscopy has been used to study the native ferrous active site of phthalate dioxygenase and its interaction with substrate and exogenous ligands, which has previously been difficult to study due to the additional presence of a  $[2Fe-2S]$  Rieske cluster. The native form of soybean lipoxygenase exists as a mixture of species in solution that has been defined through the application of CD and MCD spectroscopies. This MCD methodology has also been used to elucidate the nature of the ferrous active site in bleomycin, which represents an important deviation from mononuclear non-heme iron enzymes in that it exhibits low-energy charge transfer transitions and performs chemistry similar to heme systems. The MCD methodology presented in this review has been employed to obtain molecular level insight into the catalytic mechanisms of these important enzyme systems and to understand the differences in active site geometric and electronic structures which relate to differences in oxygen reactivity.

**Keywords:** Magnetic circular dichroism spectroscopy; Non-heme ferrous enzymes; Geometric structure; Electronic structure

---

## 1. Introduction

Iron is one of the most abundant elements found in the earth's core, is present throughout the biosphere, and is distributed in a variety of proteins which can be classified by their biological functions: iron transport, electron transfer, oxygen binding, oxygen activation, and multi-electron reduction. The stable oxidation state is  $Fe^{3+}$ , which is difficult to store in vivo because it reacts to form an insoluble  $Fe(III)$  oxide polymer that is toxic to cells. Examples of iron-containing proteins which have evolved to overcome this difficulty are ferritin [1,2], a storage protein of iron metabolism found in the liver and spleen, and transferrins [3], beta globulins in blood plasma capable of combining with ferric ions and transporting iron in the body. Electron transfer and storage are accomplished by a class of proteins which contain iron–sulfur clusters [4]. Rubredoxin is an electron transfer protein which contains one iron tetrahedrally coordinated to four cysteine sulfurs. Electron storage is accomplished by  $[2Fe-2S]$  plant ferredoxins, in which the two iron atoms are tetrahedrally coordinated to four sulfur atoms (two bridging sulfides and two cysteine sulfurs) and Rieske centers, which differ from the plant ferredoxins in that one of the two tetrahedrally coordinated irons is ligated to two histidine nitrogens.  $[4Fe-4S]$  ferredoxins are low molecular weight proteins which are also involved in oxidation/reduction reactions in substrate metabolism and have distorted cubane geometries. The most studied class of iron-containing proteins are the heme proteins. These systems are responsible for oxygen binding, oxygen activation, and multi-electron reduction and include such examples as hemoglobin, cytochrome P-450, prostaglandin synthase, cytochrome oxidase, and catalase [5]. Hemoglobin is a respiratory pigment capable of reversibly binding and transporting oxygen. Prostaglandin synthase is a dioxygenase that catalyzes the insertion of two atoms of oxygen from

dioxygen into substrate [6]. Cytochrome P-450 activates dioxygen for monooxygenase chemistry and is thought to involve an oxo-ferryl intermediate [7]. Cytochrome oxidase acts as a proton pump across cell membranes requiring four electrons from cytochrome *c* to reduce molecular oxygen to water [8,9]. Catalase catalyzes the dismutation of the toxic peroxide byproduct to oxygen and water in the cells of nearly all aerobic organisms. It is important to realize that there are also large classes of non-heme iron enzymes which perform reactions similar to those of the heme enzymes involving oxygen binding, activation, four-electron reduction, and disproportionation. These can be subdivided into binuclear and mononuclear classes. For the binuclear proteins, the nature of the oxo or hydroxy bridge appears to play a key role in the catalytic mechanisms [10,11]: hemerythrin is an oxygen carrier protein analogous to hemoglobin, methane monooxygenase catalyzes the conversion of methane to methanol, and ribonucleotide reductase reduces ribonucleotides to deoxyribonucleotides in the first committed step in DNA synthesis. Finally, the mononuclear non-heme iron enzymes, which are the focus of this review, are an extensive class which do not have the dominant structural features of the above proteins (iron–sulfur bonds, the porphyrin ligand, or oxo bridges) and are thus the least well understood. Several recent reviews of non-heme iron enzymes are given in Refs. [12–14].

Mononuclear non-heme iron active sites are present in a variety of enzymes involved in a wide range of important biological functions requiring dioxygen. These enzymes are classified according to the types of reactions catalyzed: dismutation, oxidation, monooxygenation, dioxygenation, hydroperoxidation, and DNA cleavage. The dioxygenases may be further subdivided into extra- and intradiol dioxygenases, *cis*-dihydroxylases, and pterin- and  $\alpha$ -ketoglutarate- ( $\alpha$ -KG-) dependent hydroxylases. The latter two systems incorporate one oxygen atom from dioxygen into substrate and one into the organic cofactor and are thus formally dioxygenases. Specific enzyme reactions from each class are given in Fig. 1. Briefly, iron superoxide dismutase (FeSOD) is one of three superoxide dismutases that catalyze the dismutation of superoxide ions to oxygen and hydrogen peroxide [15]. Isopenicillin N synthase (IPNS) is an oxidase which is unusual in that it catalyzes the four-electron oxidative double ring closure of its substrate [16]. Monooxygenase activity is exhibited by  $\omega$ -hydroxylase ( $\omega$ H), but the available information is limited owing to difficulty in isolating the protein in sufficient quantities for detailed study [17]. Several different types of dioxygenases are involved in the bacterial degradation of aromatic rings. The final ring cleavage step in the degradation of aromatic rings, breakdown of a catechol, is catalyzed by the extra- and intradiol dioxygenases (e.g., catechol 2,3-dioxygenase (2,3-CTD) and protocatechuate 3,4-dioxygenase (3,4-PCD), respectively) which exhibit fundamental differences in structure and reactivity [18,19]. Prior to this reaction, conversion of an unactivated aromatic to the *cis*-dihydrodiol is required and is catalyzed by the *cis*-dihydroxylase phthalate dioxygenase (PDO) and related enzymes [20]. Phenylalanine hydroxylase (PAH), one of three pterin-dependent hydroxylases, catalyzes the hydroxylation of phenylalanine to tyrosine [21]. Clavaminic synthase (CS) is an  $\alpha$ -ketoglutarate-dependent hydroxylase which can perform ring closure as well as hydroxylation chemistry depending on substrate

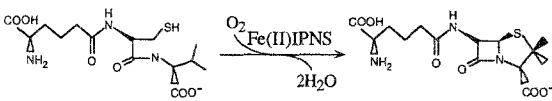
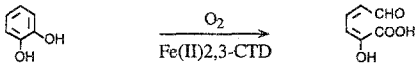
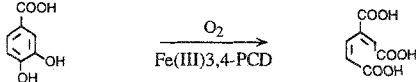
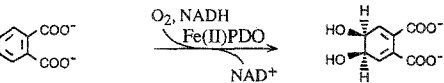
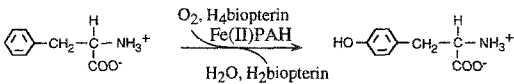
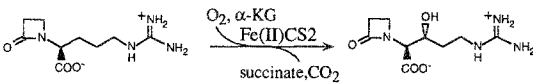
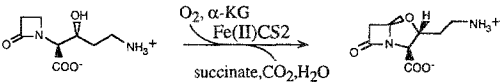
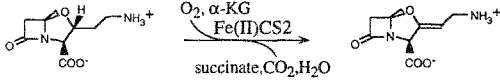
Oxygen Reactivity	Representative Enzyme	Reaction Catalyzed	
Dismutation	superoxide dismutase	$2 \text{O}_2^- + 2 \text{H}^+ \xrightleftharpoons{\text{Fe(II,III)SOD}} \text{H}_2\text{O}_2 + \text{O}_2$	
Oxidation	isopenicillin N synthase		
Monooxygenation	$\omega$ -hydroxylase	$\text{RCH}_3 \xrightarrow[\text{Fe(II)\omega H}]{\text{O}_2} \text{RCH}_2\text{OH}$	
Extradiol Dioxygenation	catechol 2,3-dioxygenase		
Intradiol Dioxygenation	protocatechuate 3,4-dioxygenase		
cis-Hydroxylation	phthalate dioxygenase		
Pterin-Dependent Hydroxylation	phenylalanine hydroxylase		
$\alpha$ -Ketoglutarate-Dependent Hydroxylation & Oxidative Ring Closure	clavamate synthase		
			
			
Hydroperoxidation	lipoxygenases	$\text{R}-\text{CH}=\text{CH}-\text{CH}=\text{CH}-\text{R} \xrightarrow[\text{Fe(III)LO}]{\text{O}_2} \text{HOOC}-\text{CH}(\text{R})-\text{CH}=\text{CH}-\text{CH}=\text{CH}-\text{R}$	
DNA Cleavage	bleomycin	$\text{DNA} \xrightarrow[\text{Fe(II)BLM}]{\text{O}_2} \text{base propenals}$	

Fig. 1. Classes of oxygen reactivity exhibited by mononuclear non-heme iron enzymes. Representative enzymes and the reactions they catalyze are illustrated for each class.

[22]. The lipoxygenases (LOs) catalyze the hydroperoxidation of *cis,cis*-1,4-pentadiene-containing fatty acids [23]. Bleomycin (BLM) is a non-heme iron glycopeptide that reversibly binds and activates oxygen for hydrogen atom abstraction which is similar to heme chemistry (cytochrome P-450) [24,25] but involves a different oxygen intermediate. More detailed mechanistic and structural information for these enzymes is presented in Section 2.1.

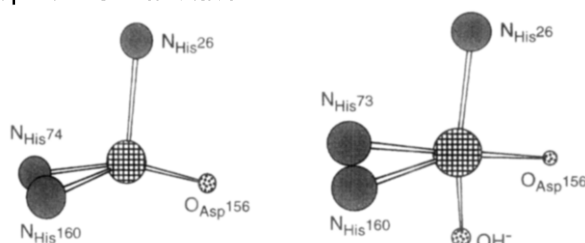
Both ferrous and ferric oxidation states have been determined to be involved in catalysis for the different mononuclear non-heme iron enzymes, and substrate- and oxygen-bound intermediates have been observed for several of these enzymes. Much less is known about the active sites in these enzymes relative to heme systems as the non-heme iron centers are less spectroscopically accessible, particularly in the ferrous oxidation state. Therefore, we have developed a methodology for the study of non-heme ferrous active sites emphasizing magnetic circular dichroism (MCD) spectroscopy to observe the ligand field excited states and variable-temperature variable-field (VTVH) MCD spectroscopy to obtain the ground-state sublevel splittings for these non-Kramers ions which often do not exhibit electron paramagnetic resonance (EPR) signals. A ligand field analysis of these data then generates the experimental d-orbital splittings of the ferrous active sites which provide geometric and electronic structural insight. This MCD methodology has then been applied to understand catalytic mechanisms on a molecular level and to discern structure/function relationships by determining how differences in geometric and electronic structure over several non-heme iron enzymes relate to differences in oxygen and substrate reactivity. This approach is developed in detail in Section 3 and applied to phthalate dioxygenase, lipoxygenases, and bleomycin in Section 4. Its application to catechol 2,3-dioxygenase [26] has been previously reviewed [12,27].

## 2. Background

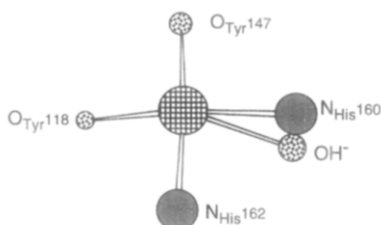
### 2.1. Bioinorganic enzymology

The dismutation of superoxide anions to peroxide and molecular oxygen is catalyzed by one of three superoxide dismutases containing either iron (FeSOD), manganese (MnSOD), or copper and zinc (Cu,Zn-SOD) [28]. FeSOD is isolated from procaryotes and is a dimer with a two-domain structure composed of 50%  $\alpha$ -helix and three strands of antiparallel  $\beta$ -sheet [28,29]. There is no change in the protein structure with the addition of iron to the active site, which contains residues from both the N- and C-terminal domains [30,31]. Fe(III)SOD has been found by X-ray crystallography to have a distorted trigonal bipyramidal structure with four endogenous protein ligands [15,28,32]. Histidine 26 coordinates axially, while histidine 74 (73), histidine 160, and aspartate 156 form the trigonal plane. The imidazole ligands bind through the NE2 and the carboxyl group binds in a monodentate fashion. Fig. (2a) illustrates that there is some controversy regarding the possible coordination of solvent in the axial fifth position. Stoddard et al. [15] propose that the fifth site is devoid of a bound water molecule or an anion and place the metal at 0.5 Å out

## (a) Superoxide Dismutase



## (b) Protocatechuate 3,4-Dioxygenase



## (c) Soybean Lipoxygenase

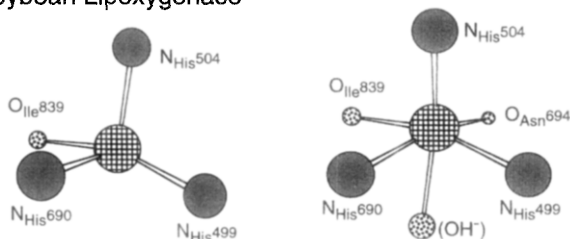


Fig. 2. Known crystallographic information about the metal coordination environments of mononuclear non-heme iron enzymes. (a) Conflicting coordination spheres of superoxide dismutase adapted from Stoddard et al. [15] (left) and Stallings et al. [28] (right). (b) Protocatechuate 3,4-dioxygenase adapted from Ohlendorf et al. [53]. (c) Conflicting metal environments of soybean lipoxygenase adapted from Boyington et al. [100] (left) and Minor et al. [101] (right).

of the plane of the trigonal ligands towards the axial histidine. Stallings et al. [28] position the metal ion in the plane of the trigonal ligands and find that solvent (hydroxide) occupies the fifth, axial coordination position on the  $\text{Fe}^{3+}$ . There is little structural change upon reduction to the ferrous state; however, the uptake of one proton per electron is observed from titration experiments which is accounted for in the Stallings et al. structure by the bound hydroxide going to water [32]. MCD and Mössbauer studies indicate that a five-coordinate structure is present in the reduced state [28], with a more square pyramidal electronic symmetry indicated from the MCD analysis [33]. Azide is an inhibitor of dismutase activity and binds to the ferric site with an increase in coordination number [28]. Superoxide binding

to the ferric center is proposed to parallel azide binding, and catalysis involves a cyclic oxidation/reduction mechanism [28,29] which ultimately results in the dismutation products.

Isopenicillin N synthase (IPNS) is a non-heme,  $\text{Fe}^{2+}$ - and oxygen-dependent enzyme found in  $\beta$ -lactam antibiotic-producing fungi and bacteria [34] which catalyzes the stepwise [35], desaturative cyclization of  $\delta$ -(L- $\alpha$ -amino adipoyl)-L-cysteinyl-D-valine (LLD-ACV) to form isopenicillin N [36], the precursor of all penicillins [37]. This key step in the biosynthesis of penicillins and cephalosporins results in the four-electron reduction of one equivalent of dioxygen to two equivalents of water [38]. The loss of four hydrogen atoms is stereospecific and the internal C–N and C–S bonds are formed with complete retention of configuration [39,40]. Although no crystal structure of this enzyme exists, information on the active site has been gained using a variety of spectroscopic techniques, including optical absorption [38], EPR [41], electron spin echo envelope modulation (ESEEM) [37], nuclear magnetic resonance (NMR) [42], Mössbauer [41], and X-ray absorption spectroscopy (XAS) [43,44]. The native enzyme is believed to be coordinated by four endogenous residues, three histidine and one monodentate aspartate, with water or hydroxide occupying the remaining sites in a distorted octahedral geometry. There are two conserved cysteine residues which have been shown by site directed mutagenesis studies [45] to affect substrate and small molecule binding, but are not directly ligated to the iron. Substrate binds to the metal center through a thiolate sulfur evidenced by the appearance of a thiolate-to-metal charge transfer transition in the absorption spectrum of the ACV complex of Cu-substituted IPNS, resulting in increased covalency as seen by a reduction in the XAS edge height and its shift to lower energy. Nitric oxide (NO) also binds to the native metal center to form a complex with a characteristic  $S=3/2$  EPR signal. Substrate and NO bind simultaneously to form a ternary complex that is independent of the order of addition. At this point little is known about the catalytic mechanism of this enzyme, although a high-valent iron-oxo intermediate has been proposed [16,46,47].

The hydroxylation of fatty acids and alkanes and the epoxidation of alkenes using molecular oxygen are catalyzed by the mixed function oxidase  $\omega$ -hydroxylase ( $\omega$ H) [48].  $\omega$ H is one of three components, including a flavoprotein reductase and rubredoxin, of the non-heme iron monooxygenase system from *Pseudomonas oleovorans*, and has proven difficult to purify, limiting the available mechanistic and structural information [17,49]. Phospholipids and a stoichiometry of one atom of iron per polypeptide chain are required for full activity [48]. NMR has shown that the epoxidation of terminal olefins to the corresponding 1,2-oxides proceeds with a high degree of stereoselectivity and specificity, resulting primarily in inversion of the original olefin geometry [50]. The stepwise mechanism does not involve complex hydrogen atom abstraction but rather initial attack of “activated” oxygen and final ring closure to the epoxide product [17]. At most, one cysteine sulfur may be ligated to the iron of  $\omega$ H. However, iron contributes only slightly to the visible absorption spectrum, which displays no charge transfer transitions. Thus  $\omega$ H is proposed to have principally nitrogen and/or oxygen coordination [48].

The extra- and intradiol dioxygenases are most often found in soil bacteria for



the degradation of aromatic rings and are also involved in mammalian tyrosine and tryptophan metabolism (the latter leading to the biosynthesis of pyridine nucleotides) [51]. The ferrous site of the extradiol cleaving enzymes is stable in the presence of dioxygen, binds substrate in a bidentate fashion, and has a third coordination position available for small molecule binding and oxygen reaction [52]. The intradiol cleaving enzymes involve a ferric site with two open coordination positions for substrate binding [18] and are the best studied, with high resolution crystal structures available for protocatechuate 3,4-dioxygenase (3,4-PCD) from *Pseudomonas aeruginosa* [53] and *Brevibacterium fuscum* [54]. Fig. 2(b) shows the observed trigonal bipyramidal metal environment with tyrosine 147 and histidine 162 coordinated axially, and tyrosine 118, histidine 160, and hydroxide bound in the equatorial plane. The substrate is thought to bind as a chelate replacing the hydroxide and axial tyrosine [55]. Binding to the  $\text{Fe}^{3+}$  is believed to activate this substrate either by inducing semiquinone- $\text{Fe}^{2+}$  character through high covalency [56], with oxygen then reacting with either the substrate or the iron [57], or by a weakening of the binding of one of the catecholate oxygens with the  $\text{Fe}^{3+}$  to induce ketonization of the substrate followed by oxygen attack on the coordinated hydroxyl group [19]. For either model of substrate activation, the  $\text{ESO}_2$  intermediate observed in the initial phase of this reaction is thought to involve a peroxy adduct of the substrate coordinated to the iron. This converts to  $\text{ESO}_2^*$ , which is a product complex. For the extradiol dioxygenase catechol 2,3-dioxygenase (2,3-CTD), substrate binding activates the ferrous site for small molecule binding [26]. A crystal structure of an extradiol dioxygenase 2,3-dihydroxybiphenyl 1,2-dioxygenase (1,2-DBD) has just been completed [58] and shows that this site is square pyramidal as predicted by MCD spectroscopy on the analogous enzyme 3,4-PCD. The ligation consists of two bound water molecules, a nitrogen from histidine 210, and an oxygen from a carboxylate group which form the equatorial plane, and a nitrogen from histidine 146 coordinated axially.

Phthalate dioxygenase (PDO) catalyzes the *cis*-dihydroxylation of phthalate to 1,2-dihydroxy-4,5-dicarboxy-3,5-cyclohexadiene in the presence of phthalate dioxygenase reductase (PDR), NADH as an electron source, substrate, and oxygen. PDO is substrate specific, activating only phthalate or aromatics with vicinal anionic groups. Although PDO can oxygenate phthalate in the presence of oxygen, PDR is required for efficient catalysis [20]. PDO is a member of a broad class of environmentally significant bacterial dioxygenases which activate aromatic substrates to their *cis*-dihydrodiols for further degradation and catabolism. Other enzymes in this family include benzene dioxygenase [59], benzoate dioxygenase [60], naphthalene dioxygenase [61], pyrazon dioxygenase [62], and toluene dioxygenase [63], all of which contain a [2Fe–2S] Rieske site and a mononuclear non-heme iron center. In addition to the bacterial dioxygenases, there are other enzymes which also contain a Rieske cluster in addition to a mononuclear non-heme iron site but do not yield the dihydrodiol products [64]: 4-chlorophenylacetate 3,4-dioxygenase converts substrate to catechol with chloride elimination [65], vanillate demethylase participates in the biodegradation of lignin [66], and 4-methoxybenzoate *O*-demethylase (putidamoonoxin) catalyzes the conversion of 4-methoxybenzoic acid to 4-hydroxybenzoic acid

and formaldehyde [67]. In all of these systems, the mononuclear non-heme iron is believed to be the active site for catalysis and presumably binds and activates molecular oxygen. PDO is the best-studied enzyme in its class because it is available in high yield and is extremely stable even at room temperature. However, spectroscopic studies that have been performed on PDO, including resonance Raman (rR) [68,69], electron-nuclear double resonance (ENDOR) [70,71], and XAS [72,73], have focused primarily on investigation of the Rieske site owing to its dominant spectroscopic features and have only been used indirectly (i.e., through XAS studies of  $\text{Co}^{2+}$ - and  $\text{Zn}^{2+}$ -substituted protein) to probe the mononuclear non-heme ferrous active site. Low-temperature MCD provides a direct method to probe the native ferrous center of PDO even in the presence of the Rieske site as the latter can be rendered diamagnetic (i.e., no temperature-dependent MCD; vide infra) by oxidation to the antiferromagnetically-coupled  $[\text{Fe}^{\text{III}}\text{--Fe}^{\text{III}}]$  state [74,75] (see Section 4.1).

Phenylalanine (PAH), tyrosine (TH), and tryptophan (TPH) hydroxylases are all tetrahydropterin-dependent enzymes. PAH, which is found in the liver and kidney, is involved in the metabolism of phenylalanine, and its deficiency is responsible for the genetic disorder phenylketonuria (PKU) that is associated with severe mental retardation [76]. It has been thought that the role of the metal ion is to generate a 4a-hydroperoxy intermediate and activate it through forming a  $\mu$ -peroxy pterin-iron complex which could further generate a non-heme oxo-ferryl intermediate and the experimentally observed 4a-hydroxypterin species [77]. In support of this, PAH from *Chromobacterium violaceum* (CVPAH), thought to be a copper enzyme, showed an ESEEM spectrum of a pterin directly coordinated to the metal ion [78] and crystallographic studies on Cu-pterin model complexes indicate that the pterin cofactor binds to the metal center through positions O4 and N5 [79] (Fig. 3(a)). Further, paramagnetic NMR studies on  $\text{Co}^{2+}$ -substituted TH show that phenylalanine, which is also a substrate for this enzyme, binds such that the aromatic ring is in the "second coordination sphere" of the metal ion [80]. Recent studies [81] of CVPAH have questioned whether the copper ion is in fact required for activity and thus whether the iron in mammalian PAHs (which is strictly required for activity) plays a direct oxygen activation role or an indirect structural role in catalysis. As reduction to the  $\text{Fe}^{2+}$  state is required for catalysis, it is critically important to probe the interaction of pterin cofactor with this reduced iron site. However, all studies thus far reported have been on the EPR-active resting ferric site. These studies [82,83] have shown that both active (axial) and inactive (rhombic) iron sites are present which do not interconvert and have a relative ratio dependent on the preparative conditions [84].

Bacterial resistance to penicillin antibiotics is largely due to the hydrolytic activity of the  $\beta$ -lactamase enzymes. Clavaminase synthase (CS) catalyzes the key biosynthetic ring closure step in the formation of clavulanic acid, a potent  $\beta$ -lactamase inhibitor [22]. CS is a member of a large class of non-heme iron enzymes dependent on  $\alpha$ -ketoglutarate ( $\alpha$ -KG) as a cofactor. This class also includes prolyl and lysyl hydroxylases (involved in collagen synthesis) [85], thymine hydroxylase [86], and 4-hydroxyphenylpyruvate dioxygenase [87], all of which catalyze the hydroxylation of substrate. In contrast, CS catalyzes oxidative ring closure similar to the reaction

(a) Cu(tppb)(pterin) model

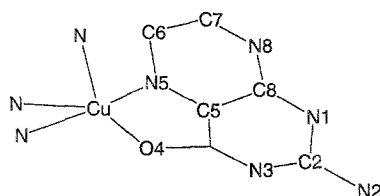
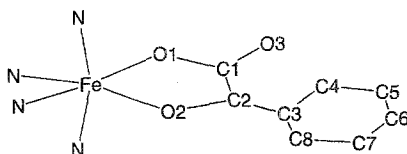
(b) Fe(TLA)( $\alpha$ -KG) model

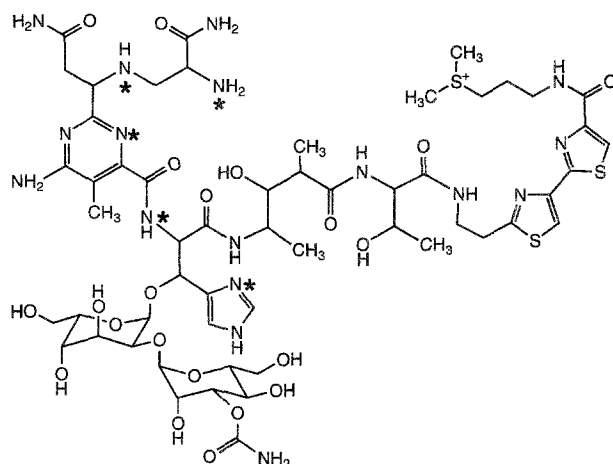
Fig. 3. Metal-cofactor binding interactions proposed from model studies. (a) Cu(tppb)(pterin) coordination scheme for phenylalanine hydroxylase [79]. (b) Fe(TLA)( $\alpha$ -KG) model for clavaminic synthase [90].

catalyzed by IPNS [16], which is not an  $\alpha$ -KG-dependent enzyme. CS is a particularly interesting enzyme in that, depending on substrate, this enzyme can also catalyze hydroxylation [88] as well as ring closure and desaturation chemistry [22,89]. The mechanism of  $\alpha$ -KG-dependent enzymes generally involves the reaction of an  $\alpha$ -KG-bound ferrous active site with dioxygen. Model studies [90] have shown that an  $\alpha$ -KG analog binds to the  $\text{Fe}^{2+}$  site in a bidentate fashion through one carboxylate oxygen (O1) and one carbonyl oxygen (O2) as indicated in Fig. 3(b). The enzymatic reaction generates succinate,  $\text{CO}_2$ , and an activated iron-oxygen species, thought to be an oxo-ferryl unit [91] which goes on to hydroxylate substrate or catalyze oxidative ring closure through the heteroatom.

The lipoxygenases (LOs) catalyze the hydroperoxidation of *cis,cis*-1,4-pentadiene-containing fatty acids. Mammalian LOs catalyze the conversion of arachidonic acid to leukotrienes (5-LOs), which mediate hypersensitivity and inflammation, and lipoxins (15-LOs), which inhibit cellular immunity [23]. 15-LOs are also implicated in the oxidation of low density lipoprotein (LDL) to the atherogenic form which leads to the growth of atherosclerotic lesions [92]. Most mechanistic studies have been performed on the plant enzyme from soybean (SLO-1) which has linoleic acid as a substrate. The resting enzyme is air-stable in its ferrous oxidation state, but is activated by reaction with the hydroperoxide product to produce the ferric site [93]. The fatty acid substrate reacts with this ferric site to produce an intermediate, which then oxygenates to generate the hydroperoxide. The substrate-active site intermediate has been proposed to be either an organometallic complex formed by proton abstrac-

tion and coordination of the carbanion substrate to the ferric center [94] or a ferrous center with a fatty acid radical, which may not be directly coordinated to the iron [95,96]. It has been of significant pharmacological importance to develop inhibitors of the lipoxygenases which are mostly found to be reversible and function by reducing the active ferric center to the ferrous state [97]. Spectroscopic studies have generally indicated that the ferrous site is six-coordinate with at least three histidine ligands [33,98,99]. Recently, two crystal structures have appeared [100,101] on the resting ferrous enzyme that disagree with respect to the active site ligation (Fig. 2(c)). Four amino acid ligands are common to both structures: histidine 499 (N $\epsilon$ ), histidine 504 (N $\epsilon$ ), histidine 690 (N $\epsilon$ ), and isoleucine 839 (OT2). The Boyington et al. [100] crystallographic description of the iron site is four-coordinate with a ligand arrangement described as “distorted octahedral with two adjacent unoccupied coordination positions”. Alternatively, the Minor et al. [101] structure has an additional residue as a ligand, asparagine 694 (O $\delta$ 1), and the further possibility of a sixth water based ligand as has been proposed from EPR line-broadening studies on the ferric enzyme [102]. MCD spectroscopy has been used to elucidate the relationship of the two crystal structures to the protein active site in solution and has provided a means of spectroscopic investigation of multiple components of a mixture [103] (see Section 4.2).

Bleomycin (BLM), a histidine-containing glycopeptide antibiotic produced by strains of *Streptomyces verticillus*, is used in treatment against a variety of carcinomas and lymphomas [104]. The anticancer activity of the drug Blenoxane<sup>®</sup> involves selective DNA cleavage at certain GT and GC sites in the presence of metal ions and dioxygen [24,25,105]. The structure of BLM is shown in Fig. 4(a) and includes three domains [24]: the bithiazole tail which is involved in BLM binding to DNA, the sugar moiety which is believed to be responsible for uptake by cancer cells, and the  $\beta$ -aminoalanine-pyrimidine-histidine region which binds metal ions. BLM is generally thought to be most reactive as a ferrous complex with histidine, deprotonated amide, pyrimidine, and secondary amine nitrogens as equatorial ligands [24,25]. No crystal structure exists of the ferrous complex and present descriptions are based on correlations to a Cu(II) complex of the related biosynthetic precursor P-3A, which has a square pyramidal geometry [106]. However, Cu<sup>2+</sup> has strong structural preferences due to the Jahn-Teller effect which Fe<sup>2+</sup> does not, and P-3A lacks the disaccharide and bithiazole moieties of BLM, the former being a potential ligand. Thus, there is some controversy with respect to axial ligation where both the carbamoyl group of the mannose sugar [107] and the primary amine from the  $\beta$ -aminoalanine [108] have been implicated, with the sixth position being the site of exogenous ligand binding. BLM binds to DNA via intercalation and/or ionic interactions with the minor groove, with both the bithiazole and the metal chelating regions playing a significant role in the binding and specificity [109–111]. Kinetic and spectral studies [112,113] have demonstrated that the mechanism of activation involves a high-spin Fe(II)BLM species reacting with dioxygen to form oxygenated BLM, described as a ferric-superoxide complex. This in turn acquires an additional electron from either a second Fe(II)BLM molecule or another reductant to generate activated BLM, which is best described as a ferric-peroxide complex [114–116].

(a) Bleomycin A<sub>2</sub>

## (b) PMAH

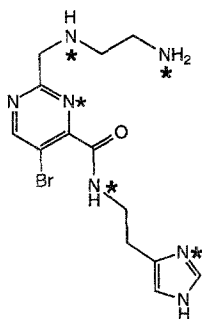


Fig. 4. Structural ligand frameworks. (a) Bleomycin A<sub>2</sub>. (b) The analogous model complex PMAH. Coordinating nitrogens are denoted with asterisks (\*) for each structure.

despite showing reactivity [112,117] similar to the generally assumed oxo-ferryl heme intermediate of cytochrome P-450 [7,118]. Activated BLM reacts with DNA by hydrogen atom abstraction from the C-4' position of the deoxyribose sugar, leading to DNA degradation concomitant with base propenal formation [24]. The anticancer activity of BLM has prompted the synthesis of numerous models to mimic portions of the metal binding region and the reactivity of BLM [119,120]. In particular, PMAH (Fig. 4(b)) contains the imidazole, amide, pyrimidine, secondary and primary amine functionalities and its ferrous complex reacts with dioxygen to generate an intermediate with very similar spectral features and reactivity to activated BLM [119]. MCD has been used to determine the Fe<sup>2+</sup> chelating mode of BLM by comparison to the ferrous complex of PMAH [121]. Further, Fe(II)BLM and

$[\text{Fe(II)PMA}]^+$  differ from the other non-heme iron enzymes listed above in that they exhibit moderately intense, low-energy charge transfer transitions. This difference also manifests itself in unusual ground-state MCD parameters for  $\text{Fe(II)BLM}$  and  $[\text{Fe(II)PMA}]^+$  leading to the prediction of strong  $\pi$ -bonding interactions with the pyrimidine ligand which can significantly affect the reactivity of mononuclear non-heme ferrous active sites (see Section 4.3).

## 2.2. Physical methods

The  $\text{Fe}^{2+}$  free ion has a  $d^6$  configuration with four unpaired electrons to give a  $^5D$  ground-state atomic term symbol. If the ion is subjected to an octahedral crystal field, the  $d$ -orbitals separate into a triply degenerate  $t_{2g}$  set and a doubly degenerate  $e_g$  set, splitting the  $^5D$  state into a high-spin paramagnetic  $^5T_{2g}$  ground state separated by the energy  $10Dq(O_h)$  from a  $^5E_g$  excited state, where  $Dq$  is the cubic field splitting parameter. When the crystal field is strong enough to overcome the spin pairing energy, the  $t_{2g}$  orbitals are completely filled, resulting in a low-spin diamagnetic  $^1A_{1g}$  ground state. This scheme is summarized in Fig. 5, which shows the  $d^6$  Tanabe–Sugano diagram for  $\text{Fe}^{2+}$  [122]. Since the appropriate range of  $Dq$  values for ligands found in non-heme ferrous active sites (primarily oxygen and nitrogen ligands) is  $\sim 500$ – $1200\text{ cm}^{-1}$  and the free ion  $B$  value is  $917\text{ cm}^{-1}$ , the region of the Tanabe–Sugano diagram applicable to these systems is the weak-field, high-spin side, highlighted on the left in Fig. 5. There is only one spin-allowed one-electron transition

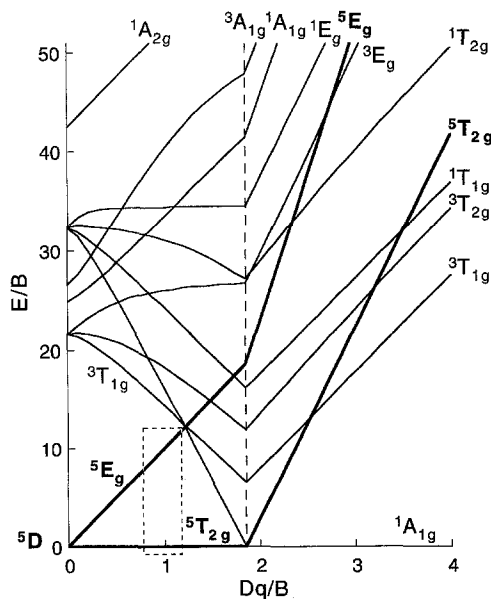


Fig. 5.  $d^6$  Tanabe–Sugano diagram. Energy levels were calculated with  $C/B=4.4$  and for a  $Dq$  range of  $0$ – $4000\text{ cm}^{-1}$ . The boxed area indicates the region relevant to high-spin non-heme ferrous sites.

from the  ${}^5T_{2g}$  ground state, namely the  ${}^5T_{2g} \rightarrow {}^5E_g$  transition. The  ${}^5T_{2g} \rightarrow {}^5E_g$  transition is electric dipole forbidden by parity; however, this can be overcome by magnetic dipole and vibronic coupling mechanisms. In a non-heme ferrous active site, the local symmetry around the metal ion will be low, removing the parity restriction and splitting the  ${}^5E_g$  excited state into two orbitally non-degenerate states that can be probed by absorption, CD, and MCD spectroscopies (vide infra). Since the  ${}^5T_{2g} \rightarrow {}^5E_g$  transition corresponds to the  $(t_{2g})^4(e_g)^2 \rightarrow (t_{2g})^3(e_g)^3$  one-electron promotion, this splitting of the  $d_{z^2}$  and  $d_{x^2-y^2}$  set of  $e_g$  orbitals reflects the splitting of the  ${}^5E_g$  excited state and its energy dependence on active site geometry. The experimentally measured transitions give the  ${}^5E_g$  splittings, which can then be related to the geometric and electronic structure of the complex through ligand field theory (see Section 3.2).

The degeneracy of the  ${}^5T_{2g}$  ground state is also removed in a low symmetry environment to produce three orbitally non-degenerate quintet states. However, it is difficult to directly observe the splittings between these states because the far- to mid-infrared energy regions ( $100\text{--}2000\text{ cm}^{-1}$ ) are congested with intense vibrational transitions. The lowest-energy spin sublevels ( $< \sim 30\text{ cm}^{-1}$ ) of the orbitally non-degenerate quintet ground state can be probed by EPR, Mössbauer, VTVH magnetic susceptibility, and VTVH MCD (vide infra) spectroscopies and can be modeled by the spin Hamiltonian [123] given in Eq. (1):

$$\mathcal{H} = \vec{S} \cdot \vec{D} \cdot \vec{S} + \beta \vec{H} \cdot \vec{g} \cdot \vec{S} \quad (1)$$

where  $\vec{D}$  is the zero-field splitting (ZFS) tensor,  $\vec{S}$  is the spin operator,  $\beta$  is the Bohr magneton,  $\vec{H}$  is the applied magnetic field, and  $\vec{g}$  is the  $g$ -tensor. Assuming that the  $\vec{D}$  and  $\vec{g}$  tensors are coaxial and that the total spin is two ( $S=2$ ), the general expression in Eq. (1) can be rewritten as Eq. (2).

$$\mathcal{H} = D(\hat{S}_z^2 - 2) + E(\hat{S}_x^2 - \hat{S}_y^2) + \beta(g_x H_x \hat{S}_x + g_y H_y \hat{S}_y + g_z H_z \hat{S}_z) \quad (2)$$

$D$  and  $E$  are the axial and rhombic ZFS parameters, respectively, and  $g_x$ ,  $g_y$ , and  $g_z$  are the molecular  $g$ -values.

When applied to a distorted octahedral system, a positive value of  $D$  corresponds to a contraction along the molecular  $z$ -axis; conversely, a negative value of  $D$  corresponds to an elongated octahedron (see Section 3.2). As shown in Fig. 6, the non-degenerate  $M_s=0$  level lies lowest in energy for  $D>0$  while the doubly degener-

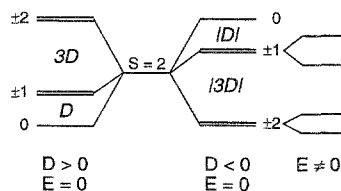


Fig. 6. Energy splittings of the  $S=2$  sublevels for axial and rhombic ZFS. For  $D>0$  (left), the  $M_s=0$  level is lowest and the  $M_s=\pm 1$  and  $\pm 2$  levels lie at  $D$  and  $3D\text{ cm}^{-1}$ , respectively. For  $D<0$  (right), the doubly degenerate  $M_s=\pm 2$  level is lowest. Rhombic ZFS ( $E$ ) removes the degeneracy of both the  $M_s=\pm 1$  and  $\pm 2$  levels (far right).

ate  $M_S = \pm 2$  level is lowest for  $D < 0$ . The  $M_S = \pm 2$  doublet has an effective  $g$ -value of 8.00 (assuming the molecular  $g$ -values are 2.00). The three levels obtained for an axially distorted system,  $M_S = 0, \pm 1$ , and  $\pm 2$ , are split in energy by the amounts  $|D|$  and  $|3D|$  respectively, as shown in Fig. 6. The theoretical ranges of  $D$  have been found to be  $\sim 2$  to  $15 \text{ cm}^{-1}$  for  $+D$  systems and approximately  $-3$  to  $-23 \text{ cm}^{-1}$  for  $-D$  systems (Section 3.4). The rhombic ZFS parameter  $E$  ranges in value from zero to  $D/3$ , and if  $E$  is non-zero, all five spin sublevels in the  $S=2$  non-Kramers system will be non-degenerate (Fig. 6, right).

Once an  $\text{Fe}^{2+}$  system is known to be a high-spin monomer, the geometric and electronic structures can be elucidated from a combination of the experimentally determined spin Hamiltonian parameters  $D$  and  $E$  and the  $d \rightarrow d$  transition energies (Section 3.4). This information has generally been obtained by the ground-state techniques of magnetic susceptibility [124], magnetic Mössbauer [125], and EPR [123] spectroscopies and the excited-state technique of optical absorption. Some less common techniques have also been used to probe the ground state of ferrous complexes including electronic Raman [126–128] and far-infrared absorption [129–131], but neither of these methods has been applied to a non-heme ferrous enzyme.

Magnetic susceptibility is the measurement of the magnetic moment of a sample at a given field and temperature. The data can be collected in two different ways: over a broad temperature range at constant field, or as a function of both temperature and field, which is termed saturation magnetization [132,133]. The limitation of magnetic susceptibility is that it is a bulk measurement. Protein susceptibility experiments require sample concentrations of the order of  $10^{-3} \text{ M}$ , only a single paramagnetic species, and an accurate way to subtract the large diamagnetic background from the sample holder, buffer, and protein moiety [134]. Although magnetic susceptibility data have been published on binuclear non-heme ferrous enzymes [135,136], the only study of a mononuclear system has been on SLO-1 [137,138], and this was complicated by the fact that it was performed on a mixture of species [103].

Magnetic Mössbauer spectroscopy measures the transitions between the magnetic field split hyperfine levels of the  $^{57}\text{Fe}$  nucleus [125,139]. The splitting pattern is a function of the  $\tilde{D}$  and  $\tilde{g}$  tensors and the hyperfine tensor, and is iteratively fit to extract the spin Hamiltonian parameters. A clear splitting pattern due to one species is necessary to obtain a reliable fit, and this is a function of the  $^{57}\text{Fe}$  concentration, number of unique metal sites, temperature, and recoil properties of the material. The sample requirements for an enzyme study are that the protein be  $^{57}\text{Fe}$  enriched, pure, and cooled to liquid He temperatures [125,139]. Only two non-heme ferrous active sites have been probed via magnetic Mössbauer, SLO-1 and 3,4-PCD [98,140]. The SLO-1 data are noisy and were not used to extract spin Hamiltonian parameters [140], and as mentioned above, the Mössbauer spectra on native reduced SLO-1 may be complicated by the existence of a mixture of two forms of the enzyme [103]. Conversely, the 3,4-PCD study is an excellent example of the utility of this technique when the sample is amenable to study. The splitting pattern was fit to obtain values of  $D = -6 \pm 1 \text{ cm}^{-1}$  and  $|E/D| = 0.25 \pm 0.05$  [140].

EPR spectroscopy measures the field at which a fixed microwave frequency induces



a transition from one  $M_S$  sublevel to another, usually with a selection rule of  $\Delta M_S = \pm 1$  [123]. EPR signals of integer spin systems are often not observed because these systems have zero-field splittings larger than the frequency probe energy of  $0.33 \text{ cm}^{-1}$  for X-band spectrometers [141–143]. For some ferrous complexes with significant inhomogeneous line broadening, a broad transition will be observed in the region of  $g=9$ , although these systems are less common and most  $S=2$  systems are EPR silent [144]. For  $D < 0$  systems, this is formally a  $\Delta M_S = 4$  transition ( $-2 \rightarrow +2$ ) and is made allowed by the limited mixing of the  $|-2\rangle$  and  $|+2\rangle$  components by the rhombic term in Eq. (2). Thus there is a small  $\Delta M_S = 0$  component to this transition which is allowed in non-normal longitudinal mode EPR spectroscopy. Inhomogeneous broadening of the  $M_S = -2$  and  $M_S = +2$  levels produces a spread in the ZFS [145,146] and some fraction of the ensemble can have a  $ZFS < 0.33 \text{ cm}^{-1}$ . The temperature dependence of this integer spin EPR signal can then be used to establish spin Hamiltonian parameters [135]. No studies of a mononuclear non-heme ferrous enzyme have been reported.

As mentioned above, the energies of excited states are extremely sensitive to coordination number and geometry and have been probed by absorption spectroscopy in model complexes. The ligand field  $d \rightarrow d$  transitions of mononuclear ferrous complexes occur in the near-infrared (NIR) region while the charge transfer transitions occur in the ultraviolet region for non-heme non-iron-sulfur centers [147]. Therefore,  $\text{Fe}^{2+}$  systems are often colorless and have been regarded as spectroscopically inaccessible [148]. However, the energies of the  $d \rightarrow d$  transitions directly reflect both the geometric and electronic structures of the ferrous center and are energetically isolated from the vibrational and charge transfer regions. In principle, measuring the NIR absorption spectrum is a simple experiment which can provide significant insight. In practice, the extinction coefficients are small ( $1\text{--}50 \text{ M}^{-1} \text{ cm}^{-1}$ ) and overtones from solvent and ligand C–H and O–H vibrations can obscure the ligand field bands. In fact, the only published mononuclear ferrous enzyme NIR absorption spectrum is for  $\text{Fe(II)SOD}$  [33] (see Fig. 7(a)).

For reference to the protein systems under investigation here, it is important to catalog the available ground- and excited-state data for structurally defined mononuclear ferrous model complexes (excluding heme and iron-sulfur systems). A sampling of ground-state parameters and excited-state transition energies for different structural types is presented in Tables 1 and 2.

### 3. Methodology

As described above, ligand field transitions of non-heme ferrous centers are often difficult to observe in absorption spectroscopy, but can be probed by circular dichroism (CD) and magnetic circular dichroism (MCD) spectroscopies because of their different selection rules. The CD and MCD spectra in the NIR region allow observation and resolution of the  $d \rightarrow d$  excited-state transitions [12,26,33,75,103,121] which are not usually accessible in absorption (*vide supra*). This excited-state information is then used to elucidate the coordination number and geometry of the  $\text{Fe}^{2+}$

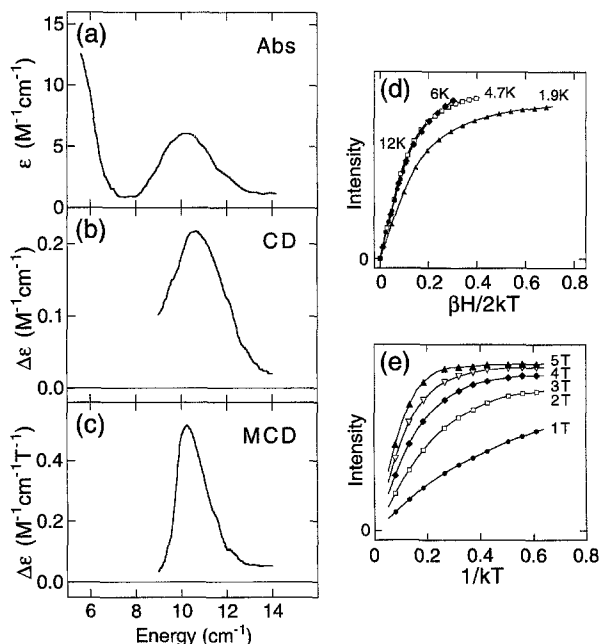


Fig. 7. Ligand field spectra and saturation magnetization data for FeSOD. (a) Absorption spectrum. (b) Room temperature CD spectrum. (c) Low-temperature MCD spectrum. (d) VTVH MCD intensity is plotted versus  $\beta H/2kT$ , in which each line represents a fixed temperature over a range of magnetic fields. (e) The same data are replotted as a function of  $1/kT$  to decouple magnetic field and temperature effects; each line represents a fixed magnetic field over a range of temperatures.

center at the protein active site. Analysis of the temperature and field dependence of the MCD intensities of these transitions provides information about the ground state for these paramagnetic ferrous centers. Ligand field analysis is combined with the excited- and ground-state data to provide detailed insight into the geometric and electronic structures of an  $\text{Fe}^{2+}$  site. An example of this combination of optical absorption, CD, MCD, and variable-temperature variable-field (VTVH) MCD spectroscopies is given in Fig. 7, which shows all of these data for the enzyme FeSOD [33]. In this section, we will develop the methodology to treat this type of data.

### 3.1. MCD theory

Both MCD and CD spectroscopies measure the difference  $\Delta\epsilon$  between the left and right circularly polarized (lcp and rcp) extinction coefficients,  $\epsilon_L$  and  $\epsilon_R$  (Eq. (3)).

$$\Delta\epsilon = \epsilon_L - \epsilon_R = \Delta A/bC \quad (3)$$

$\Delta\epsilon$  relates to the difference between lcp and rcp absorbance,  $\Delta A$ , via Beer's Law, where  $b$  is the path length in cm and  $C$  is the concentration in moles/liter to give units of  $\text{M}^{-1} \text{cm}^{-1}$ . For a material to exhibit CD transitions, it must possess chirality, i.e., the chromophore cannot be superimposable on its mirror image. Optical activity

Table 1

Ground-state parameters for mononuclear non-heme ferrous model complexes

C.N.	Complex	Fe <sup>2+</sup> ligands	Method <sup>a</sup>	D (cm <sup>-1</sup> )	E (cm <sup>-1</sup> )	<i>g</i> <sub>  </sub> / <i>g</i> <sub>⊥</sub> <sup>b</sup>	Ref.
6	Fe(H <sub>2</sub> O) <sub>6</sub> SiF <sub>6</sub>	6O	FIR	11.8	0.67		[129]
			EPR	11.9	0.67	1.96	[149]
			susc.	10.9		2.00/2.12	[150,151]
	Fe(H <sub>2</sub> O) <sub>6</sub> (NH <sub>4</sub> ) <sub>2</sub> (SO <sub>4</sub> ) <sub>2</sub>	6O	Möss.	−21 or +15	D/3		[152]
	Fe(py) <sub>4</sub> (CF <sub>3</sub> SO <sub>3</sub> ) <sub>2</sub>	4N, 2O	susc.	[6.1]		2.15	[153]
	Fe(py) <sub>4</sub> (CH <sub>3</sub> SO <sub>3</sub> ) <sub>2</sub>	4N, 2O	susc.	[3.4]		2.05	[153]
	Fe(py) <sub>4</sub> ( <i>p</i> -CH <sub>3</sub> C <sub>6</sub> H <sub>4</sub> SO <sub>3</sub> ) <sub>2</sub>	4N, 2O	susc.	[3.9]		2.09	[153]
5	Fe(bpy)Cl <sub>2</sub>	4N, 2Cl	susc.	~ −2			[154]
	Fe:ZnF <sub>2</sub>	6F	susc.	−4.9		2.25/2.04	[155]
	[Fe(TMC)(NCCH <sub>3</sub> )] <sup>2+</sup>	4N, 1N'	susc.	3.4	−°	2.63/2.00	[156]
	[Fe(TMC)(N <sub>3</sub> )] <sup>+</sup>	4N, 1N'	susc.	2.1	−°	2.39/2.01	[156]
	[Fe(TMC)(NCS)] <sup>+</sup>	4N, 1N'	susc.	5.4	−°	2.58/1.96	[156]
	[Fe(TMC)Br] <sup>+</sup>	4N, 1Br	susc.	5.7	−°	2.32/1.95	[156]
	[Fe(TMC)Cl] <sup>+</sup>	4N, 1Cl	susc.	6.2	−°	2.03/2.00	[156]
	[Fe(1,7-CT)Cl] <sup>+</sup>	4N, 1Cl	susc.	8.8	−°	2.28/1.94	[156]
	[Fe(1,3,7,10-CT)Cl] <sup>+</sup>	4N, 1Cl	susc.	3.1	−°	2.22/2.01	[156]
4	BaFeSi <sub>4</sub> O (gillespite)	4O	susc.	11.6			[157]
	Fe(biq)(NCS) <sub>2</sub>	2N, 2N'	susc. + Möss.	~ 5.0		2.41/2.24	[158]
	Fe(2,9-dmp)(NCS) <sub>2</sub>	2N, 2N'	susc. + Möss.	−2 to −5			[158]
	Fe(2,9-dmp)Cl <sub>2</sub>	2N, 2Cl	Möss.	>0			[158]
	[FeCl <sub>4</sub> ](NMe <sub>4</sub> ) <sub>2</sub>	4Cl	Möss.	9.0		2.05/2.27	[159]

<sup>a</sup> FIR, far-infrared magnetic resonance; EPR, electron paramagnetic resonance; susc., magnetic susceptibility; Möss., magnetic Mössbauer. <sup>b</sup> Refers to *g*(average) if only one number is reported. ° −, *E* is assumed to be negligible.

can also be induced by an applied magnetic field, so that all substances exhibit MCD activity.

There are many advantages to CD and MCD over absorption spectroscopy for probing the d→d transitions in high-spin ferrous active sites. First, since Δ*ε* is signed, overlapping bands observed in absorption are often resolved by CD and MCD spectroscopies. Second, because CD spectroscopy is a differential technique that utilizes phase sensitive detection, CD signals from systems with extinction coefficients of ~1–10 M<sup>-1</sup>cm<sup>-1</sup> and Δ*ε* values of ~10<sup>-6</sup> M<sup>-1</sup>cm<sup>-1</sup> are routinely measured [171]. While CD spectra typically have moderate intensities, MCD spectra of materials with degenerate or near degenerate ground states show high intensities at low temperature (<4.2 K), so that systems with weak or no CD intensities can still be probed via MCD spectroscopy [172]. The increased MCD intensity of paramagnetic centers means that the signal due to the metal center in a dilute protein solution will be greatly amplified (by two to three orders of magnitude) over those of the

Table 2

Excited-state absorption data for mononuclear non-heme ferrous model complexes

C.N.	Parent geometry	Complex	Fe <sup>2+</sup> ligands	Excited-state transitions (cm <sup>-1</sup> )		Ref.
6	<i>octahedral</i>	Fe(H <sub>2</sub> O) <sub>6</sub> <sup>2+</sup> (in water)	6O	8300	10 400	[160]
		Fe(H <sub>2</sub> O) <sub>6</sub> (NH <sub>4</sub> ) <sub>2</sub> (SO <sub>4</sub> ) <sub>2</sub>	6O	8400	10 800	[160]
		Fe(H <sub>2</sub> O) <sub>6</sub> SiF <sub>6</sub>	6O	8700	10 300	[160]
		Fe(Im) <sub>6</sub> Cl <sub>2</sub>	6N	9800	11 750	[161]
		Fe(py) <sub>4</sub> (NCS) <sub>2</sub>	4N, 2N'	9880	11 460	[162]
		Fe(py) <sub>4</sub> Cl <sub>2</sub>	4N, 2Cl	8720	10 520	[162]
5	<i>square pyramidal trigonal bipyramidal</i>	[Fe([14] dieneN <sub>4</sub> )Cl] <sup>+</sup>	4N, 1Cl	4700	12 200	[163]
		[Fe([14] dieneN <sub>4</sub> )Br] <sup>+</sup>	4N, 1Br	~ 5000	12 200	[163]
		[Fe(Me <sub>6</sub> tren)Br] <sup>+</sup>	4N, 1Br	< 4000	9800	[164]
		Fe(MeTPyA)Br <sup>+</sup>	4N, 1Br	5400	8700	[165]
		Fe(MeTPyA)Cl <sup>+</sup>	4N, 1Cl	5400	9000	[165]
		Fe(Me <sub>5</sub> dien)Cl <sub>2</sub>	3N, 2Cl	~ 4000	8400	[166]
4	<i>tetrahedral</i>	[Fe(NCS) <sub>4</sub> ] <sup>2-</sup>	4N	4650	5780	[167]
		Fe(2,9-dmp)(NCS) <sub>2</sub>	2N, 2N'	5600	6940	[158]
		Fe(2,9-dmp)Cl <sub>2</sub>	2N, 2Cl	6800		[158]
		Fe(L <sup>+</sup> )Cl <sub>3</sub>	1N, 3Cl	4000	4910	[168]
		[FeCl <sub>4</sub> ](NMe <sub>4</sub> ) <sub>2</sub>	4Cl	~ 4060		[169]
	<i>square planar</i>	BaFeSi <sub>4</sub> O <sub>10</sub> (gillespite)	4O	8300	~ 20 000	[170]

vibrational overtones of water and the protein backbone. Finally, the magnetic field and temperature dependence of the MCD signals can be used to obtain detailed information about the energy splittings of the ground-state sublevels (see Section 3.3), which can be related to ligand field theory to provide structural information (see Section 3.4). In order to apply these effects to non-heme ferrous active sites, it is necessary to understand how the observed CD and MCD spectra relate to electronic structure. The theoretical basis for these relationships has been developed in detail by Stephens [171,173–175].

### 3.1.1. Circular dichroism spectroscopy

The selection rule for CD activity is that the optical transition from a ground state  $|A\rangle$  to an excited state  $|J\rangle$  must be simultaneously electric dipole and magnetic dipole allowed along the same molecular direction [172] (Eq. (4)).

$$R = \text{Im}(\langle A | \vec{m} | J \rangle \cdot \langle J | \vec{\mu} | A \rangle) \quad (4)$$

In Eq. (4),  $R$  is the rotational strength of the CD transition,  $\vec{m}$  is the electric dipole operator  $e\vec{r}$ , and  $\vec{\mu}$  is the magnetic dipole operator  $\beta(\vec{L} + 2\vec{S})$ .  $R$  is related to experimental data by Eq. (5) [176], where  $h$  is Planck's constant,  $c$  is the speed of light,  $N_0$  is Avogadro's number, and  $\nu$  is the experimental frequency.

$$R = \frac{3hc10^3 \ln 10}{32\pi^3 N_0} \int \frac{\Delta\varepsilon(\nu)}{\nu} d\nu \quad (5)$$

From Eq. (4),  $R$  is non-zero (i.e., the electric and magnetic dipoles have non-zero projections) only for systems described by the point groups  $C_n$ ,  $D_n$ ,  $O$ ,  $T$ , and  $I$  [176]. Thus, low symmetry protein active sites ( $C_1$  symmetry) will have CD activity. Furthermore, because the CD selection rule is different from that for absorption, the CD spectrum may reveal different transitions, particularly those having significant magnetic dipole character.

### 3.1.2. Magnetic circular dichroism spectroscopy

MCD intensity for a transition from a ground state  $|A\rangle$  to an excited state  $|J\rangle$  is historically written as in Eq. (6) for broad band transitions [171,172,174,175].

$$\frac{\Delta A}{E} = \left( \frac{2N_0\pi^3\alpha^2 Cl \lg e}{250hcn} \right) \beta H \left[ \mathcal{A}_1 \left( \frac{-\partial f(E)}{\partial E} \right) + \left( \mathcal{B}_0 + \frac{\mathcal{C}_0}{kT} \right) f(E) \right] \quad (6)$$

In this expression,  $\Delta A$  is the field-dependent difference between lcp and rcp absorption,  $E = h\nu$ ,  $\alpha$  is the electric permeability,  $C$  is the concentration,  $l$  is the path length,  $n$  is the index of refraction,  $\beta$  is the Bohr magneton, and  $H$  is the applied magnetic field.  $\mathcal{A}_1$ ,  $\mathcal{B}_0$ , and  $\mathcal{C}_0$  are the first-order MCD  $\mathcal{A}$ -,  $\mathcal{B}$ -, and  $\mathcal{C}$ -terms, respectively, and will be discussed below following the notation of Piepho and Schatz [172],  $f(E)$  is the band shape in absorption, and  $\partial f(E)/\partial E$  is its first derivative. Eq. (6) is only applicable when the MCD intensity is linear with field (non-linear magnetic field MCD behavior is considered in Section 3.3).  $\mathcal{A}_1$  is the magnitude of any feature with the derivative bandshape,  $\mathcal{B}_0$  is the magnitude of any feature with the absorption bandshape and temperature-independent intensity, and  $\mathcal{C}_0$  is the magnitude of any feature with the absorption bandshape that increases in intensity with decreasing temperature. An experimentally observed transition may have contributions from all three terms, which can be fit to determine their relative magnitudes.

$\mathcal{A}$ - and  $\mathcal{C}$ -terms occur in systems which have either degenerate excited states or degenerate ground states that are split in a magnetic field due to the Zeeman effect, as illustrated in Figs. 8 and 9.  $\mathcal{A}_1$  and  $\mathcal{C}_0$  are related to molecular electronic structure by Eqs. (7) and (8),

$$\begin{aligned} \mathcal{A}_1 = \frac{1}{|d_A|} \sum & (\langle J|L_z + 2S_z|J\rangle - \langle A|L_z + 2S_z|A\rangle) \\ & \times (|\langle A|m_-|J\rangle|^2 - |\langle A|m_+|J\rangle|^2) \end{aligned} \quad (7)$$

$$\mathcal{C}_0 = \frac{-1}{|d_A|} \sum \langle A|L_z + 2S_z|A\rangle (|\langle A|m_-|J\rangle|^2 - |\langle A|m_+|J\rangle|^2) \quad (8)$$

where  $|d_A|$  is the electronic degeneracy of the ground state  $|A\rangle$  and the summation is over all components of  $|A\rangle$  and  $|J\rangle$ . The first part of the  $\mathcal{A}$ -term expression, Eq. (7), is the difference between the excited- and ground-state Zeeman terms while the first part of the  $\mathcal{C}$ -term expression, Eq. (8), is only a ground-state Zeeman term.

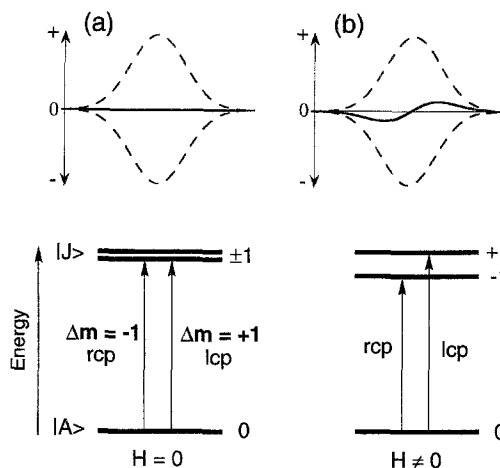


Fig. 8. MCD  $\mathcal{A}$ -term mechanism. (a) In the absence of a magnetic field, the rcp and lcp transitions from a non-degenerate ground state to a doubly degenerate excited state cancel, resulting in no observed MCD intensity. (b) Applying a magnetic field removes the degeneracy of the excited state so that the rcp and lcp transitions combine to give an MCD transition which has a derivative bandshape, called an  $\mathcal{A}$ -term.

The second parts of Eqs. (7) and (8) give the difference between the lcp ( $m_+$ ) and rcp ( $m_-$ ) electric dipole moments, where  $m_{\pm}$  are defined in Eq. (9).

$$m_{\pm} \equiv \mp \frac{1}{\sqrt{2}} (m_x \pm m_y) \quad (9)$$

This electric dipole operator transforms as  $(x,y)$  which is described by the E irreducible representation in axial point groups (i.e.,  $C_n$  and  $D_n$  for  $n > 2$ ). Thus, in systems with a first-order Zeeman interaction for the magnetic field along the molecular  $z$ -axis,  $xy$ -polarized electric dipole transitions will dominate the  $\mathcal{A}$ - and  $\mathcal{C}$ -term components of the MCD spectrum. Furthermore, from the electric dipole term in Eq. (7), the MCD selection rule is  $\Delta M_L = \pm 1$ , requiring that either the ground state or excited state contains orbital angular momentum. Thus,  $\mathcal{A}$ - and  $\mathcal{C}$ -term MCD transitions observed between spin degenerate orbital singlets occur by spin-orbit mixing with other states.

For  $\mathcal{A}$ -terms, if the excited state  $|J\rangle$  has degeneracy, the Zeeman term ( $\langle J|L_z + 2S_z|J\rangle$ ) will split  $|J\rangle$  into oppositely signed  $M_J$  components which will have oppositely signed MCD bands because of the  $\Delta m_{\pm}$  term. Since the Zeeman splittings are of the order of a few wavenumbers and the  $d \rightarrow d$  band widths are of the order of  $1000 \text{ cm}^{-1}$ , the oppositely signed dipole transitions will sum to a derivative shape with a very small  $\Delta A$ , as shown in Fig. 8(b). This effect also occurs for a degenerate ground state (Fig. 9(b)) as long as  $kT$  is large relative to the Zeeman splittings so

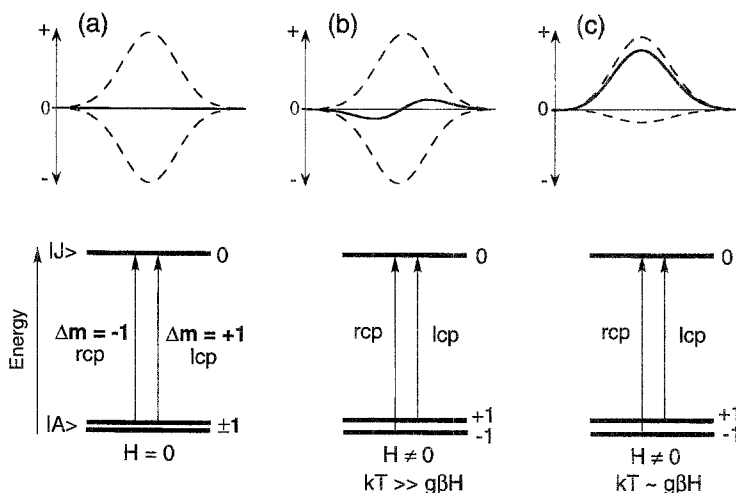


Fig. 9. MCD  $\mathcal{E}$ -term mechanism. (a) With no applied field, the rcp and lcp transitions from a doubly degenerate ground state to an excited state cancel, resulting in no observed MCD intensity. (b) In the presence of a magnetic field and for  $kT \gg g\beta H$ , the degeneracy of the ground state is removed so that the rcp and lcp transitions combine to give an MCD transition which has a derivative bandshape ( $\mathcal{A}$ -term). (c) At low temperatures, when  $kT \sim g\beta H$ , the two levels of ground-state doublet are unequally populated, resulting in an MCD transition with an absorption bandshape, called a  $\mathcal{E}$ -term.

that the Boltzmann populations over the sublevels are comparable. Because their intensities are always small for broad band transitions and orbital degeneracy is not present in low symmetry protein sites,  $\mathcal{A}$ -terms can generally be excluded as a source of MCD intensity for high-spin ferrous centers.

The origin of the  $\mathcal{E}$ -term is related to the  $\mathcal{A}$ -term, except that  $\mathcal{E}$ -terms require a degenerate ground state and that  $kT$  be of the order of the Zeeman splitting. At high temperatures, the observed MCD transitions originating from a degenerate ground state will have pure  $\mathcal{A}$ -term intensity (derivative bandshape), as depicted in Fig. 9(b). When the temperature is reduced, the Boltzmann population of the lowest ground-state sublevel will be larger than the higher-energy sublevels and the MCD transition is a combination of  $\mathcal{A}$ - and  $\mathcal{E}$ -terms (Fig. 9(c)). When the temperature is low enough that the higher-energy sublevels are completely depopulated, the intensity of the MCD band originating from a degenerate ground state will be maximized and will exhibit essentially pure  $\mathcal{E}$ -term behavior. Under these conditions the MCD intensity will no longer increase with increasing magnetic field or decreasing temperature and is said to be saturated; this non-linear behavior is treated in detail in Section 3.3.

The  $\mathcal{B}$ -term contribution to an MCD band has the absorption bandshape like the  $\mathcal{E}$ -term; however,  $\mathcal{B}$ -terms arise from field-induced mixing with an intermediate state  $|K\rangle$ . Eq. (10) gives the basic relation between the  $\mathcal{B}$ -term and molecular properties.

$$\mathcal{B}_0 = \frac{2}{|d_A|} \text{Re} \sum \left[ \sum_{K(K \neq J)} \frac{\langle J|L_z + 2S_z|K\rangle}{\Delta E_{KJ}} [(\langle A|m_-|J\rangle \langle K|m_+|A\rangle - \langle A|m_+|J\rangle \langle K|m_-|A\rangle) + \sum_{K(K \neq A)} \frac{\langle K|L_z + 2S_z|A\rangle}{\Delta E_{KA}} (\langle A|m_-|J\rangle \langle J|m_+|K\rangle - \langle A|m_+|J\rangle \langle J|m_-|K\rangle)] \right] \quad (10)$$

Eq. (10) is similar to the  $\mathcal{A}$ - and  $\mathcal{C}$ -term expressions in that it contains the product of Zeeman and electric dipole terms. The first part of Eq. (10) is the Zeeman interaction between the excited state  $|J\rangle$  and the intermediate state  $|K\rangle$ , divided by their energy separation ( $\Delta E_{KJ}$ ); this is followed by a product of the electric dipole matrix elements from the ground state  $|A\rangle$  to both the excited state  $|J\rangle$  and the intermediate state  $|K\rangle$ . The second part of Eq. (10) is the Zeeman interaction between the ground and intermediate states,  $|A\rangle$  and  $|K\rangle$ , divided by their energy separation ( $\Delta E_{KA}$ ), followed by the product of the electric dipole moments from  $|A\rangle$  and  $|K\rangle$  to the excited state  $|J\rangle$ . If  $|K\rangle$  is substantially higher in energy than  $|J\rangle$ , the resultant  $\mathcal{B}$ -term will be small due to the large energy denominators (Fig. 10(a)). If  $|K\rangle$  is close in energy to either the excited state or the ground state, but high enough in energy that it is not Boltzmann populated, there can be a significant  $\mathcal{B}$ -term MCD intensity component to the  $A \rightarrow J$  transition (Fig. 10(b)) [177,178].

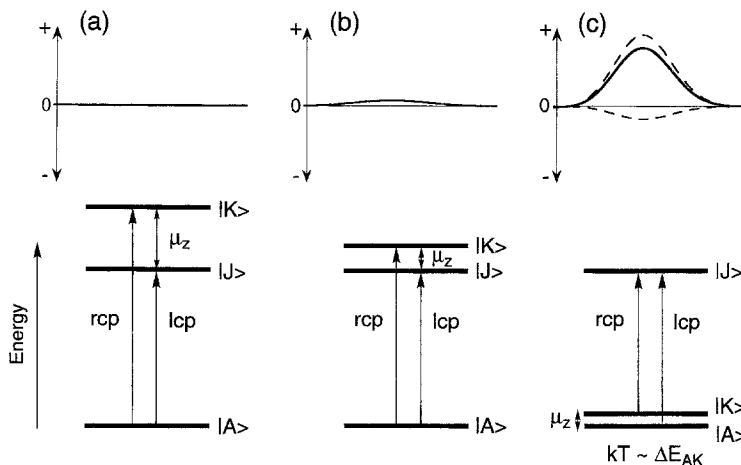


Fig. 10. MCD  $\mathcal{B}$ -term mechanism. (a) When an intermediate state ( $|K\rangle$ ) is significantly higher in energy than both the ground and excited states, the mixing between them is weak and the resulting  $\mathcal{B}$ -term is negligible. (b) If an intermediate state is near the excited state, the interaction is larger and results in a weak feature with an absorption bandshape that has temperature-independent MCD intensity which is linear with magnetic field. (c) If an intermediate state is within  $kT$  of the ground state, the mixing is substantial and the intermediate state itself will be thermally populated, resulting in an intense temperature-dependent  $\mathcal{B}$ -term which qualitatively resembles a  $\mathcal{C}$ -term.



Such a  $\mathcal{B}$ -term can be distinguished from an  $\mathcal{A}$ -term by its bandshape and from a  $\mathcal{C}$ -term by its temperature-independent behavior. Fig. 10(c) demonstrates a third situation, in which the intermediate state  $|K\rangle$  lies at low-energy and strongly interacts via the magnetic field with the ground state  $|A\rangle$  [179]. This case can exhibit high MCD intensity which will be temperature-dependent (see Section 3.3.4).

These expressions for the MCD  $\mathcal{A}$ -,  $\mathcal{B}$ -, and  $\mathcal{C}$ -terms assume that both the light propagation and magnetic field directions are along the molecular  $z$ -axis, which would be true for an oriented axial single crystal. However, most ferrous protein systems and related model complexes are studied as randomly oriented glasses or mulls, so that the random orientation of the magnetic field and light directions with respect to the ensemble of molecules in the sample must be taken into account [173]. Eqs. (7), (8) and (10) can be rewritten for randomly oriented centers to give Eqs. (11), (12) and (13).

$$\bar{\mathcal{A}}_1 = \frac{i}{3|d_A|} \sum (\langle J|\vec{\mu}|J\rangle - \langle A|\vec{\mu}|A\rangle) \cdot (\langle A|\vec{m}|J\rangle \times \langle J|\vec{m}|A\rangle) \quad (11)$$

$$\begin{aligned} \bar{\mathcal{B}}_0 = \frac{2}{3|d_A|} \operatorname{Im} \sum \left[ \sum_{K(K \neq J)} \frac{\langle J|\vec{\mu}|K\rangle}{\Delta E_{KJ}} \cdot (\langle A|\vec{m}|J\rangle \times \langle K|\vec{m}|A\rangle) \right. \\ \left. + \sum_{K(K \neq A)} \frac{\langle K|\vec{\mu}|A\rangle}{\Delta E_{KA}} \cdot (\langle A|\vec{m}|J\rangle \times \langle J|\vec{m}|K\rangle) \right] \quad (12) \end{aligned}$$

$$\bar{\mathcal{C}}_0 = \frac{-i}{3|d_A|} \sum \langle A|\vec{\mu}|A\rangle \cdot (\langle A|\vec{m}|J\rangle \times \langle J|\vec{m}|A\rangle) \quad (13)$$

All three of these expressions contain the dot product of a magnetic dipole vector ( $\vec{\mu} = \vec{L} + 2\vec{S}$ ) with the cross product between two electric dipole vectors. The expansion of the  $\mathcal{C}$ -term is given in Eq. (14), and the expansions of the  $\mathcal{A}$ - and  $\mathcal{B}$ -term expressions are similar.

$$\begin{aligned} \mathcal{C}_0 = \frac{-i}{3|d_A|} \operatorname{Im} \sum [ \langle A|\mu_x|A\rangle (\langle A|m_y|J\rangle \langle J|m_z|A\rangle - \langle A|m_z|J\rangle \langle J|m_y|A\rangle) \\ + \langle A|\mu_y|A\rangle (\langle A|m_x|J\rangle \langle J|m_z|A\rangle - \langle A|m_z|J\rangle \langle J|m_x|A\rangle) \\ + \langle A|\mu_z|A\rangle (\langle A|m_x|J\rangle \langle J|m_y|A\rangle - \langle A|m_y|J\rangle \langle J|m_x|A\rangle) ] \quad (14) \end{aligned}$$

Eq. (14) expresses the  $\mathcal{C}$ -term intensity as the sum of three terms, each containing the product of a ground-state Zeeman term with the electric dipole matrix elements between the ground and excited states in the two molecular directions orthogonal to the Zeeman direction. Therefore, non-zero  $z$ -polarization will now contribute to the MCD intensity, but with the magnetic field perpendicular to the molecular  $z$ -axis.

Ferrous complexes have spin degenerate ground states which will split in a magnetic field and can acquire  $\mathcal{C}$ -term MCD intensity at low temperature through spin-orbit coupling. Zero-field splitting as described in Fig. 6 complicates this picture and removes some of the ground-state degeneracy. However, off-diagonal Zeeman

coupling of these levels produces  $\mathcal{B}$ -terms which are often temperature-dependent. Thus, low-temperature MCD allows one to observe excited states with high sensitivity and the temperature dependence of the MCD intensity allows one to probe the ground-state ZFS through  $\mathcal{C}$ - and  $\mathcal{B}$ -term mechanisms (see Section 3.3).

### 3.1.3. Experimental considerations

It is beyond the scope of this review to discuss the instrumentation used to acquire CD/MCD spectra, but the reader is referred to excellent reviews on this subject [180,181]. Sample preparation, however, requires some consideration which is summarized here. Because CD and MCD spectroscopies measure the difference between lcp and rcp absorption, the sample must meet two basic requirements: it must transmit light throughout the spectral region of interest, and it must not depolarize the incident light.

The vibrational overtone bands of O–H and C–H stretches dominate the transmission spectra of all proton-containing complexes and, in fact, can strongly block light transmission throughout much of the NIR region. For aqueous protein solutions, this problem can be overcome by exchanging deuterium oxide for water, which extends the transmission window from  $\sim 1400$  nm to  $\sim 1900$  nm. Low-temperature MCD experiments involve cooling a sample to liquid helium temperatures, which is problematic because frozen protein solutions form a snow, leading to both transmission loss and depolarization. Therefore, a glassing agent such as glycerol or ethylene glycol is added to the protein solution. Care must be taken to ensure that the glassing agent does not chemically alter the protein by confirming that the room temperature CD spectrum is invariant to the addition of the glassing agent. The amount of strain induced in the glass by cooling to low temperature is estimated by monitoring the difference in the CD intensity of a nickel tartrate standard placed just before and just after the sample compartment [177]. The low-temperature natural CD of the protein is difficult to observe above the strain-induced baseline shift. In order to observe the MCD spectrum of the protein, this field-independent baseline must be subtracted from the measured intensity. If the low-temperature MCD bands are significantly shifted in energy from the room-temperature CD transitions, the possibility of site perturbations due to temperature effects must also be considered.

These same criteria must be applied to the study of model complexes. Only uniaxial or cubic single crystals will not depolarize the incident light. If a crystal is uniaxial, both the magnetic field and the incident light must be directed along the unique crystallographic axis; for biaxial crystals the optic axis will, in general, be temperature- and wavelength-dependent. As this is not typically the case, a model complex is often ground into a mull using a mulling agent which must transmit NIR light, must not dissolve the crystal or powder, and must not depolarize the incident light. Transmission is best through a fluorocarbon grease such as Fluorolube<sup>®</sup>, although the sharp vibrational overtone bands present in a hydrocarbon or silicone grease are easily distinguished from the broad ligand field transitions of the ferrous sample. Dissolution of a model complex in the mulling agent can be checked by examining the mull under a microscope, the consequence being that the crystallographically defined structural information may no longer apply. Depolarization of the incident

light is avoided if the sample particle size is smaller than the wavelength of the exciting light (300–2000 nm). Alternatively, a model complex can be dissolved in a non-absorbing glassing agent and handled analogously to the protein glasses (vide supra), although the spectral features of the complex in the glass must be identical to the those of the mull to verify that the structure has not changed in solution.

### 3.2. Ligand field theory of excited-state d-orbital splittings

MCD transitions observed in the NIR region give the d-orbital splittings for a non-heme  $\text{Fe}^{2+}$  center which are directly correlated to the geometry of the site. Ligand field calculations [182] give the theoretical energy levels and wave functions of the d-orbitals for specific ligand arrangements. Fitting the experimentally observed excited-state splittings with a ligand field calculation provides an estimate of the ground-state splittings. These ligand field calculations are especially useful in describing trends in the d-orbital splittings due to differences in coordination number and site geometry and in interpolating between limiting geometries in distorted sites, as in proteins.

In the crystal field approximation, the ligands are treated as point charges which perturb the d-orbitals due to electrostatic interactions based on the ligands' geometric arrangement around the metal. The secular determinant of degenerate perturbation theory,  $|H_{pq} - S_{pq}E_k| = 0$ , is calculated using the real d-orbitals ( $p$  and  $q$ ) as the basis set. Because the d-orbitals form an orthonormal set, the overlap integral  $S_{pq}$  is zero unless  $p = q$ , in which case  $S_{pq} = 1$ , so that the solving the secular determinant reduces to evaluating the matrix elements  $H_{pq}$ . Following Companion and Komarynsky [182], the general expression for  $H_{pq}$  is given by Eq. (15).

$$\langle \psi_p | \hat{\mathcal{H}} | \psi_q \rangle = \sum_{i=1}^N \sum_{l=0,2,4} \sum_{m=-l}^{m=l} \frac{4\pi Z_i e^2}{2l+1} \times Y_{lm}^*(\theta_i, \phi_i) \int \psi_p^* \left[ \frac{r_{<}^l}{r_{>}^{l+1}} \right]_i Y_{lm}(\theta, \phi) \psi_q dv \quad (15)$$

$N$  is the number of ligands ( $i$ ),  $Z_i$  is the effective nuclear charge,  $l$  and  $m$  are the angular momentum quantum numbers of the spherical harmonics,  $Y_{lm}$ , and  $r_{<}$  and  $r_{>}$  are the shorter and longer radial distance vectors, respectively, connecting the metal to the electron and to the ligand. The matrix elements of the secular determinant are given in terms of  $D_{lm} = \sum_{i(\text{ligands})} D_{lm}^i$  and  $G_{lm} = \sum_{i(\text{ligands})} G_{lm}^i$  as described in Refs. [27,182]. In the  $D_{lm}^i$  and  $G_{lm}^i$  terms, the radial part of the integral is separated from the angular part and is contained in the parameter  $\alpha_l^i$ , which is defined in Eq. (16).

$$\alpha_l^i = Z_i e^2 \int_0^\infty R_{3d}^2 \left[ \frac{r_{<}^l}{r_{>}^{l+1}} \right]_i r^2 dr \quad (16)$$

The elements of the secular determinant can be calculated given the angular coordi-

nates of the ligands and the radial parameters  $\alpha_0$ ,  $\alpha_2$ , and  $\alpha_4$  for each ligand  $i$ . The energies and wave functions of the d-orbitals are then obtained by diagonalizing the Hamiltonian matrix.

Because the electrostatic crystal field model does not give good agreement with experiment if the radial integrals are calculated using appropriate wave functions, a ligand field model is generally used in which the  $\alpha_i^l$  parameters are obtained experimentally through correlation with data on model complexes. The parameter  $\alpha_0$  contributes equally to all diagonal elements of the matrix and does not affect the d-orbital splittings and can therefore be eliminated. A set of reasonable values for  $\alpha_2$  and  $\alpha_4$  has been obtained for nitrogen and oxygen ligation appropriate to non-heme ferrous enzymes [183], and these parameters which were used as starting values for the calculations presented here are given in Table 3.

Energy level diagrams resulting from ligand field calculations on a six-coordinate  $\text{Fe}^{2+}$  site are shown in Fig. 11, where a metal environment of six equivalent oxygen ligands has been considered. A pure octahedral geometry (Fig. 11(A)) produces a triplet ground state ( $t_{2g}$  one-electron d-orbitals giving the  $^5T_{2g}$  many-electron ground state) and a doublet excited state ( $e_g$  d-orbitals giving the  $^5E_g$  excited state) which are split by  $\sim 10\,000\text{ cm}^{-1}$ , corresponding to  $10Dq(O_h)$ . A weak-axial tetragonal distortion (Fig. 11(B)), considered as an elongation along one of the  $C_4$  axes, causes the excited state to split by  $\sim 2000\text{ cm}^{-1}$ . This weak-axial distortion also splits the ground state in such a way as to make the degenerate ( $d_{xz}$ ,  $d_{yz}$ ) orbitals lowest, producing a  $-D$  system as described in Section 3.4.1.2. A strong-axial distortion (Fig. 11(C)), considered as compression along one of the  $C_4$  axes, also causes the excited state to split by  $\sim 2000\text{ cm}^{-1}$ , but now the  $d_{xy}$  orbital is lowest, corresponding to a  $+D$  system (see Section 3.4.1.1). Similarly, a trigonal compression along a  $C_3$  axis splits the  $^5T_{2g}$  orbitals to produce an orbitally non-degenerate ground state indicative of a  $+D$  system. Although a trigonal distortion does not remove the degeneracy of the  $^5E_g$  excited state, a rhombic distortion (appropriate for low-symmetry protein sites) added to a trigonal compression causes the  $^5E_g$  state to split by  $\sim 1000\text{ cm}^{-1}$  as shown in Fig. 11(D) (where  $z$  is now defined along the  $C_3$  axis). Thus, distorted octahedral complexes will display two excited-state d→d transitions at  $\sim 10\,000\text{ cm}^{-1}$  which are split by  $\sim 1000\text{--}2000\text{ cm}^{-1}$ .

Fig. 12 shows the results of ligand field calculations on a square pyramidal five-coordinate  $\text{Fe}^{2+}$  complex with all O-type ligands and a unique axial ligand. Square

Table 3  
Ligand field parameters for common non-heme ferrous ligands

Fe–L (bond length)	Type of ligand	$\alpha_2\text{ (cm}^{-1}\text{)}$	$\alpha_4\text{ (cm}^{-1}\text{)}$
Fe–N (2.17 Å)	imidazole	19 850	7850
Fe–N (2.21 Å)	imidazole	18 520	6170
Fe–O (2.08 Å)	water	17 300	5760
Fe–O (2.14 Å)	water	18 700	5600
Fe–O	carboxylate	17 000	5800
Fe–O	amide	14 900	4800

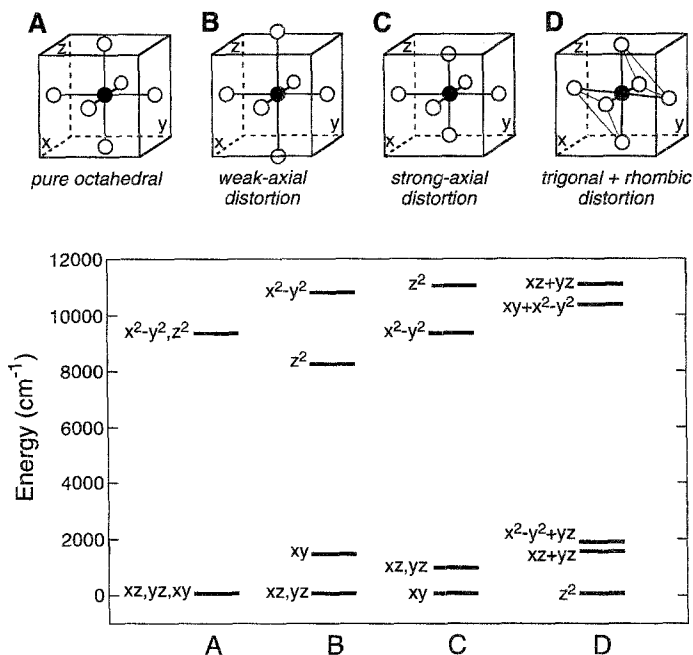


Fig. 11. Calculated energy level diagrams for a six-coordinate  $\text{Fe}^{2+}$  site. d-orbital energy splittings of an  $\text{Fe}^{2+}$  center with six O-type ligands under the following geometries: A, pure octahedral; B, a weak-axial tetragonal distortion; C, a strong-axial tetragonal distortion; D, a trigonal and rhombic distortion. d-orbital wave functions are written in a tetragonal basis set ( $z$  along  $C_4$ ) for A–C and in a trigonal basis set ( $z$  along  $C_3$ ) for D.

pyramidal geometry can be achieved by removing one ligand from an octahedron, with the metal remaining in the equatorial plane (Fig. 12(A)). This arrangement has a very large splitting ( $\sim 10\,000\text{ cm}^{-1}$ ) of the ( $d_{x^2-y^2}$ ,  $d_{z^2}$ ) orbitals. However, with the removal of one axial ligand, the metal moves out of the equatorial plane toward the remaining axial ligand, resulting in a stronger bond. The ( $d_{x^2-y^2}$ ,  $d_{z^2}$ ) splitting is reduced to  $\sim 7000\text{ cm}^{-1}$  for a puckered square pyramid with the metal  $10^\circ$  out of the equatorial plane, as shown in Fig. 12(B). Moving the metal  $15^\circ$  out of the plane (Fig. 12(C)) further reduces this splitting to  $\sim 5000\text{ cm}^{-1}$ . In each of these cases, the ground state is the orbitally degenerate ( $d_{xz}$ ,  $d_{yz}$ ) level associated with a weak-axial system. As the metal is moved further toward the axial ligand, a strong-axial system is reached which has the non-degenerate  $d_{xy}$  orbital lowest in energy, as shown in Fig. 12(D); the excited-state splitting in this case is  $< 5000\text{ cm}^{-1}$ . In general, five-coordinate square pyramidal sites have one  $d \rightarrow d$  transition above  $10\,000\text{ cm}^{-1}$  and one transition  $\sim 5000\text{--}7000\text{ cm}^{-1}$  to lower energy, although it is important to note that the position of the metal above the equatorial plane and the strength of the  $\text{M-L}_{\text{axial}}$  bond will affect the splitting of the excited state as well as the nature of the ground state.

A five-coordinate square pyramidal geometry can be distorted to a trigonal bipyra-

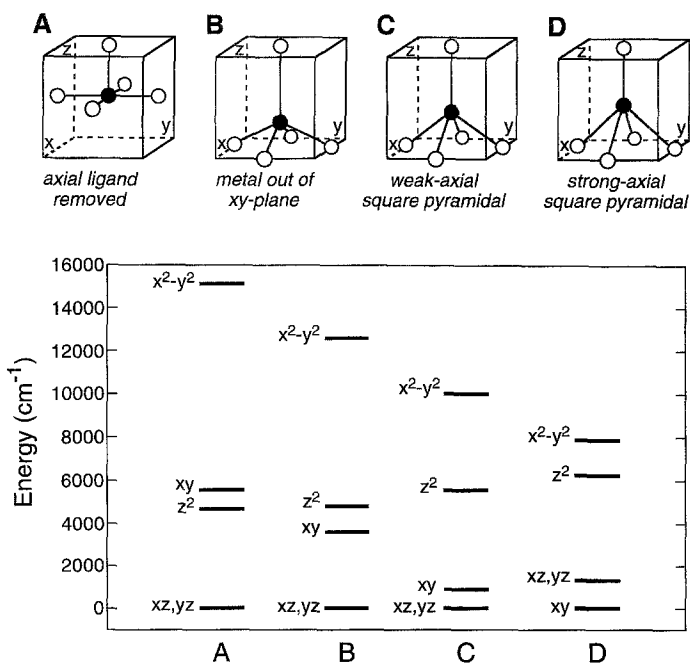


Fig. 12. Calculated energy level diagrams for a five-coordinate  $\text{Fe}^{2+}$  square pyramidal site, moving the metal out of the equatorial plane. d-orbital energy splittings of a square pyramidal  $\text{Fe}^{2+}$  center with five O-type ligands and the metal pulled out of the equatorial plane by: A,  $0^\circ$  (removal of one ligand from a pure octahedron); B,  $10^\circ$ ; C,  $15^\circ$ ; D,  $17.5^\circ$  (resulting in a strong-axial system). All orbital wave functions are written in a tetragonal basis set.

midial structure through an intramolecular rearrangement which maintains  $C_{2v}$  symmetry throughout, known as the Berry pseudo-rotation [184]. This distortion is considered in the energy level diagrams in Fig. 13, which treat the rearrangement of five O-type ligands around a metal center. Fig. 13(A) shows the d-orbital splittings for a puckered square pyramidal geometry with a ( $d_{xz}$ ,  $d_{yz}$ ) ground state, where the d-orbitals are defined in a tetragonal basis set (i.e., quantized along the  $C_4$  axis). In Fig. 13(B), the energies of the higher-energy orbitals do not change much with a  $C_{2v}$  distortion, but the wave functions of the excited states are now mixed and the degeneracy of the ( $d_{xz}$ ,  $d_{yz}$ ) orbitals is removed. When a pure trigonal bipyramidal arrangement is achieved (Fig. 13(C)), the highest-lying orbital is lowered in energy relative to the square pyramidal case and the wave functions are mixed in the tetragonal basis set. The second-highest-lying d-orbital for trigonal bipyramidal symmetry is also lowered in energy relative to the square pyramidal case, and the lowest-lying orbitals are again degenerate, composed of the ( $d_{xy}$ ,  $d_{yz}$ ) pair in a tetragonal basis and the ( $d_{xz}$ ,  $d_{yz}$ ) pair in a trigonal basis ( $z$  along  $C_3$ ), as shown in Fig. 13(C) and 13(D), respectively. Thus, the energies of both the excited-state  $d \rightarrow d$  transitions are lowered upon going from square pyramidal to trigonal bipyramidal geometry.

Removing two *trans* axial ligands from a pure octahedron produces a square

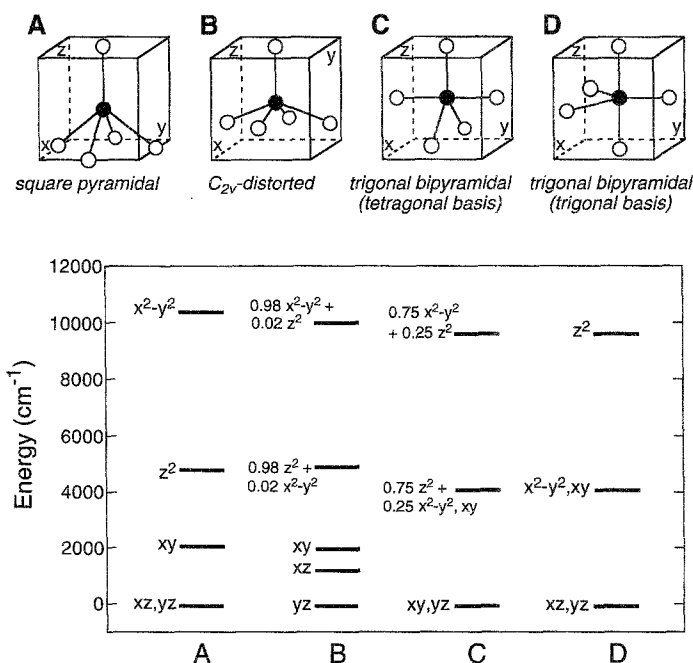


Fig. 13. Calculated energy level diagrams for a five-coordinate  $\text{Fe}^{2+}$  site with square pyramidal to trigonal bipyramidal geometries. d-orbital energy splittings of an  $\text{Fe}^{2+}$  center with five O-type ligands under the following geometries: A, puckered square pyramidal; B,  $C_{2v}$ -distorted square pyramidal; C and D, trigonal bipyramidal. The orbital wave functions in A–C are written in a tetragonal basis set and those in D in a trigonal basis set.

planar geometry. The ligand field results for four equivalent O-type ligands in a square planar arrangement are given in Fig. 14(A), which shows that the two highest-lying excited states are at much higher energy than has been found for either five- or six-coordinate sites. A  $D_{2d}$ -distortion of square planar geometry to produce a flattened tetrahedron (Fig. 14(B)) greatly compresses the d-orbital splittings so that the two highest-lying excited states are now at  $\sim 4000\text{--}7000\text{ cm}^{-1}$  and are separated by only a few thousand wavenumbers. The lowest-energy orbital remains  $d_{z^2}$  along a  $D_{2d}$ -distortion coordinate from square planar to tetrahedral geometry [183]. A pure tetrahedral ligand arrangement (Fig. 14(C)) gives doubly degenerate ( $d_{xz}$ ,  $d_{yz}$ ) orbitals lowest in energy and triply degenerate ( $d_{xy}$ ,  $d_{yz}$ ,  $d_{xz}$ ) orbitals  $\sim 5000\text{ cm}^{-1}$  above, corresponding to  $10Dq(T_d) = -4/9\ 10Dq(O_h)$ . A tetragonally-distorted, elongated tetrahedron (Fig. 14(D)) produces d-orbital splittings similar to the flattened tetrahedron in Fig. 14(B), but now the  $d_{x^2-y^2}$  orbital is lowest. Because square planar geometry is not common for high-spin  $\text{Fe}^{2+}$  and tetrahedral symmetry will be lowered due to Jahn-Teller effects, the energy level diagrams calculated for the distorted tetrahedra provide a good description of four-coordinate sites, for which an orbitally non-degenerate ground state and two low-energy ( $< 7000\text{ cm}^{-1}$ ) d→d transitions are expected.

These ligand field calculations provide trends in the excited-state splittings for

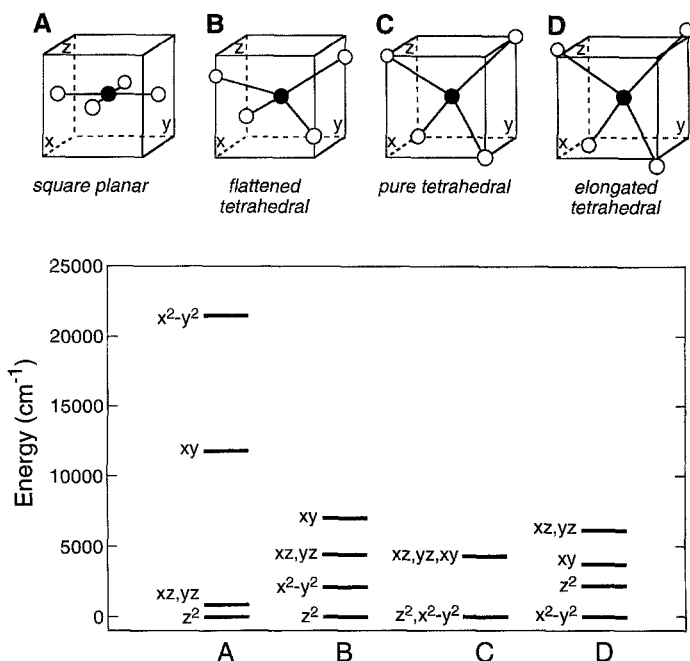


Fig. 14. Calculated energy level diagrams for a four-coordinate  $\text{Fe}^{2+}$  site. d-orbital energy splittings of an  $\text{Fe}^{2+}$  center with four O-type ligands under the following geometries: A, square planar; B, flattened tetrahedral; C, pure tetrahedral; D, elongated tetrahedral. All orbital wave functions are written in a tetragonal basis set with the orbitals in A rotated  $45^\circ$  relative to those in B–D.

different coordination numbers and geometries relevant to non-heme iron enzymes. In general, six-coordinate sites exhibit two NIR transitions  $\sim 10\,000\text{ cm}^{-1}$  which are split by  $\sim 2000\text{ cm}^{-1}$ ; five-coordinate square pyramidal sites exhibit one band at  $>10\,000\text{ cm}^{-1}$  and one at  $>5000\text{ cm}^{-1}$  while trigonal bipyramidal sites show one band at  $<10\,000\text{ cm}^{-1}$  and a second band  $<5000\text{ cm}^{-1}$  (which may lie too low in energy to be detected by NIR MCD); and four-coordinate distorted tetrahedral sites exhibit two bands in the  $4000\text{--}7000\text{ cm}^{-1}$  region. These calculations also provide information about the ground-state splittings which can be compared with experimentally-derived ground-state information (Section 3.4). However, while the ligand field calculations are generally consistent with experimental results for excited-state splittings (see Table 2), this model does not consider specific  $\sigma$ - and  $\pi$ -bonding interactions so that the calculated  $t_{2g}$  splittings, which are particularly sensitive to  $\pi$ -bonding effects [121], may not be consistent with experiment. Additionally, effects of mixed ligand geometries should be considered, and the  $\alpha_2$  and  $\alpha_4$  parameters obtained through fits to model complexes are not necessarily transferable to other ferrous sites [185].

The excited-state spectral data for FeSOD shown in Fig. 7 can now be analyzed by applying these ligand field correlations between excited-state transition energies and site geometry. The absorption (Fig. 7(a)), CD (Fig. 7(b)), and MCD (Fig. 7(c))



spectra all show the presence of one broad feature near  $10\,500\text{ cm}^{-1}$ , and a second transition observed in the absorption spectrum is centered at approximately  $5000\text{ cm}^{-1}$  (low-energy CD and MCD spectra are not shown as the instrument available at that time did not extend below  $\sim 9000\text{ cm}^{-1}$ ; current instrumentation now probes this region). The presence of two peaks in these energy regions indicates a five-coordinate site; further, the geometry can be assigned as square pyramidal since the  $^5\text{E}_g$  transitions are observed at  $>10\,000\text{ cm}^{-1}$  and  $\sim 5000\text{ cm}^{-1}$ .

### 3.3. MCD saturation magnetization: determination of ground-state spin Hamiltonian parameters

Through an analysis of the VTVH MCD data, the ground-state spin Hamiltonian parameters for a non-heme  $\text{Fe}^{2+}$  center with  $S=2$  (Fig. 6) can be obtained and can provide complementary information to the excited-state spectra. Further, the  $^5\text{T}_{2g}$  splittings (i.e., the  $d_{xz}$ ,  $d_{yz}$ ,  $d_{xy}$  orbital splittings) which lead to the  $S=2$  spin Hamiltonian parameters (Section 3.4) reflect ligand  $\pi$ -interactions and thus provide additional information about the metal environment.

Saturation magnetization data, which consist of MCD intensities collected over a range of temperatures and magnetic fields at a fixed wavelength corresponding to a transition, are often presented in two formats. The first plots the observed MCD intensity versus  $\beta H/2kT$ , where each curve (isotherm) represents one temperature for a range of fields. The  $\beta H/2kT$  plot for FeSOD is presented in Fig. 7(d) and shows that the isotherms do not superimpose, indicating unusual saturation behavior relative to that of a simple Kramers doublet as described in Section 3.3.1. The second format plots the observed MCD intensity versus  $1/kT$ , where each curve represents one magnetic field for a range of temperatures; this presentation allows the magnetic field effects to be separated from the temperature effects. The lowest-temperature region of the  $1/kT$  plot for FeSOD, shown in Fig. 7(e), is particularly interesting: as the magnetic field increases with equal increments, the intensity intervals decrease, indicating a non-linear magnetic field effect. In the following sections, we consider this saturation magnetization behavior by systematically investigating the effects of various ground-state parameters on the MCD intensity. Simulated intensities have been calculated for a fixed set of temperatures (1.7, 1.9, 2.4, 2.7, 4.2, 5.0, 7.0, 11.0, 25.0 K) and magnetic fields (up to 7.0 Tesla, with even increments of 0.7 T) to approximate typical experimental conditions.

#### 3.3.1. Effective Kramers doublet

We first consider the VTVH MCD behavior of an effective Kramers doublet, i.e., a doubly degenerate ground state which is not split in energy in the absence of a magnetic field. This would correspond to an  $S=2$ ,  $M_S=\pm 2$  ground state (i.e.,  $D<0$  and  $E=0$  in Fig. 6) with an effective  $g_{\parallel}$  of 8 and a small, but non-zero,  $g_{\perp}$ .

**3.3.1.1. *xy*-Polarization effects** The experimentally observed MCD intensity corresponds to *xy*-polarized transitions (vide supra), and the *xy*-polarized  $\mathcal{G}$ -term MCD

intensity for a Kramers doublet [171] is given by Eq. (17), which includes orientation averaging.

$$\Delta\varepsilon = A_{\text{satlim}} \int_0^{\pi/2} \cos \theta \sin \theta \tanh \left[ \frac{g_{\parallel} \beta H \cos \theta}{2kT} \right] d\theta \quad (17)$$

In Eq. (17),  $A_{\text{satlim}}$  is the maximum  $\mathcal{C}$ -term intensity at saturation,  $\beta$  is the Bohr magneton,  $H$  is the magnetic field in Tesla,  $\theta$  is the angle between the applied magnetic field and the ZFS axis,  $k$  is Boltzmann's constant, and  $T$  is the absolute temperature. Varying the value of  $A_{\text{satlim}}$  serves only to scale the magnitude of the MCD intensity and does not qualitatively affect the data. Varying the magnitude  $g_{\parallel}$ , however, does affect the saturation magnetization behavior. Fig. 15 shows  $\beta H/2kT$  and  $1/kT$  plots for an isolated effective Kramers doublet with a fixed value of  $A_{\text{satlim}}$  and  $g_{\parallel} = 8.0$  or  $4.0$  (for demonstrative purposes). Both of the  $\beta H/2kT$  plots in Fig. 15, left, show that all of the isotherms superimpose, as would be expected for a Kramers system from Eq. (17). The rate at which the intensity saturates, i.e., the steepness of the slope at low field, increases as  $g_{\parallel}$  increases. The  $1/kT$  plots (Fig. 15, right) show that the intensity is saturated at low temperatures and at high fields, where the curves have leveled off, and in this region the curves superimpose.

**3.3.1.2. z-Polarization effects** If an MCD transition contains z-polarization, the orientation averaged MCD intensity expression (Eq. (14)) must be expanded to include the effects of both  $g_{\perp}$  and  $M_z/M_{xy}$ , the ratio of the z-polarized to the xy-polarized transition dipole moments. Eq. (18), derived from Ref. [186], gives the

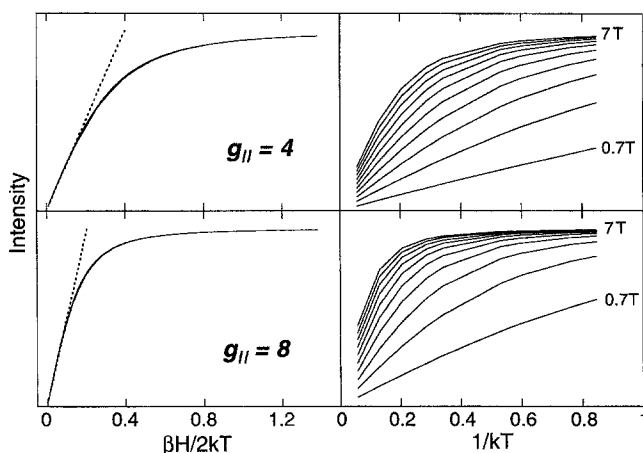


Fig. 15. Effects of the magnitude of  $g_{\parallel}$  on an effective Kramers doublet.  $\beta H/2kT$  plots (left) and  $1/kT$  plots (right) of simulated MCD intensities for an isolated effective Kramers doublet with  $A_{\text{satlim}} = 100.0$  and  $g_{\parallel} = 4.0$  (top) and  $8.0$  (bottom). Increasing  $g_{\parallel}$  causes an increase in the rate of saturation, as evidenced by a steeper rise on the left side of the plots (dashed lines).

MCD intensity expression for an isolated Kramers doublet containing both  $xy$ - and  $z$ -polarization [187,188].

$$\Delta\varepsilon = A_{\text{satlim}} \left\{ \int_0^{\pi/2} \frac{\cos^2 \theta \sin \theta}{\Gamma} g_{\parallel} \cdot \tanh \left[ \frac{\Gamma \beta H}{2kT} \right] d\theta - \sqrt{2} \frac{M_z}{M_{xy}} \int_0^{\pi/2} \frac{\sin^3 \theta}{\Gamma} g_{\perp} \cdot \tanh \left[ \frac{\Gamma \beta H}{2kT} \right] d\theta \right\} \quad (18)$$

where

$$\Gamma = \sqrt{(g_{\parallel} \cos \theta)^2 + (g_{\perp} \sin \theta)^2}$$

The effects of  $z$ -polarization on the saturation behavior can be probed by treating  $A_{\text{satlim}}$ ,  $g_{\parallel}$ ,  $g_{\perp}$ , and  $M_z/M_{xy}$  as parameters and calculating a set of MCD intensities.

Fig. 16 shows the  $\beta H/2kT$  and  $1/kT$  plots for calculations in which  $A_{\text{satlim}}$  has been fixed,  $g_{\parallel} = 8.0$ ,  $g_{\perp} = 0.25$  (based on calculations of the perpendicular Zeeman

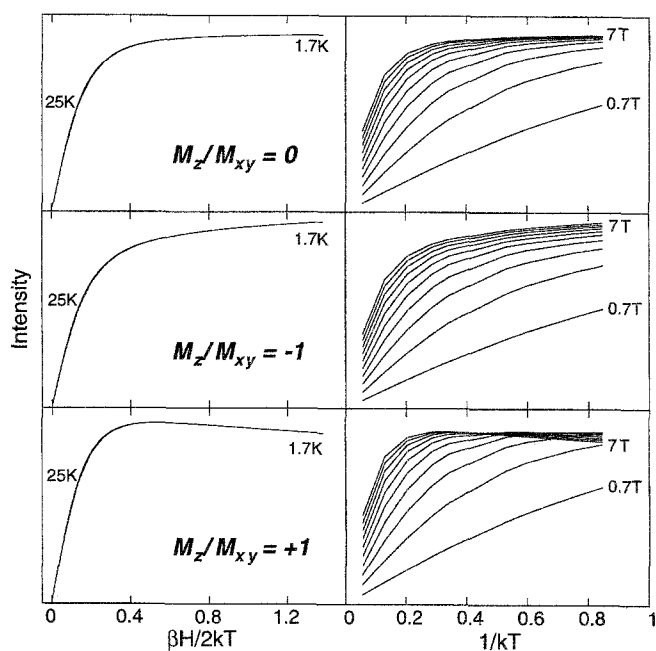


Fig. 16. Effects of  $z$ -polarization on an effective Kramers doublet. Simulated MCD intensities for an isolated effective Kramers doublet with  $A_{\text{satlim}} = 100.0$ ,  $g_{\parallel} = 8.0$ , and the following  $z$ -polarization parameters:  $g_{\perp} = 0.0$  and  $M_z/M_{xy} = 0.0$  (top);  $g_{\perp} = 0.25$  and  $M_z/M_{xy} = -1.0$  (middle) and  $+1.0$  (bottom). Non-zero values of  $M_z/M_{xy}$  and  $g_{\perp}$  cause the data to curve upward (negative  $M_z/M_{xy}$ ) or downward (positive  $M_z/M_{xy}$ ) at the saturation limit.

effect for an  $S = 2$  spin Hamiltonian), and  $M_z/M_{xy} = 0.0, -1.0$  (the  $z$ - and  $xy$ -polarized transition dipole moments have opposite signs), or  $+1.0$  (same signed transition dipole moments). The first set of calculations, with  $M_z/M_{xy} = 0.0$  (Fig. 16, top), corresponds to the  $xy$ -polarized case described above. For a non-zero polarization ratio of  $-1.0$  (Fig. 16, middle), the isotherms still superimpose, but are angled upward at high field. The corresponding  $1/kT$  plot also shows that the intensity does not saturate. Similarly, when the polarization ratio is  $+1.0$  (Fig. 16, bottom), the isotherms superimpose in the  $\beta H/2kT$  plot, but are angled downward at high field, and the curves in the  $1/kT$  plot show a small incremental decrease in intensity instead of saturating at lowest-temperature.

**3.3.1.3. Linear, temperature-independent  $\mathcal{B}$ -term effects** Linear, temperature-independent  $\mathcal{B}$ -term intensity, which arises from field-induced mixing between the ground state and high-lying excited states (vide supra), can also affect the MCD saturation magnetization data. The inclusion of a linear  $\mathcal{B}$ -term is equivalent to adding (or subtracting, depending on the sign of the  $\mathcal{B}$ -term relative to the  $\mathcal{C}$ -term intensity) a constant amount of MCD intensity to the  $\mathcal{C}$ -term signal for a given magnetic field. This can be accounted for in the expression for the MCD intensity by adding a  $B_0 H$  term [173] to Eq. (17) for purely  $xy$ -polarized transitions or to the end of Eq. (18) for both  $xy$ - and  $z$ -polarizations, where  $B_0$  indicates the magnitude of the ground-state linear  $\mathcal{B}$ -term and  $H$  is the magnetic field.

Fig. 17 shows the  $\beta H/2kT$  and  $1/kT$  plots for an isolated effective Kramers doublet with  $\mathcal{B}$ -term contributions of 0.0,  $+2.0$ ,  $+5.0$ , and  $-2.0\%$  (where the  $\mathcal{B}$ -term magnitude is given as a percentage of the  $\mathcal{C}$ -term intensity factor  $A_{\text{satlim}}$ ) and a  $g_{\parallel} = 8.0$ , assuming pure  $xy$ -polarization. Isolated linear  $\mathcal{B}$ -term intensity plotted versus magnetic field would give a set of linear isotherms which are all superimposable; however, when the  $\mathcal{B}$ -term intensity is plotted versus  $\beta H/2kT$ , the slopes of those straight lines change as  $1/T$ . Thus when a linear  $\mathcal{B}$ -term is added to a set of superimposable  $\mathcal{C}$ -term isotherms, such as in Fig. 15, left, and plotted versus  $\beta H/2kT$ , the result is a set of isotherms which no longer superimpose, but instead exhibit the fanning behavior seen in Fig. 17, left. The sign of the  $\mathcal{B}$ -term relative to the  $\mathcal{C}$ -term is reflected in the qualitative pattern of the  $\beta H/2kT$  plots, the same signs giving the positive and the opposite signs giving the negative behavior at the bottom of Fig. 17, left.

Because the linear  $\mathcal{B}$ -term adds a field-dependent amount to the  $\mathcal{C}$ -term intensity, the observed MCD signal does not saturate with increasing magnetic field, but instead continues to increase/decrease by the amount of the  $\mathcal{B}$ -term. This is most clearly seen in the low-temperature regions of the  $1/kT$  plots (Fig. 17, right), where the intensity difference between equal field increments at lowest-temperature is found to be constant and proportional to the magnitude of the  $\mathcal{B}$ -term. A negatively signed  $\mathcal{B}$ -term is also readily recognized by the low-temperature region of the  $1/kT$  plot (Fig. 17, bottom right) where the intensity curves cross each other and are evenly spaced at lowest temperature. It should be noted that while non-zero  $z$ -polarization also produced similar-looking non-saturation behavior in the  $1/kT$  plots, a linear

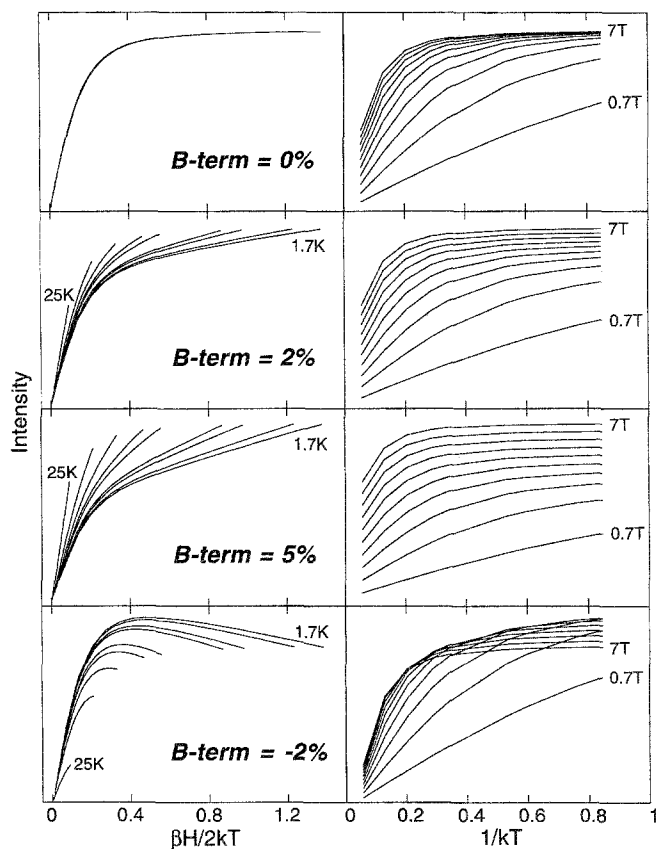


Fig. 17. Effects of a linear, temperature-independent  $\mathcal{B}$ -term on an effective Kramers doublet. Simulated MCD intensities for an isolated effective Kramers doublet with  $A_{\text{satlim}}=100.0$ ,  $g_{\parallel}=8.0$ , and a  $\mathcal{B}$ -term (given as a percentage of  $A_{\text{satlim}}$ ) equal to 0.0% (top), +2.0% (second panel), +5.0% (third panel), and -2.0% (bottom). The inclusion of a linear  $\mathcal{B}$ -term causes fanning behavior in the  $\beta H/2kT$  plots (left) and even intensity spacing between curves of equal field increments in the low-temperature, high-field region of the  $1/kT$  plots (right).

$\mathcal{B}$ -term produces fanning behavior while z-polarization effects still produce superimposing curves in the  $\beta H/2kT$  plots.

### 3.3.2. Population of excited states for negative zero-field splitting

As shown in Fig. 6, there are two excited spin states present in the  $S=2$  spin manifold for negative (and positive) values of the ZFS parameter  $D$ . As the magnitude of  $D$  becomes small and/or high experimental temperatures are used, these excited states become populated and can affect the saturation magnetization behavior. For a Kramers system, the MCD intensity expression given in Eq. (18) can be adapted to include low-lying excited states to produce Eq. (19) [189].

$$\Delta\varepsilon = \sum_i (A_{\text{satlim}})_i \left\{ \int_0^{\pi/2} \frac{\cos^2 \theta \sin \theta}{\Gamma_i} (g_{\parallel i}) \alpha_i d\theta - \sqrt{2} \frac{M_z}{M_{xy}} \int_0^{\pi/2} \frac{\sin^3 \theta}{\Gamma_i} (g_{\perp i}) \alpha_i d\theta \right\} \quad (19)$$

where

$$\Gamma_i = \sqrt{(g_{\parallel i} \cos \theta)^2 + (g_{\perp i} \sin \theta)^2}$$

$$\alpha_i = \frac{e^{-(E_i - \Gamma_i \beta H/2)/kT} - e^{-(E_i + \Gamma_i \beta H/2)/kT}}{\sum_j e^{-(E_j - \Gamma_j \beta H/2)/kT} + e^{-(E_j + \Gamma_j \beta H/2)/kT}}$$

In this expression, the parameters  $A_{\text{satlim}}$ ,  $g_{\parallel}$ , and  $g_{\perp}$  are defined for each of the  $i$  levels and  $E_i$  is defined as the energy of the  $i$ th level above the ground state ( $E_0 \equiv 0.0$ ). For the simulations presented here, we will assume that the MCD transitions are purely  $xy$ -polarized and that the  $\tilde{\mathbf{g}}$  and  $\tilde{\mathbf{D}}$  tensors are both quantized along the molecular  $z$ -axis (cf. Section 3.3.4).

When  $D$  is negative, the doubly degenerate  $M_S = \pm 1$  level lies at  $E_1 = |3D|$  and the singly degenerate  $M_S = 0$  level lies at  $E_2 = |4D|$  above the  $M_S = \pm 2$  doublet ground state. A set of saturation magnetization intensities has been calculated for  $D = -10.0$ ,  $-5.0$ , and  $-2.0 \text{ cm}^{-1}$  using  $g_{\parallel}(\pm 2) = 8.0$ ,  $g_{\parallel}(\pm 1) = 4.0$ , and  $g_{\parallel}(0) = 0.0$ .  $A_{\text{satlim}}$  for the  $M_S = \pm 1$  level was set at half the magnitude of  $A_{\text{satlim}}(\pm 2)$ , and  $A_{\text{satlim}}(0)$  was set to zero as this non-degenerate level does not give rise to  $\mathcal{C}$ -term intensity. The results of these calculations have been plotted versus  $\beta H/2kT$  and  $1/kT$  in Fig. 18.

For  $D = -10.0 \text{ cm}^{-1}$ , the first excited state lies at  $30 \text{ cm}^{-1}$  above the  $M_S = \pm 2$  ground state and will not become significantly populated until the temperature is above 40 K. Because the simulated MCD intensities were calculated only up to 25 K, there is little difference between the data shown in Fig. 18, top, which includes contributions from excited states, and the data for an isolated effective Kramers doublet with  $g_{\parallel} = 8.0$  (Fig. 15, bottom). As the value of  $D$  decreases to  $-5.0 \text{ cm}^{-1}$ , the higher states begin to be populated at lower temperatures. This effect can be seen by the fact that the 25 K and 11 K isotherms in the  $\beta H/2kT$  plot (Fig. 18, middle) no longer superimpose on the rest of the data. When  $D = -2.0 \text{ cm}^{-1}$  (Fig. 18, bottom), this non-superposition effect in the  $\beta H/2kT$  curves is even more pronounced and the isotherms exhibit nesting behavior, which is similar to behavior observed for other metal sites with  $S > 1/2$  and is associated with ZFS of the ground state [190]. The  $1/kT$  saturation behavior (Fig. 18, right) is also affected by the thermal population of excited states. While the low-temperature regions of the  $1/kT$  plots in Fig. 18 are all identical, since only the ground state is populated at lowest temperatures, the high-temperature regions of the  $1/kT$  plots are different for the different values of  $D$ : the smaller the value of  $D$ , the lower the MCD intensity at high-temperature as the excited states become more thermally accessible. In this calcula-

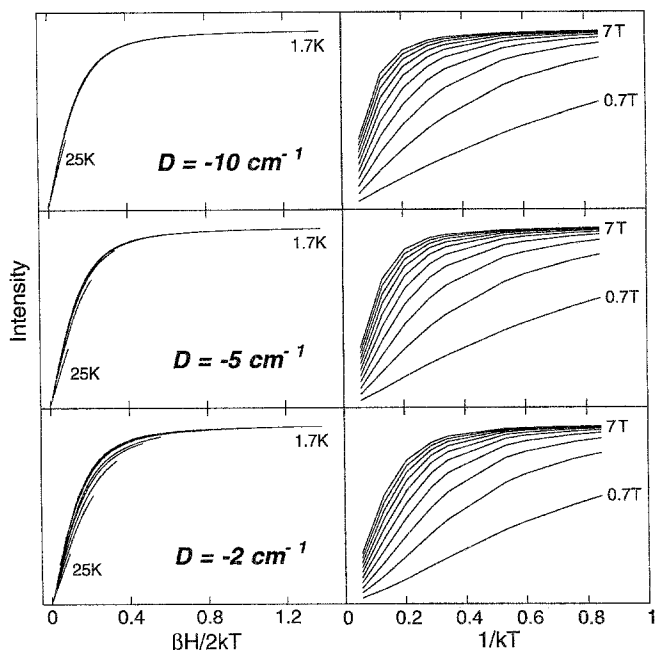


Fig. 18. Effects of excited-state population on a  $-D$  effective Kramers  $S=2$  spin manifold. Simulated MCD intensities calculated with  $g_{\parallel}(\pm 2)=8.0$ ,  $g_{\parallel}(\pm 1)=4.0$ ,  $g_{\parallel}(0)=0.0$ , and  $A_{\text{satlim}}(\pm 2)=100.0$ ,  $A_{\text{satlim}}(\pm 1)=50.0$ , and  $A_{\text{satlim}}(0)=0.0$ . The excited states were positioned at  $E(\pm 1)=|3D| \text{ cm}^{-1}$  and  $E(0)=|4D| \text{ cm}^{-1}$  above the ground state for  $D=-10.0 \text{ cm}^{-1}$  (top),  $-5.0 \text{ cm}^{-1}$  (middle), or  $-2.0 \text{ cm}^{-1}$  (bottom). No  $z$ -polarization or linear  $\mathcal{B}$ -term effects were included. Nesting behavior is observed for small values of  $-D$  as the population of the excited states increases.

tion, the intensity decrease observed at higher temperatures is due to the population of states with lower  $\mathcal{C}$ -term intensities than that of the ground-state: if the  $\mathcal{C}$ -term intensity of the excited states is higher than that of the ground state, then the saturation magnetization intensities would increase as the excited states become thermally populated. It should be noted that these effective Kramers doublet simulations do not accurately describe the FeSOD saturation magnetization data (Fig. 7(d,e)), and we now consider an  $M_S=\pm 2$  non-Kramers doublet model.

### 3.3.3. Negative zero-field splitting: non-Kramers doublet

When the axial ZFS parameter  $D$  is negative, the doubly degenerate  $M_S=\pm 2$  sublevel will be lowest in energy (Fig. 6, right), and thus  $\mathcal{C}$ -term MCD behavior is expected. For a non-Kramers system, the degeneracy of the ground-state doublet is removed in the absence of a magnetic field by rhombic ZFS ( $E\neq 0$ ) which splits the two components by an amount  $\delta$ , as shown in Fig. 19. With this rhombic splitting, the two components of the ground state mix with each other to produce the real wave functions  $|X\rangle$  and  $|Y\rangle$ , which are the normalized, symmetric and anti-symmetric linear combinations of the  $|+2\rangle$  and  $|-2\rangle$  complex wave functions [33] (see Fig. 19). Thus, the rhombic ZFS quenches the angular momentum and

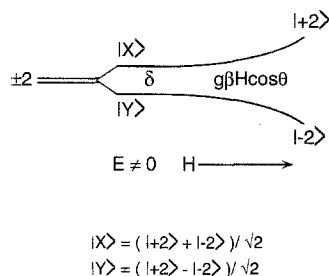


Fig. 19. Splitting of an  $M_s = \pm 2$  non-Kramers doublet under rhombic ZFS and applied magnetic field. For  $D < 0$ , rhombic ZFS splits the  $M_s = \pm 2$  ground state by the amount  $\delta$  and produces the real wave functions  $|X\rangle$  and  $|Y\rangle$ . An applied magnetic field changes the mixing of the wave functions which approach pure  $|+2\rangle$  and  $|-2\rangle$  at high fields and further splits the two levels by  $g\beta H \cos \theta$ .

removes any MCD  $\mathcal{C}$ -term activity, which requires complex wave functions. As an external magnetic field is applied, the two components further split in energy by the amount  $g\beta H \cos \theta$ . This Zeeman perturbation changes the wave functions so that the amount of  $|+2\rangle$  and  $|-2\rangle$  mixing is no longer equal, thus inducing angular momentum and MCD intensity. At high magnetic fields, the wave functions of the two partners of the non-Kramers doublet become pure complex  $|+2\rangle$  and  $|-2\rangle$  in character. In this situation, the MCD intensity saturates as a function of this mixing as well as the thermal population effects described for an effective Kramers doublet (Section 3.3.1). Thus the MCD  $\mathcal{C}$ -term intensity for a non-Kramers doublet ground state arises from unequal mixing between the  $|+2\rangle$  and  $|-2\rangle$  components, and furthermore, this mixing is non-linear with respect to magnetic field.

**3.3.3.1. *xy-Polarization and rhombicity effects*** For a purely *xy*-polarized transition, the MCD  $\mathcal{C}$ -term intensity of an isolated non-Kramers doublet is given by Eq. (20) [33].

$$\Delta \varepsilon = A_{\text{satlim}} \int_0^{\pi/2} \frac{\cos^2 \theta \sin \theta}{\sqrt{\delta^2 + (g_{\parallel} \beta H \cos \theta)^2}} (g_{\parallel} \beta H) \cdot \tanh \left[ \frac{\sqrt{\delta^2 + (g_{\parallel} \beta H \cos \theta)^2}}{2kT} \right] d\theta \quad (20)$$

Experimental MCD data sets (absolute temperature, magnetic field, and MCD intensity) are fit to Eq. (20) by treating  $A_{\text{satlim}}$ ,  $g_{\parallel}$ , and  $\delta$  as variables and fitting the orientation averaged integral with a simplex routine. Since  $A_{\text{satlim}}$  only scales the MCD intensities without qualitatively changing the behavior and the  $g_{\parallel}$  value changes only the rate of saturation (see Section 3.3.1.1), we can fix  $A_{\text{satlim}}$  and  $g_{\parallel}$  and vary the magnitude of  $\delta$  to probe how rhombic ZFS affects the saturation magnetization behavior of an isolated non-Kramers doublet. A set of such calculations has been performed with  $\delta$  values of 0.0, 2.0, 4.0, or 8.0  $\text{cm}^{-1}$  and  $g_{\parallel} = 8.0$ ; the results of these simulations are plotted in Fig. 20.

The  $\beta H / 2kT$  plots in Fig. 20, left, do not show superimposable saturation curves



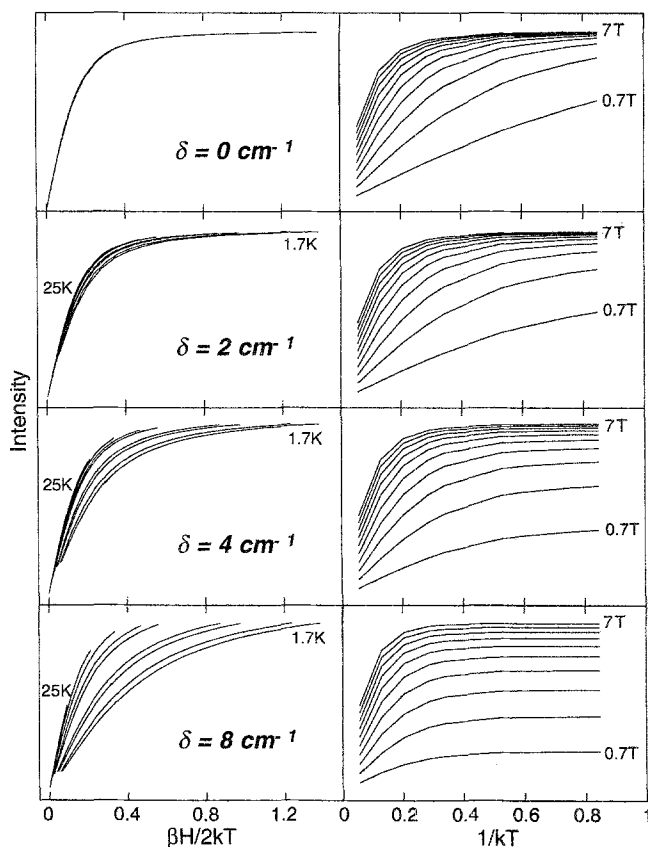


Fig. 20. Effects of rhombicity on a non-Kramers doublet. Simulated MCD intensities for an isolated non-Kramers doublet with  $A_{\text{satlim}}=100.0$ ,  $g_{\parallel}=8.0$ , and  $\delta=0.0\text{ cm}^{-1}$  (top),  $2.0\text{ cm}^{-1}$  (second panel),  $4.0\text{ cm}^{-1}$  (third panel), and  $8.0\text{ cm}^{-1}$  (bottom). Non-zero  $\delta$  values cause decreasing intensity intervals for even magnetic field increments in the low-temperature region of the  $1/kT$  plots (right) instead of superimposing at the saturation limit. Increasing  $\delta$  values cause an increased degree of nesting in the  $\beta H/2kT$  plots (left).

for non-zero values of  $\delta$ , but instead exhibit nesting behavior with the degree of nesting proportional to the magnitude of  $\delta$ . These nesting effects appear to be qualitatively different from any of the other non-superimposing behavior seen for the effective Kramers simulations or those including excited states (*vide supra*). The  $1/kT$  plots of the rhombically-split non-Kramers doublet (Fig. 20, right) indicate the magnitude of  $\delta$ : when the zero-field splitting of the ground-state doublet becomes very large, the  $\mathcal{C}$ -term intensity saturates with decreasing temperature even at low fields, thus the  $1/kT$  curves level off at lower magnetic fields for larger values of  $\delta$ . Vital insight into the nature of the ground-state wave functions can be obtained from the low-temperature, high-field region of the  $1/kT$  plots. For the effective Kramers doublet system (Fig. 15), the saturation limit of the  $1/kT$  plots (low-temperature, high-field region) showed superimposing curves, while for the non-

Kramers case (Fig. 20, right), the saturated intensity curves do not superimpose. Instead, the rhombic ZFS causes the intensity spacing between equal field increments at lowest-temperature to decrease with increasing field, indicating non-linear magnetic field dependence in the ground-state wave functions. Thus the nested saturation magnetization behavior which appears when  $\delta$  is non-zero arises from non-linear field-induced mixing between the partners of the non-Kramers doublet [33].

The simulated data in Fig. 20 look very similar to the FeSOD VTVH data in Fig. 7(d,e). Further, the lowest-temperature regions of the simulated  $1/kT$  plots show the same decreasing intensity intervals for even field increments as does the protein data. Therefore, the non-Kramers doublet model with  $\delta > 0$  and pure  $xy$ -polarization is a good model for the FeSOD saturation magnetization data. The other factors which influence the MCD behavior ( $z$ -polarization, linear  $\mathcal{B}$ -terms, and population of excited states) can now be investigated for a non-Kramers system.

**3.3.3.2.  $z$ -Polarization effects** When  $z$ -polarization is also present (see Eq. (14)), the isolated non-Kramers doublet MCD intensity expression in Eq. (20) must be expanded to include a term which contains  $g_{\perp}$  and is scaled by the electric dipole polarization ratio  $M_z/M_{xy}$ . This is achieved by first diagonalizing the Hamiltonian matrix given in Eq. (21) for a non-Kramers doublet with non-zero values of both  $g_{\parallel}$  and  $g_{\perp}$  [33].

$$\begin{array}{ccc} & |+\rangle & |-\rangle \\ \hat{\mathcal{H}} = \langle +| & \frac{1}{2} (g_{\parallel} \beta H \cos \theta) & \frac{1}{2} (\delta + e^{+i\phi} \sin \theta (g_{\perp} \beta H)) \\ & & \\ \langle -| & \frac{1}{2} (\delta + e^{-i\phi} \sin \theta (g_{\perp} \beta H)) & -\frac{1}{2} (g_{\parallel} \beta H \cos \theta) \end{array} \quad (21)$$

This Hamiltonian must be calculated for each  $\theta$  and  $\phi$  to obtain the field-dependent wave function coefficients ( $|A-\rangle = C_1|+2\rangle + C_2|-\rangle$ ) and energy splittings ( $\Delta E = E_{A+} - E_{A-}$ ) of the ground state doublet. These are then inserted into the general expressions for MCD intensity [186] to give Eq. (22), which has two parts: the first term describes  $xy$ -polarized ( $M_{xy}$ ) electric dipole transitions and the second term allows for non-zero  $z$ -polarization ( $M_z$ ).

$$\begin{aligned} \Delta \varepsilon = A_{\text{satlim}} \left\{ \int_0^{\pi/2} (|C_2|^2 - |C_1|^2) \cos \theta \sin \theta \tanh \left( \frac{\Delta E}{2kT} \right) d\theta \right. \\ \left. - 2\sqrt{2} \left( \frac{M_z}{M_{xy}} \right) \int_0^{\pi/2} (\text{Im}(C_1^* C_2)) \sin^2 \theta \tanh \left( \frac{\Delta E}{2kT} \right) d\theta \right\} \end{aligned} \quad (22)$$

Experimental data can be fit to Eqs. (21) and (22) by floating  $A_{\text{satlim}}$ ,  $\delta$  and  $g_{\parallel}$ , plus the two additional variables  $g_{\perp}$  and  $M_z/M_{xy}$ , and evaluating the MCD intensity expression numerically by averaging over  $\theta$  with a point-by-point summation on a

longitude. Because fitting MCD data to the full  $xy$ - and  $z$ -polarized intensity expression increases the number of floated parameters and softens the fits, a stronger fit can be obtained by fixing  $g_{\perp}$  and treating  $M_z/M_{xy}$  as a floating variable. Based on calculations from a  $^5T_{2g}$  Hamiltonian (see Section 3.4), a reasonable value for  $g_{\perp}$  is  $\sim 1$ . Because  $g_{\perp}$  is coupled to  $g_{\parallel}$  and in turn  $g_{\parallel}$  is coupled to  $\delta$ , the results from a  $^5T_{2g}$  Hamiltonian analysis (vide infra) were used to obtain the simulation parameters for a set of calculations to explore the effects of varying amounts of  $z$ -polarization in the MCD data. The parameters used to generate the plots shown in Fig. 21 are:  $g_{\perp}=0.0$ ,  $g_{\parallel}=9.0$ , and  $\delta=5.0\text{ cm}^{-1}$  for  $M_z/M_{xy}=0.0$  and  $g_{\perp}=1.0$ ,  $g_{\parallel}=8.8$ , and  $\delta=5.0\text{ cm}^{-1}$  for  $M_z/M_{xy}=-1.0$  or  $+1.0$ .

The data in Fig. 21, top, which include no  $z$ -polarization, show the non-Kramers doublet nesting behavior described in Section 3.3.3.1. Fig. 21, middle, shows the  $\beta H/2kT$  and  $1/kT$  plots for a non-Kramers doublet with a  $z$ -polarization having the opposite sign from the  $xy$ -polarization ( $M_z/M_{xy}=-1.0$ ). The  $\beta H/2kT$  plot for this simulation still exhibits nesting behavior, but additionally there appears to be some fanning. At the saturation limit, the  $1/kT$  plot predominantly reflects the  $\delta$  effect of decreasing intensity intervals for equal field increments; however, at the higher fields, this behavior is no longer observed. While this might arise from the contribution of a linear  $\mathcal{B}$ -term to the non-Kramers doublet (see Section 3.3.1.3), the  $z$ -polarized

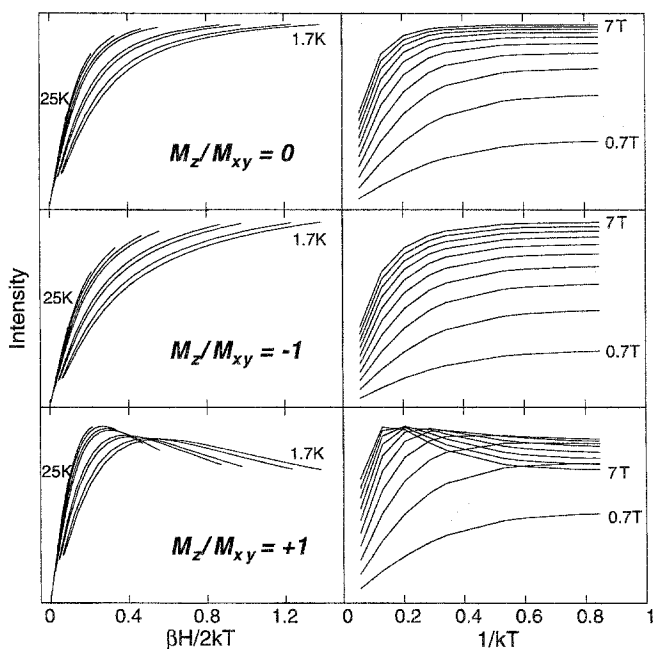


Fig. 21. Effects of  $z$ -polarization on a non-Kramers doublet. Simulated MCD intensities for an isolated non-Kramers doublet with  $A_{\text{satlim}}=100.0$  and  $\delta=5.0\text{ cm}^{-1}$  and the following parameters:  $g_{\parallel}=9.0$  and  $g_{\perp}=0.0$  for  $M_z/M_{xy}=0.0$  (top),  $g_{\parallel}=8.8$  and  $g_{\perp}=1.0$  for  $M_z/M_{xy}=-1.0$  (middle) or  $+1.0$  (bottom). A negative  $M_z/M_{xy}$  ratio causes a small change in the saturation behavior, particularly in the low-temperature, high-field region, and a positive  $M_z/M_{xy}$  ratio produces distinctive curve-crossings.

MCD behavior can be distinguished from a linear  $\mathcal{B}$ -term by fitting the data with an xy-polarized intensity expression which includes  $\mathcal{B}$ -terms (vide infra): a fit to data from a transition which contains z-polarization gives a  $g_{\parallel}$  value which is out of the acceptable range (see Section 3.4) and a very small  $B_0$ , while a fit to data from a transition with a  $\mathcal{B}$ -term yields reasonable values of  $g_{\parallel}$  and  $B_0$ . When both transition dipole moments have the same sign, such as  $M_z/M_{xy} = +1.0$  in Fig. 21, bottom, the saturation magnetization data produced are clearly different from any behavior previously observed. Thus a positive non-zero  $M_z/M_{xy}$  value should be easily identified from the qualitative shape of the saturation curves.

**3.3.3.3. Linear, temperature-independent  $\mathcal{B}$ -term effects** A linear  $\mathcal{B}$ -term is included in the MCD intensity expression by adding the term  $B_0 H$  [173] to either Eq. (20) or Eq. (22), depending on the polarization, where  $B_0$  indicates the magnitude of the ground-state linear  $\mathcal{B}$ -term and  $H$  is the magnetic field. Fig. 22 shows the  $\beta H/2kT$  and  $1/kT$  plots for an isolated non-Kramers doublet with a  $\mathcal{B}$ -term = 0.0 or +5.0% of  $A_{\text{satlim}}$ ,  $g_{\parallel} = 8.0$ ,  $\delta = 5.0 \text{ cm}^{-1}$ , and no z-polarization. The plots in Fig. 22, top, which contain no  $\mathcal{B}$ -term, show the same non-Kramers nesting behavior explored in Section 3.3.3.1. When a large linear  $\mathcal{B}$ -term is present (Fig. 22, bottom), the  $\beta H/2kT$  plot shows that the  $\mathcal{B}$ -term fanning observed for the effective Kramers doublet (Fig. 17) adds to the nesting behavior due to the non-zero  $\delta$ . The low-temperature region of the corresponding  $1/kT$  plot (Fig. 22, bottom right) shows that the intensity increment between equivalent fields does decrease at the saturation limit, as is expected for a non-zero  $\delta$ ; however, this increment converges to a fixed value proportional to the magnitude of the linear  $\mathcal{B}$ -term. Thus the presence of a

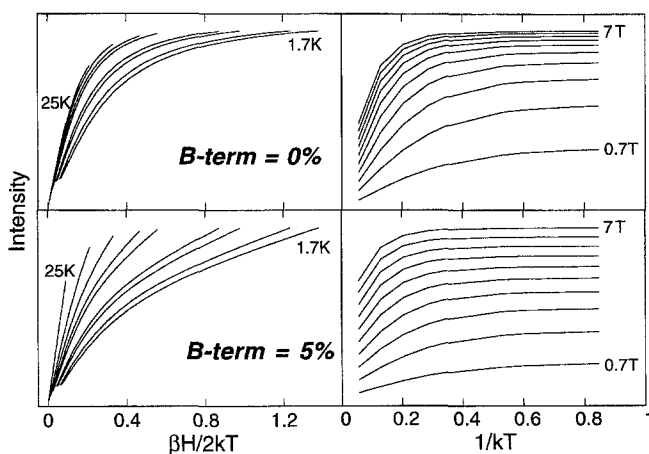


Fig. 22. Effects of a linear, temperature-independent  $\mathcal{B}$ -term on a non-Kramers doublet. Simulated MCD intensities for an isolated non-Kramers doublet with  $A_{\text{satlim}} = 100.0$ ,  $\delta = 5.0 \text{ cm}^{-1}$ ,  $g_{\parallel} = 8.0$ , and  $\mathcal{B}$ -term (as a percentage of  $A_{\text{satlim}}$ ) = 0.0% (top) and +5.0% (bottom), assuming pure xy-polarization. Inclusion of a linear  $\mathcal{B}$ -term combines fanning behavior with the non-Kramers nesting behavior in the  $\beta H/2kT$  plot (bottom left) and causes the low-temperature, high-field region of the  $1/kT$  plot (bottom right) to converge to an equal intensity spacing.

linear  $\mathcal{B}$ -term, positive or negative, on a non-Kramers doublet can be recognized primarily by the behavior of the intensity curves at lowest temperature in a  $1/kT$  plot which converge to a set of evenly spaced saturation curves.

**3.3.3.4. Population of excited states** Lastly, we consider the possibility of populating low-lying excited states for a non-Kramers doublet. The  $xy$ -polarized MCD intensity expression which allows for the summing over non-Kramers excited states, including linear  $\mathcal{B}$ -terms for all states, is given in Eq. (23).

$$\Delta\epsilon = \sum_i \left\{ (A_{\text{satlim}})_i \int_0^{\pi/2} \frac{\cos^2\theta \sin\theta}{\Gamma_i} (g_{\parallel i} \beta H) \alpha_i d\theta + B_i H \gamma_i \right\} \quad (23)$$

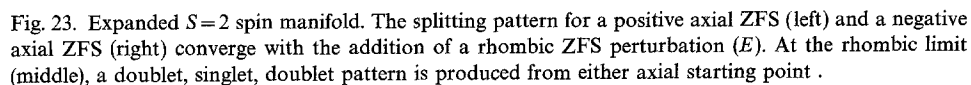
where

$$\begin{aligned} \Gamma_i &= \sqrt{\delta_i^2 + (g_{\parallel i} \beta H \cos\theta)^2} \\ \alpha_i &= \frac{e^{-(E_i - \Gamma_i/2)/kT} - e^{-(E_i + \Gamma_i/2)/kT}}{\sum_j e^{-(E_j - \Gamma_j/2)/kT} + e^{-(E_j + \Gamma_j/2)/kT}} \\ \gamma_i &= \frac{e^{-(E_i - \delta_i/2)/kT} + e^{-(E_i + \delta_i/2)/kT}}{\sum_j e^{-(E_j - \delta_j/2)/kT} + e^{-(E_j + \delta_j/2)/kT}} \end{aligned}$$

$(A_{\text{satlim}})_i$ ,  $\delta_i$ ,  $g_{\parallel i}$ , and  $B_i$  are the  $\mathcal{C}$ -term intensity factor, the rhombic ZFS of a non-Kramers doublet, the  $g_{\parallel}$ , and the linear  $\mathcal{B}$ -term of the  $i$ th doublet, respectively.  $E_i$  is defined as the energy of the  $i$ th state above the ground state ( $E_0 \equiv 0.0$ ). Boltzmann population over all states has been included for both the  $\mathcal{C}$ -term intensity, with the factor  $\alpha_i$ , and the linear  $\mathcal{B}$ -term intensity, with the factor  $\gamma_i$ . Note that  $\alpha_i$  and  $\gamma_i$  are different because the largest contribution to the  $\mathcal{B}$ -terms should derive from  $H \perp z$  as governed by  $g_{\perp}$  which is small and thus the energy splitting is governed by  $\delta$ .

The effects of populating excited states for a non-Kramers doublet will be most apparent when the experimental data are collected at high temperatures, otherwise the additional factors contributing to non-superimposable saturation magnetization behavior ( $\delta$  and linear  $\mathcal{B}$ -terms) may be too difficult to unambiguously deconvolute. As excited states begin to be populated, the experimental data will effectively break into two regions: a lower-temperature region which can be fit by one set of ground-state parameters and a higher-temperature region which will not fit with those ground-state parameters. If the addition of  $z$ -polarization still does not satisfactorily fit all of the data, then the inclusion of one or more excited states in the fit will be necessary to describe the observed saturation magnetization behavior.

Considering all of these effects on the saturation magnetization behavior of a non-Kramers doublet, the FeSOD VTVH data presented in Fig. 7(d,e) do not indicate the presence of a significant linear  $\mathcal{B}$ -term or low-lying populated excited states, nor does the inclusion of  $z$ -polarization improve the fit to the experimental data. The FeSOD data can therefore be fit to Eq. (20) for a purely  $xy$ -polarized transition to



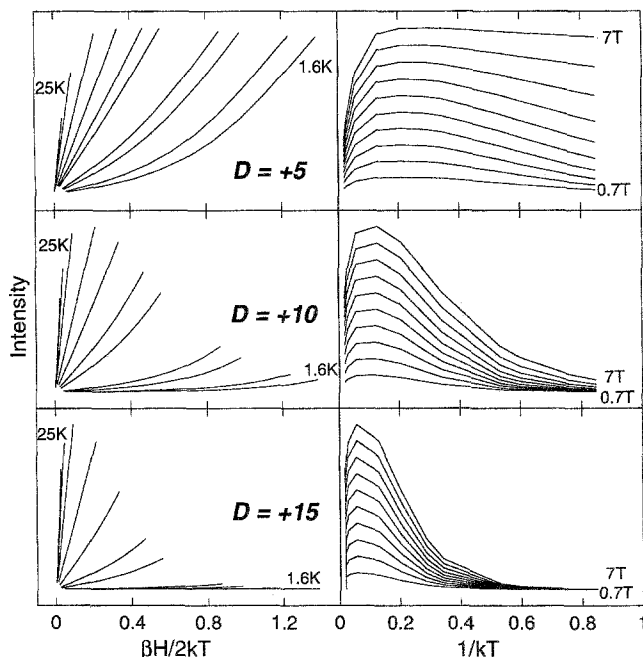


Fig. 24. Effects of excited-state population on a  $+D$  effective Kramers  $S=2$  spin manifold with pure  $xy$ -polarization. Simulated MCD intensities calculated with  $g_{\parallel}(0)=0.0$ ,  $g_{\parallel}(\pm 1)=4.0$ ,  $g_{\parallel}(\pm 2)=8.0$ , and  $A_{\text{satlim}}(0)=0.0$ ,  $A_{\text{satlim}}(\pm 1)=50.0$ , and  $A_{\text{satlim}}(\pm 2)=100.0$ . The excited states were positioned at  $E(\pm 1)=D \text{ cm}^{-1}$  and  $E(\pm 2)=4D \text{ cm}^{-1}$  above the ground state, for  $D=+5.0 \text{ cm}^{-1}$  (top),  $+10.0 \text{ cm}^{-1}$  (middle), and  $+15.0 \text{ cm}^{-1}$  (bottom). No  $z$ -polarization or linear  $\mathcal{B}$ -term effects were included. The upwards-curving behavior in the  $\beta H/2kT$  plots (left) and the diminished MCD intensity in the low-temperature, low-field region of the  $1/kT$  plots (right) are unlike the  $D<0$  behavior.

magnetization isotherms that are clearly distinct from the effective Kramers doublet model presented in Fig. 18. The  $1/kT$  plots are especially revealing at fields where the Zeeman splitting is much smaller than  $D$ . For example, the 0.7 T curves in Fig. 24, right, show that there is no MCD intensity at low temperature. As the temperature is increased and the  $M_S=\pm 1$  level is populated, the MCD intensity increases proportionally to both the Boltzmann population and the magnitude of  $A_{\text{satlim}}(\pm 1)$ . If the Zeeman splitting is large relative to  $D$ , components of the  $M_S=\pm 1$  and  $\pm 2$  doublets can approach and even cross the lowest level, resulting in substantially increased MCD intensity even at pumped helium temperatures. This can be seen for the  $D=+5.0 \text{ cm}^{-1}$ , 7 T curve in Fig. 24, top right, where MCD intensity is substantial over the entire 1.7–25 K range. Note that the calculated behavior in Fig. 24 based on the  $S=2$  spin manifold with an  $M_S=0$  level lowest and  $xy$ -polarized  $d \rightarrow d$  transitions does not produce a result resembling the FeSOD saturation magnetization data, nor, in fact, do the results resemble the existing VTVH MCD data for any non-heme ferrous monomer.

**3.3.4.2. *z*-Polarization effects in the axial limit** The above  $+D$  analysis was restricted to a Zeeman effect produced by an applied magnetic field along the molecular  $z$ -axis. The Zeeman effect resulting from field along the molecular  $x$  and  $y$  directions will now be included as a source of MCD intensity. Note from Eq. (14) that this requires non-zero values of  $M_x M_z$  and  $M_y M_z$ , i.e.,  $z$ -polarization. The importance of the off- $z$ -axis Zeeman effect for  $S=2$  systems is illustrated in the upper half of Fig. 25, which shows the energy levels of the  $S=2$  ground state for  $D=+10.0\text{ cm}^{-1}$  and  $E/D=0.0$  (axial limit) responding to an applied magnetic field in the molecular  $x$ ,  $y$  and  $z$  directions. Fig. 25(a) shows the Zeeman effect for  $H\parallel z$  and corresponds to the scheme used above to calculate the  $xy$ -polarized MCD intensity. Fig. 25(b) for  $H\parallel x,y$  shows that the  $M_S=0$  level undergoes a field-induced mixing with one combination of  $M_S=\pm 1$  sublevels. The other combination of the  $M_S=\pm 1$  doublet and the  $M_S=\pm 2$  doublet do not exhibit a significant off-axis Zeeman effect for fields up to 7 T with  $D=10.0\text{ cm}^{-1}$ . This mixing of the  $M_S=0$  with the  $M_S=\pm 1$  levels can lead to an intense  $\mathcal{B}$ -term because the energy difference between these levels,  $D$ , is small, corresponding to the example depicted in Fig. 10(c). Both the  $M_S=0$  ground and  $M_S=\pm 1$  intermediate sublevels will contribute MCD intensity, but with opposite signs and weighted by their Boltzmann populations.

A related type of temperature-dependent  $\mathcal{B}$ -term was considered by Collingwood et al. [179]. They used Eq. (24) to describe the two-level system consisting of the

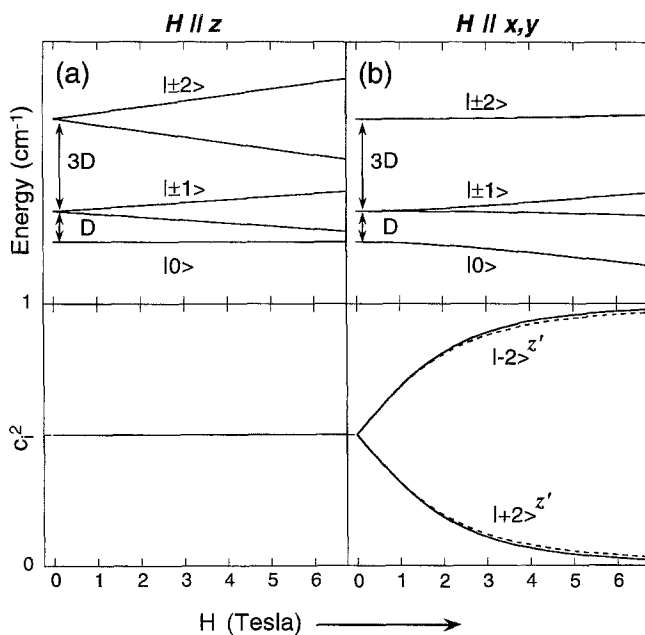


Fig. 25. Response of an axial,  $S=2$ ,  $+D$  spin system to a magnetic field along the molecular  $x$ ,  $y$  and  $z$  directions. The energy levels (top) and the normalized  $|\pm 2\rangle^{z'}$  components of the  $|0\rangle^z$  wave function,  $c_i^2$ , (bottom) are plotted as a function of the magnetic field for (a)  $H\parallel z$  and (b)  $H\parallel x,y$  (the dashed lines indicate the  $|+\rangle$  and  $|-\rangle$  components of a non-Kramers doublet ( $-D$ )).



non-degenerate levels  $|A\rangle$  and  $|K\rangle$  which have a Zeeman interaction for  $H\parallel z$  and only  $xy$ -polarized electric dipole transitions.

$$\mathcal{B} = \frac{3}{|d_A|} \langle K|\mu_z|A\rangle (\langle A|m_+|J\rangle \langle J|m_-|K\rangle - \langle A|m_-|J\rangle \langle J|m_+|K\rangle) \tanh\left(\frac{\Delta E_{KA}}{2kT}\right) \quad (24)$$

In Eq. (24), the first term is the Zeeman matrix element between  $|A\rangle$  and  $|K\rangle$ ;  $m_{\pm}$  are the  $xy$ -polarized electric dipole transition moments (Eq. (9)) from the ground-state sublevels to the excited state  $|J\rangle$ ; and  $\Delta E_{KA}$  is the zero-field splitting. Eq. (24) is very similar to Eq. (17) for a  $\mathcal{C}$ -term, and in fact Collingwood et al. show that the saturation behavior of a temperature-dependent  $\mathcal{B}$ -term is identical to that for a  $\mathcal{C}$ -term except that  $\Delta E$  is substituted for the Zeeman splitting,  $g\beta H$ . Although Collingwood et al. do not fit experimental VTVH MCD data, Hamilton et al. [191] applied Eq. (25) to VTVH MCD data from an  $S=1$  system to establish the magnitude of the positive ZFS.

$$\Delta\varepsilon = A_{\text{satlim}} \tanh\left(\frac{\Delta E}{2kT}\right) \quad (25)$$

Application of Eq. (25) resulted in linear, nested  $\beta H/2kT$  curves that approximated, but did not completely reproduce the curvature of the data at high fields. While not explicitly stated [191], the Zeeman interaction for the  $S=1$  case is for  $H\perp z$ .

In order to evaluate the importance of the temperature-dependent  $\mathcal{B}$ -term contribution to MCD intensity in ferrous systems, it is helpful to consider the Zeeman effect for  $H\parallel x$  in more detail. Eq. (26) relates the  $\tilde{\mathbf{D}}$  tensor to the ZFS parameters,  $D$  and  $E$  [123].

$$\tilde{\mathbf{D}} = \begin{pmatrix} D_x & 0 & 0 \\ 0 & D_y & 0 \\ 0 & 0 & D_z \end{pmatrix} = \begin{pmatrix} -D/3 + E & 0 & 0 \\ 0 & -D/3 - E & 0 \\ 0 & 0 & 2D/3 \end{pmatrix} \quad (26)$$

The spin Hamiltonian expression given in Eq. (1) can then be rewritten in terms of the diagonal components of the tensor  $\tilde{\mathbf{D}}$  to give Eq. (27).

$$\mathcal{H} = D_x \hat{S}_x^2 + D_y \hat{S}_y^2 + D_z \hat{S}_z^2 + \beta(g_x H_x \hat{S}_x + g_y H_y \hat{S}_y + g_z H_z \hat{S}_z) \quad (27)$$

This form of the spin Hamiltonian presumes that both the  $\tilde{\mathbf{D}}$  and  $\tilde{\mathbf{g}}$  tensors are quantized along the molecular  $z$ -axis and that the eigenvectors have the usual spin labels of  $M_S=0, \pm 1$ , and  $\pm 2$ . Requantizing the  $\tilde{\mathbf{D}}$  tensor along the molecular  $x$ -axis is achieved by mapping  $D_x$ ,  $D_y$  and  $D_z$  into  $D_z$ ,  $D_x$  and  $D_y$ , respectively, and relabeling the new axes  $x'$ ,  $y'$  and  $z'$ , so that  $x$  in the original coordinate system is now  $z'$ . This transformation results in new spin labels for the zero-field wave functions, given in Eq. (28), where the superscript  $z$  refers to the  $z$ -quantized  $\tilde{\mathbf{D}}$  tensor and  $z'$

to the  $x$ -quantized  $\tilde{\mathbf{D}}$  tensor.

$$\begin{aligned}
 |0\rangle^z &\rightarrow +\sqrt{\frac{3}{8}}|+2\rangle^{z'} + \sqrt{\frac{3}{8}}|-2\rangle^{z'} - \sqrt{\frac{1}{4}}|0\rangle^{z'} \\
 |-1\rangle^z &\rightarrow +\sqrt{\frac{1}{2}}|+1\rangle^{z'} - \sqrt{\frac{1}{2}}|-1\rangle^{z'} \\
 |+1\rangle^z &\rightarrow -\sqrt{\frac{1}{2}}|+2\rangle^{z'} + \sqrt{\frac{1}{2}}|-2\rangle^{z'} \\
 |-2\rangle^z &\rightarrow +\sqrt{\frac{1}{2}}|+1\rangle^{z'} + \sqrt{\frac{1}{2}}|-1\rangle^{z'} \\
 |+2\rangle^z &\rightarrow +\sqrt{\frac{1}{8}}|+2\rangle^{z'} + \sqrt{\frac{1}{8}}|-2\rangle^{z'} - \sqrt{\frac{3}{4}}|0\rangle^{z'}
 \end{aligned} \tag{28}$$

A magnetic field along  $x$  ( $=z'$ ) results in the diagram shown in Fig. 25(b). From both the figure and Eq. (28) it is clear that the  $M_S=0$  and one partner of the  $M_S=\pm 1$  sublevels behave very similarly to an  $M_S=\pm 2$  non-Kramers doublet where  $g(\text{effective})=8.0$  and  $\delta=D$ . This is also illustrated in Fig. 25(b), bottom, where the coefficients ( $c_i^2$ ) of the  $|\pm 2\rangle^{z'}$  components of  $|0\rangle^z$  (solid lines) are compared to those of an  $M_S=\pm 2$  pure non-Kramers doublet (dashed lines). Thus, the first three levels of an  $S=2$  axial  $+D$  system with magnetic field along the molecular  $x$ -axis can be modeled by a non-Kramers doublet with a zero-field splitting of  $D$  and an effective  $g$ -value of 8.0, but with an additional MCD-silent third level at  $D \text{ cm}^{-1}$ . The VTVH data presented in Fig. 20, left, show that increasing the zero-field splitting of a non-Kramers doublet delays the onset of the field-induced saturation of the MCD intensity. In fact, if  $+D$  is greater than  $10 \text{ cm}^{-1}$ , the MCD intensity will appear predominantly linear with field and can be crudely modeled by Eq. (25).

VTVH MCD data have been calculated using the three-level  $+D$  model for  $D=+10.0 \text{ cm}^{-1}$  and  $g(\text{effective})=8.0$ , shown in Fig. 26 (solid lines), and compared to the  $-D$  non-Kramers doublet model with the same ZFS of  $\delta=10.0 \text{ cm}^{-1}$  and  $g=8.0$ , shown in Fig. 26 (dashed lines). These data are identical for  $kT < D$ , but

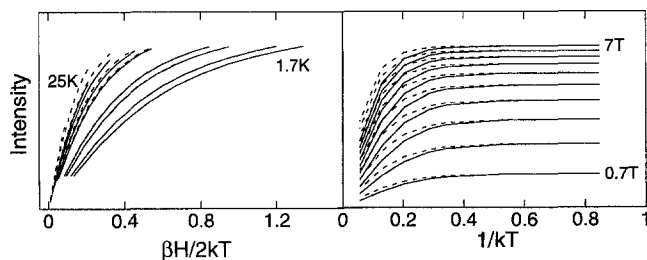


Fig. 26. Comparison of VTVH data from the three-level  $+D$  model versus the  $-D$  non-Kramers doublet model. Simulated saturation magnetization data using the three-level  $+D$  model with  $D=+10.0 \text{ cm}^{-1}$  (solid lines) and the  $-D$  non-Kramers doublet model with  $\delta=10.0 \text{ cm}^{-1}$  (dashed lines). The two models differ for  $kT$  of the order of or greater than  $\delta$ .

deviations occur when the third MCD-silent level becomes populated. Therefore, it is crucial to collect VTVH data at high temperatures relative to the magnitude of the ZFS to distinguish the sign of  $D$ . For example, if the lowest-temperature isotherm from the  $+D$  simulation in Fig. 26 is iteratively fit to a  $-D$  non-Kramers doublet model (Section 3.3.3.1), a  $g$ -value of 8 is obtained; however, if the entire  $+D$  data set in Fig. 26 for  $D = +10.0 \text{ cm}^{-1}$  is fit, the  $g$ -value obtained is 6.7, which is not physical for a  $D < 0$  ferrous center (see Section 3.4) and is indicative of a  $+D$  system.

**3.3.4.3. Rhombicity effects** The effects of non-zero  $E/D$  ratios are now considered, beginning at the axial  $+D$  limit ( $|E/D|=0$ ) and progressing to the rhombic limit ( $|E/D|=1/3$ ). Fig. 27 shows 12  $+D$  energy level diagrams in a grid: the columns from left to right are  $H \parallel x$ ,  $H \parallel y$ , and  $H \parallel z$  and the rows from top to bottom begin at the axial limit and extend to the rhombic limit. Proceeding down the first column ( $H \parallel x$ ), the  $M_S = \pm 1$  levels begin to split in Fig. 27(d) with a small non-zero value of  $E$ . With a larger rhombic ZFS (Fig. 27(g)), the  $M_S = \pm 1$  splitting is larger and the  $M_S = \pm 2$  levels start to split. At the rhombic limit (Fig. 27(j)), the ZFS pattern has become symmetric so that the splitting between the  $M_S = 0$  and the lower-energy

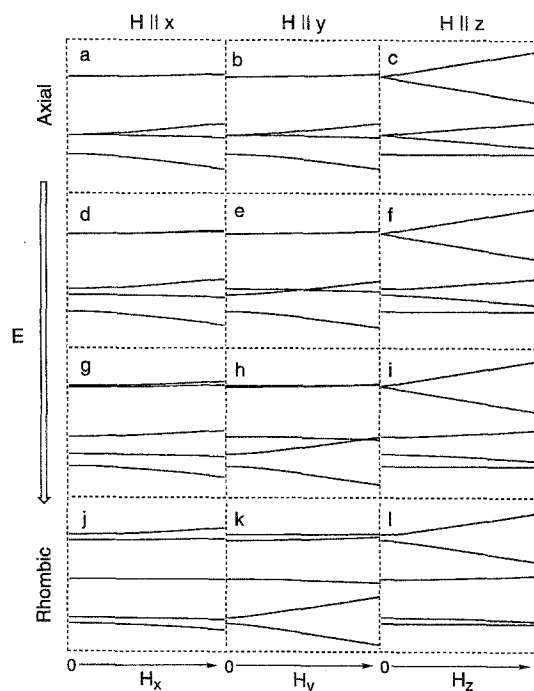


Fig. 27. Response of an  $S=2$ ,  $+D$  spin system to a magnetic field along the  $x$ ,  $y$  and  $z$  directions from the axial to the rhombic limits. The energies of the  $M_S = 0, \pm 1, \pm 2$  sublevels are plotted as a function of increasing magnetic field (0.0–7.0 T). Each column corresponds to an applied magnetic field along the molecular  $x$  (left),  $y$  (middle) and  $z$  (right) directions, and each row represents a different degree of rhombicity,  $E/D = 0.0$  (top), 0.05 (second row), 0.17 (third row), and 0.33 (bottom).

$M_S = \pm 1$  partner is identical to the  $M_S = \pm 2$  splitting. In the weak-axial (small rhombic) case (Fig. 27, second row), there is a strong Zeeman interaction between the first and third sublevels for  $H \parallel x$  (Fig. 27(d)). In Fig. 27(e), when  $H \parallel y$ , the strong Zeeman interaction is between first and second sublevels; and in Fig. 27(f), for  $H \parallel z$ , the strong Zeeman interaction is between the second and third ( $M_S = \pm 1$ ) sublevels. For a larger  $|E/D|$  ratio (Fig. 27, third row), the ZFS between the  $M_S = \pm 1$  levels has increased so that the splitting pattern of the lowest three levels resembles a low-energy doublet with a higher-energy singlet. Finally, at the rhombic limit (Fig. 27, bottom row), the splitting pattern of the five spin levels is identical to the  $-D$  spin Hamiltonian results, except that the strong Zeeman splitting occurs for  $H \parallel y$  (Fig. 27(k)) instead of  $H \parallel z$ .

According to Eq. (12), non-zero  $\mathcal{B}$ -term intensity requires that there be non-zero electric dipole moments along two molecular axes perpendicular to the magnetic field direction. Additionally, in the case of a temperature-dependent  $\mathcal{B}$ -term, the two participating sublevels  $|A\rangle$  and  $|K\rangle$  will have equal and opposite MCD intensity. However, as shown above, there is a third level which must also be included in the analysis of  $+D$  systems. Fig. 28 shows the three different MCD saturation magnetization behavior calculations for  $H \parallel x$ ,  $H \parallel y$ , and  $H \parallel z$  and for  $D = +10.0 \text{ cm}^{-1}$  and  $E/D = 0.2$ . From Eq. (12) for a randomly oriented sample, these curves will be

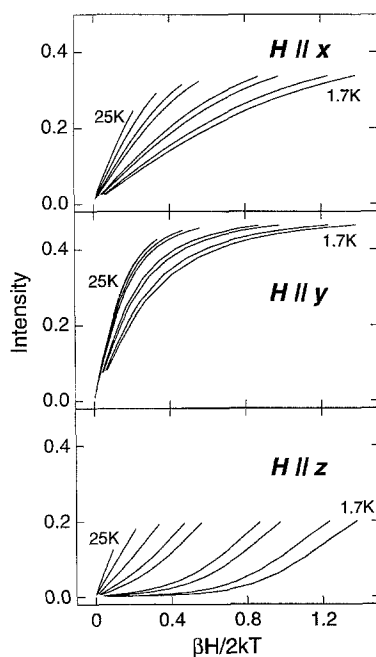


Fig. 28. VTVH behavior of a three-level  $+D$  model with  $H \parallel x$ ,  $y$  and  $z$ . Simulated MCD intensities using  $D = +10.0 \text{ cm}^{-1}$  and  $E/D = 0.2$  for  $H \parallel x$  (top),  $H \parallel y$  (middle), and  $H \parallel z$  (bottom). In a randomly oriented sample, the contributions of each of these will be weighted by the electric dipole moments  $M_x M_z$ ,  $M_y M_z$ , and  $M_x M_y$ , respectively.

weighted by the electric dipole moments  $M_y M_z$ ,  $M_x M_z$ , and  $M_x M_y$  and the magnitude of the Zeeman interaction. If all three polarizations contribute equally to the MCD intensity, the  $H\parallel y$  contribution will dominate and could be interpreted as a non-Kramers doublet with a large linear  $\mathcal{B}$ -term ( $B_0 > 5\%$  of  $A_{\text{satlim}}$ ), although the calculated  $g$ -value may be unphysical (see Section 3.4).

Distinguishing positive and negative  $D$  will not always be straightforward since the VTVH data for either sign of  $D$  can qualitatively appear very similar, as shown in Fig. 26. This is especially true if the signal-to-noise ratios of the experimental data limit the utility of a goodness-of-fit parameter. One indication that a system has a positive value of  $D$  is an experimentally measured  $\delta > 7 \text{ cm}^{-1}$ , which is out of the theoretical range of  $\delta$  (see Section 3.4). Additionally, the  $g$ -values for the  $-D$  case should be greater than 8.3 (Section 3.4), while the  $g$ -value for  $+D$  is 8.0 (both models assume molecular  $g$ -values of 2.00). A three-level  $+D$  fit can also be applied to the data and if the fit places the third level at high energy, then the isolated non-Kramers doublet model is indicated and the system is either  $-D$  or rhombic. In summary, a  $+D$  system must be described by a three-level model until the system is sufficiently rhombic to drive the third level out of the thermal range of the experiment, while the  $-D$  case can be treated as a non-Kramers doublet as presented in Section 3.3.3. Thus, any ambiguity in the sign of  $D$  for non-heme ferrous centers can in general be resolved.

### 3.4. Ligand field origin of spin Hamiltonian parameters

The ground-state spin Hamiltonian parameters discussed above can be used to obtain an experimentally-derived energy level diagram for the low-lying d-orbitals, which can be compared with the ligand field calculations from Section 3.2. Since  $\text{Fe}^{2+}$  in protein environments can have a variety of geometries, a series of different cases must be considered. A list of relevant iron coordination numbers with appropriate limiting axial geometric distortions as well as the associated sign of  $D$  is summarized in Table 4.

#### 3.4.1. Six-coordinate geometry

As demonstrated in Section 3.2, the d-orbitals of a six-coordinate  $\text{Fe}^{2+}$  center are split under an octahedral crystal field into a doubly degenerate  $^5\text{E}_g$  excited state and a triply degenerate  $^5\text{T}_{2g}$  ground state. A treatment of pure octahedral symmetry is not necessary, however, since ferrous sites in proteins are largely distorted and Jahn-Teller effects are expected to lower the symmetry of octahedral model complexes. Under a tetragonal axial distortion, both the  $^5\text{E}_g$  and  $^5\text{T}_{2g}$  states are split in energy as depicted in Fig. 29, where the splitting of the excited state,  $\Delta^5\text{E}_g$ , can be determined experimentally (see Table 2). As shown below, the sign of the splitting of the  $^5\text{T}_{2g}$  state,  $\Delta \equiv E_{xz,yz} - E_{xy}$ , determines the sign of the spin Hamiltonian parameter  $D$ : for a positive  $\Delta$ , the non-degenerate  $^5\text{B}_{2g}$  state is the ground state which leads to a positive  $D$ , while for a negative  $\Delta$ , the doubly degenerate  $^5\text{E}_g$  state is lowest and  $D$  is negative. The degeneracy of the  $^5\text{E}_g$  ground state is further removed by a rhombic distortion so that the  $d_{xz}$  and  $d_{yz}$  partners split by the amount  $V$ . The two possible

Table 4

Different  $\text{Fe}^{2+}$  coordination environments relevant to non-heme ferrous enzymes

C.N.	Parent symmetry	Distortion	Orbital ground state	Sign of $D$	Treated by case
6	octahedral	tetragonal or trigonal	singlet ( ${}^5\text{B}_{2g}/{}^5\text{A}_1'$ )	$+D$	3.4.1.1
			doublet ( ${}^5\text{E}_g$ )	$-D$	3.4.1.2
5	square	strong-axial	singlet ( ${}^5\text{B}_{2g}$ )	$+D$	(3.4.1.1)
	pyramidal	weak-axial	doublet ( ${}^5\text{E}_g$ )	$-D$	(3.4.1.2)
	trigonal	–	doublet ( ${}^5\text{E}_g$ )	$-D$	3.4.2.2
	bipyramidal	–	–	–	–
4	tetrahedral	tetragonal (flattened)	singlet ( $\text{d}_{x^2}$ )	$+D$	3.4.3.1
		tetragonal (elongated)	singlet ( $\text{d}_{x^2-y^2}$ )	$-D$	3.4.3.2
	square planar	–	singlet ( $\text{d}_{z^2}$ )	$+D$	(3.4.3.1)
		–	–	–	–

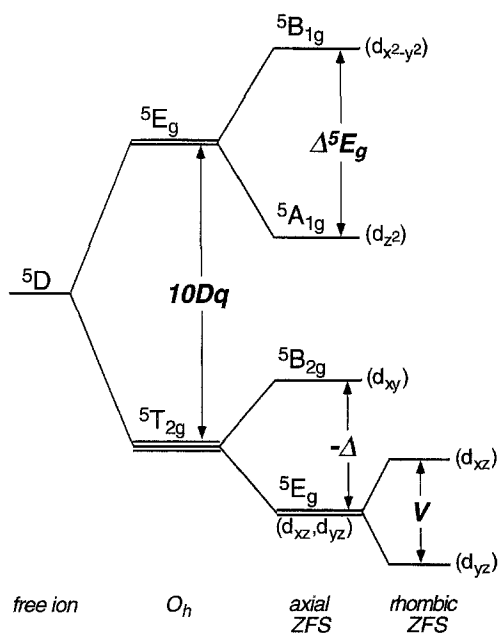


Fig. 29. Splitting pattern of the d-orbitals under distorted octahedral symmetry. The  $\text{d}^6$  free ion parent state,  ${}^5\text{D}$ , is split under an octahedral ligand field into the  ${}^5\text{T}_{2g}$  and  ${}^5\text{E}_g$  states, which are separated by the energy  $10Dq$ . A tetragonal axial distortion splits the  ${}^5\text{E}_g$  excited state by the amount  $\Delta^5\text{E}_g$  and the  ${}^5\text{T}_{2g}$  ground state by the amount  $\Delta$ . When  $\Delta$  is negative, the ground state becomes  ${}^5\text{E}_g$ , whose orbital degeneracy is removed by a rhombic distortion ( $V$ ).

ground states for axially distorted octahedral symmetry,  ${}^5B_{2g}$  or  ${}^5E_g$ , are obtained through either tetragonal or trigonal distortions (see Section 3.2).

**3.4.1.1. Distorted octahedral,  ${}^5B_{2g}$  or  ${}^5A_1'$  ground state** We first consider the  $+D$  distorted octahedral case, where  $\Delta$  in Fig. 29 is positive to give an orbitally non-degenerate ground state. This corresponds to an axial tetragonal compression to give the  $d_{xy}$  orbital lowest in energy ( ${}^5B_{2g}$  ground state) or to a trigonal compression which gives the  $d_{z^2}$  orbital lowest ( ${}^5A_1'$  ground state) (see Section 3.2). Because the  ${}^5B_{2g}$  state has five-fold spin degeneracy but no orbital degeneracy, the  $S=2$  spin Hamiltonian in Eq. (2) is applied to obtain the splittings of the  ${}^5B_{2g}$  sublevels (see Fig. 6). The magnitude of  $D$  can be estimated from perturbation theory through second-order spin-orbit coupling with the  ${}^5E_g$  partner of the  ${}^5T_{2g}$  ground state which gives Eq. (29).

$$D = \frac{\lambda^2}{\Delta} \quad (29)$$

The spin-orbit coupling parameter  $\lambda$  is related to the one-electron spin-orbit coupling parameter  $\zeta$  by  $\lambda = -\zeta/2S$ , where  $\zeta(\text{Fe}^{2+}) = -400 \text{ cm}^{-1}$  [192]. In coordination complexes, the free-ion value of  $\lambda(\text{Fe}^{2+}) = -100 \text{ cm}^{-1}$  is reduced to approximately  $-80 \text{ cm}^{-1}$  due to covalency. The stronger the axial compression, i.e., the larger the value of  $\Delta$ , the smaller the value of  $D$ . Fig. 30(a) shows  $\lambda^2/\Delta$  (dashed lines) plotted as a function of  $+D$ , using varying values of  $\lambda$  to account for small variations in covalency.

Although the  ${}^5B_{2g}$  level has no in-state orbital angular momentum, this state is derived from the parent  ${}^5T_{2g}$  state which does contain orbital angular momentum. A more complete treatment of the  ${}^5B_{2g}$  state includes spin-orbit coupling effects with the  ${}^5E_g$  state in a full  ${}^5T_{2g}$  Hamiltonian (see Section 3.4.1.2). This treatment gives a more accurate plot of  $+D$  versus  $+\Delta$ , as shown in Fig. 30(a) (solid lines), where again a range of  $\lambda$  values have been used. Although the spin Hamiltonian approximation for the  ${}^5B_{2g}$  state holds for most values of  $+\Delta$ , Fig. 30(a) demonstrates that the full  ${}^5T_{2g}$  Hamiltonian should be used for  $+\Delta < \sim 600 \text{ cm}^{-1}$ . This method also provides a range for the magnitude of  $+D$  between  $\sim 2$  and  $15 \text{ cm}^{-1}$ ; the identical treatment for negative  $D$  gives a range of  $-D$  values between approximately  $-3$  and  $-23 \text{ cm}^{-1}$ . The value of  $|E|$  depends on both the axial ( $+\Delta$ ) and rhombic ( $V$ ) ZFS parameters. Fig. 30(b) illustrates this relation by plotting  $|E|$  as a function of  $|V|/2\Delta$  for a range of  $+\Delta$  values. Thus the ground-state parameters  $D$  and  $E$ , obtained through an analysis of the VTVH MCD data as described in Section 3.3.4, can be used to determine the values of  $+\Delta$  (using Fig. 30(a)) and  $|V|$  (using Fig. 30(b)) which together provide  $t_{2g}$  orbital splittings as shown in Fig. 29.

**3.4.1.2. Distorted octahedral,  ${}^5E_g$  ground state** When  $D$  is negative, the  ${}^5T_{2g}$  ground state splits by  $-\Delta$  and the  ${}^5E_g$  component is lowest for either a tetragonally (Fig. 29) or a trigonally elongated octahedron. Unlike the  ${}^5B_{2g}$  state, the  ${}^5E_g$  state retains the in-state orbital angular momentum of the parent  ${}^5T_{2g}$  state and therefore requires

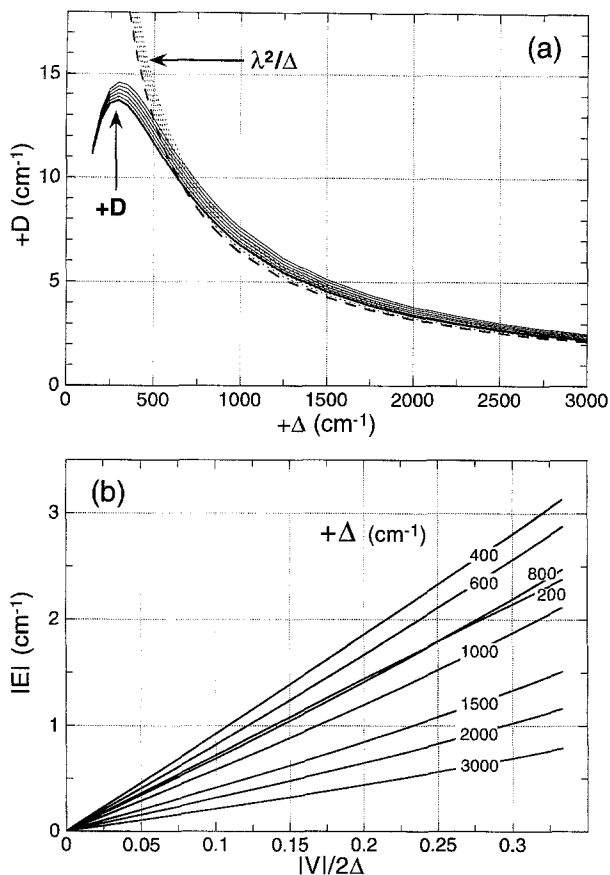


Fig. 30. Relation between the ZFS parameters  $+D$  and  $E$  to the ligand field parameters  $+Δ$  and  $V$ . (a)  $+D$ , plotted as a function of  $+Δ$ , as calculated from perturbation theory ( $+D = \lambda^2/\Delta$ , dashed) and from the full  ${}^5T_{2g}$  Hamiltonian (solid) using  $\lambda = -80 \text{ cm}^{-1}$  (heavy line) to  $-85 \text{ cm}^{-1}$  (light lines) to account for small variations in covalency. (b)  $|E|$  as a function of  $|V|/2\Delta$  calculated from the  ${}^5T_{2g}$  Hamiltonian for a range of  $+Δ$  values and  $\lambda = -80 \text{ cm}^{-1}$ .

coupling of the spin and orbital angular momenta. A full Hamiltonian which includes spin-orbit coupling over all components of the  ${}^5T_{2g}$  ground state is given by Eq. (30), using the operator equivalence method [193] for the axial and rhombic ZFS distortions in terms of the parameters  $\Delta$  and  $V$ .

$$\begin{aligned} \mathcal{H}({}^5T_{2g}) = & \lambda(\vec{L} \cdot \vec{S}) + \Delta \left\{ \hat{L}_z^2 - \frac{1}{3} L(L+1) \right\} + V(\hat{L}_x^2 - \hat{L}_y^2) \\ & + \beta \{ (\hat{L}_x + 2\hat{S}_x)H_x + (\hat{L}_y + 2\hat{S}_y)H_y + (\hat{L}_z + 2\hat{S}_z)H_z \} \end{aligned} \quad (30)$$

$\hat{L}$  operates with an effective orbital angular momentum of  $L' = -1$  which is appropriate for a  $T_{2g}$  state [193]. Zeeman perturbations are included in the last term of Eq. (30), where  $\beta$  is the Bohr magneton and  $H_i$  is the magnetic field in the  $i$  direction.



Higher-order spin-orbit coupling terms have not been included as they were not found to improve calculations of  ${}^5T_{2g}$  ground-state data for iron complexes [127]. Spin-spin interactions have been excluded since the spin-spin coupling parameter  $\rho$  is very small for  $\text{Fe}^{2+}$ ,  $\rho(\text{Fe}^{2+}) = 0.2 \text{ cm}^{-1}$  [123]. Similarly, Jahn-Teller effects have been ignored as the Jahn-Teller interaction is weak for the systems considered here and the Ham reduction factor is only  $\sim 0.9$  [127].

Eq. (30) is applied to the 15 basis functions formed by coupling  $M_s = \pm 2, \pm 1, 0$  and  $M_{L'} = +1, 0, -1$ , where the  $t_{2g}$  real d-orbitals are written as linear combinations of the  $M_{L'}$  complex wave functions:  $|+1\rangle = (d_{xz} - d_{yz})/\sqrt{2}$ ,  $|-1\rangle = (d_{xz} + d_{yz})/\sqrt{2}$  and  $|0\rangle = d_{xy}$ . The 15 energy levels obtained from the solution of this Hamiltonian are plotted in Fig. 31(a) for a range of  $-\Delta$  values and  $|V/2\Delta|$  values. Under pure octahedral symmetry, i.e., both  $\Delta$  and  $V$  are zero, the 15 sublevels split into 3-fold, 5-fold, and 7-fold degenerate states, separated by  $2\lambda$  and  $3\lambda$  respectively, as would be expected for a simple  $J' = |L + S| \dots |L - S|$  treatment. Note the inverted Hund's

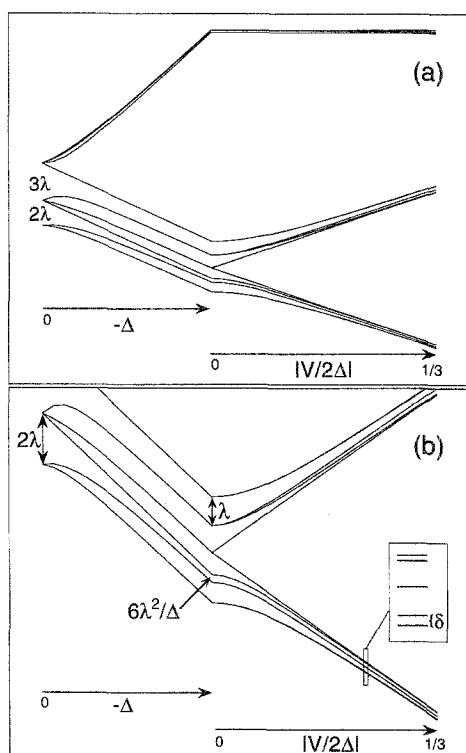


Fig. 31. Ligand field theory for the  ${}^5T_{2g}$  ground state of a  $-D$  system. Energy levels obtained from the solution of the full  ${}^5T_{2g}$  Hamiltonian. (a) All 15 energy levels plotted for increasing values of  $-\Delta$  and  $|V/2\Delta|$ ; the upper five levels correspond to the  ${}^5B_{2g}$  state and the lower ten levels to the  ${}^5E_g$  state. (b) Expansion of the ten  ${}^5E_g$  energy levels, which are split by axial ZFS ( $-\Delta$ ) into a manifold of five doublets spaced by  $\lambda$ ; the second doublet is further split by  $6\lambda^2/\Delta$  due to second-order spin-orbit coupling with the  ${}^5B_{2g}$  state. As rhombicity ( $V$ ) is introduced, the low-energy levels yield a doublet, singlet, doublet pattern and the lowest-energy doublet is split by the amount  $\delta$  (inset).

rule ordering of these levels for a  $T_2$  ground state in a more-than-half-filled  $d^6$  system. When  $-\Delta$  is non-zero, the 15 states split into a high-energy branch of five energy levels, corresponding to the  ${}^5B_{2g}$  ( $|0\rangle$ ) sublevels, and a low-energy branch of ten energy levels, corresponding to the  ${}^5E_g$  ( $|+1\rangle$ ,  $|-1\rangle$ ) sublevels, which are enlarged in Fig. 31(b). As the axial ZFS parameter  $-\Delta$  increases, these ten energy levels approach a splitting pattern of five effective doublets, separated by the amount  $\lambda$  (Fig. 31(b)); the second doublet is further split by the amount  $6\lambda^2/\Delta$  due to second-order coupling effects with the  ${}^5B_{2g}$  state. When rhombic ZFS is allowed, the middle doublet also splits and the ten levels separate into two clusters of five each. The low-energy cluster has a doubly degenerate ground state which is split by the amount  $\delta$  (see Fig. 31(b), inset), and the doublet, singlet, doublet splitting pattern produced converges toward the  $S=2$  spin Hamiltonian results for  $-D$  with  $E \neq 0$  (see Fig. 23, middle).

Zeeman perturbation causes the ground-state doublet to further split by the amount  $g\beta H \cos\theta$ , as shown in Fig. 32. The values of  $g_{\parallel}$  ( $g_z$ ) and  $g_{\perp}$  ( $g_x$  and  $g_y$ ) can thus be obtained from the splitting of the ground state under an applied magnetic field. A more accurate value of  $g_{\parallel}$  can be obtained by equating the slope of the lowest-energy level at high magnetic field to  $g\beta/2$ , which avoids the potential problem of curve crossing between the first and second excited-state sublevels. A plot of  $g_{\parallel}$  versus  $|V/2\Delta|$  is given in Fig. 33 for  $-\Delta = 200$  to  $3000 \text{ cm}^{-1}$ , though  $-\Delta$  much larger than  $2000 \text{ cm}^{-1}$  may not be physically meaningful for high-spin six-coordinate  $\text{Fe}^{2+}$  complexes with predominantly nitrogen and oxygen ligation. From Fig. 33,  $g_{\parallel}$  is between 9.5 and 10.0 for nearly all values of  $-\Delta$  at the axial limit and is substantially larger than the  $g_{\parallel} = 8.0$  obtained from the  $S=2$  spin Hamiltonian. As rhombicity is included and  $|V/2\Delta|$  approaches the rhombic limit,  $g_{\parallel}$  decreases, but never falls under 8.3. Reasonable values of  $-\Delta$  for a distorted octahedral environment are  $|\Delta| < \sim 800 \text{ cm}^{-1}$ , and so the range of  $g_{\parallel}$  values expected for six-coordinate  $-D$  complexes is  $\sim 8.8$  to 10.0, depending on the degree of rhombicity. In these calculations, molecular  $g$ -values of 2.00 were assumed, and since higher molecular  $g$ -values have been observed (see Table 1), the curves in Fig. 33 provide a lower limit for  $g_{\parallel}$ . Eq. (30) can also be solved for magnetic fields along the  $x$  or  $y$  directions to obtain an estimate of  $g_{\perp}$ . These calculations give  $g_{x,y} \approx 0.5$  at the axial limit and  $g_x \approx 0.7$

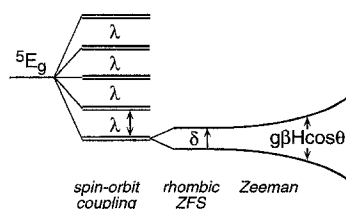


Fig. 32. The  ${}^5E_g$  ground state under spin-orbit coupling, rhombic ZFS, and Zeeman perturbations. Spin-orbit coupling perturbs the  ${}^5E_g$  ground state to produce a manifold of five doublets, spaced by  $\lambda$ . Rhombic ZFS removes the degeneracy of the lowest doublet and splits the two sublevels by  $\delta$ . A Zeeman perturbation continues to split the ground state by the amount  $g\beta H \cos\theta$ .

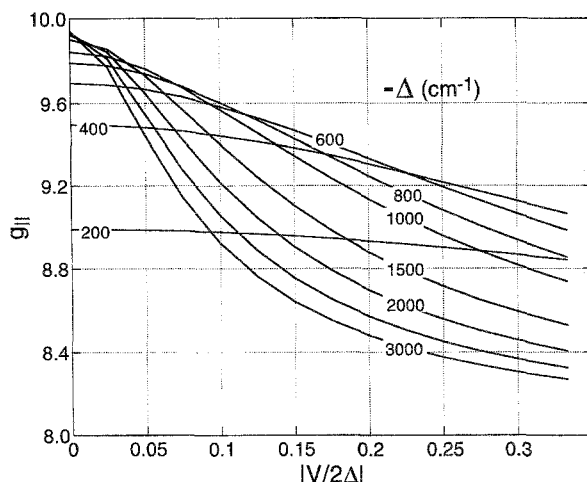


Fig. 33. Relationship between  $g_{\parallel}$  and the ligand field parameters  $-\Delta$  and  $V$  for a  ${}^5E_g$  ground state.  $g_{\parallel}$  calculated from the full  ${}^5T_{2g}$  Hamiltonian for a range of axial ( $-\Delta$ ) and rhombic ( $V$ ) ZFS parameters, using  $|V/2\Delta|=0$  at the axial limit to  $|V/2\Delta|=1/3$  at the rhombic limit and  $\lambda = -80 \text{ cm}^{-1}$ .

and  $g_y \approx 1.3$  at the rhombic limit, from which a reasonable value for a range of  $-\Delta$  and  $V$  values is  $g_{\perp} \approx 1$ .

The splitting of the ground-state doublet,  $\delta$ , can also be directly calculated from Eq. (30). Fig. 34(a) shows a series of  $\delta$  curves, each for a given  $-\Delta$ , obtained from the solution of Eq. (30) using  $\lambda = -80 \text{ cm}^{-1}$  and plotted as a function of  $|V/2\Delta|$ . Because  $\delta$  arises from rhombic ZFS effects,  $\delta$  is zero when  $V$  is zero, and  $\delta$  increases as  $|V|$  increases. Fig. 34(a) shows that the maximum  $\delta$  is  $\sim 6.5 \text{ cm}^{-1}$  and that the small  $-\Delta$  values appropriate for distorted octahedral geometry ( $-\Delta < \sim 800 \text{ cm}^{-1}$ ) give high  $\delta$  values under reasonable degrees of rhombicity. Because  $\delta$  also arises from spin-orbit coupling, the magnitude of the spin-orbit coupling parameter  $\lambda$  can affect  $\delta$ . Although a reduced  $\lambda$  value of  $-80 \text{ cm}^{-1}$  is generally acceptable for the  $\text{Fe}^{2+}$  systems considered here, small variations in covalency give a range of  $\lambda$  values. Fig. 34(b) replots  $\delta$  curves for a few values of  $-\Delta$  and allows for a spread on the value of  $\delta$  associated with a range of  $\lambda$ . The range of isotropic  $\lambda$  increases the maximum value of  $\delta$  to  $\sim 7 \text{ cm}^{-1}$  for  $-\Delta = 200 \text{ cm}^{-1}$  at the rhombic limit. Anisotropic covalency can also affect  $\delta$ ; however, this spread is smaller than the spread due to isotropic variation in  $\lambda$  shown in Fig. 34(b). (It should be noted that variations in the magnitude of  $\lambda$  have little effect on  $g$ -values.) Therefore, based on the plots in Fig. 34,  $\delta$  is expected to be between  $\sim 3$  and  $7 \text{ cm}^{-1}$  for six-coordinate  $\text{Fe}^{2+}$  protein sites with reasonable rhombic distortions,  $|V/2\Delta| > \sim 0.15$ .

The ground-state parameters obtained from fitting the saturation magnetization data can now be used to give estimates of the ligand field parameters  $\Delta$  and  $V$ . Matching the experimentally-derived value of  $g_{\parallel}$  to the curves in Fig. 33 while simultaneously matching  $\delta$  to the curves in Fig. 34(a) (and Fig. 34(b) if necessary) gives an estimate of  $-\Delta$  and  $|V/2\Delta|$  which defines the splitting of the  ${}^5T_{2g}$  ground

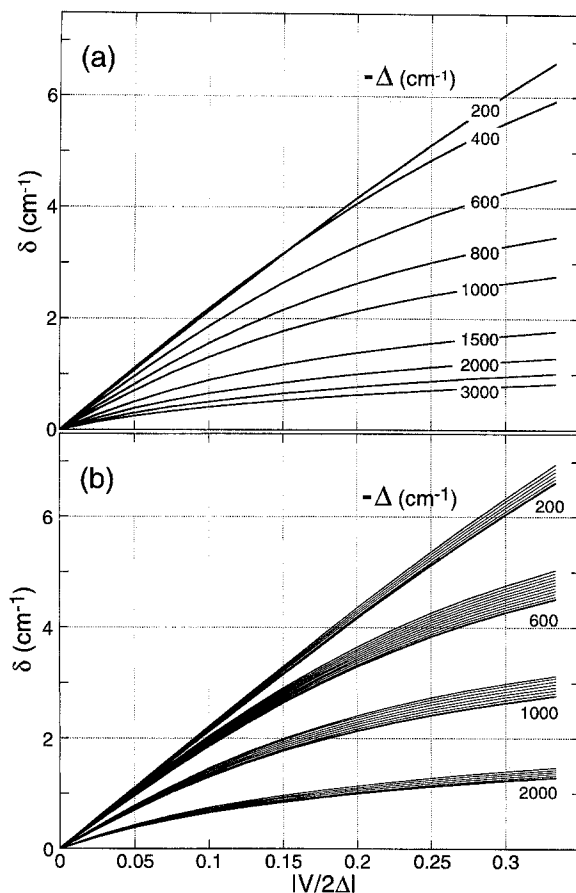


Fig. 34. Relationship between  $\delta$  and the ligand field parameters  $-\Delta$  and  $V$  for a  ${}^5E_g$  ground state.  $\delta$  calculated from the full  ${}^5T_{2g}$  Hamiltonian for  $|V/2\Delta|=0$  at the axial limit to  $|V/2\Delta|=1/3$  at the rhombic limit. (a)  $\delta$  for a range of  $-\Delta$  values using  $\lambda = -80 \text{ cm}^{-1}$ . (b)  $\delta$  for select values of  $-\Delta$  using  $\lambda = -80 \text{ cm}^{-1}$  (heavy line) to  $-85 \text{ cm}^{-1}$  (light lines) to account for small variations in covalency.

state. Combining this  ${}^5T_{2g}$  energy pattern with the observed energy splitting of the  ${}^5E_g$  excited state gives a complete d-orbital energy level diagram for a non-heme ferrous center.

### 3.4.2. Five-coordinate geometry

We now consider the ligand field origins of the ground-state spin Hamiltonian parameters for the idealized axial pentacoordinate ligand arrangements, square pyramidal and trigonal bipyramidal geometries.

**3.4.2.1. Square pyramidal, strong- and weak-axial** The  $d^6$  energy level diagram shown in Fig. 29 can be used to describe a square pyramidal complex as being a distortion from octahedral symmetry wherein the axial ZFS distortion results from the removal

of one octahedral ligand. With the removal of this ligand, the metal moves up out of the equatorial plane. If the metal rises far above the plane, the  $M-L_{\text{axial}}$  bond can shorten enough to create a strong-axial system (see Section 3.2). This case corresponds to a positive ZFS parameter  $D$  and a positive value of  $\Delta$  in Fig. 29, which results in a  ${}^5B_{2g}$  ground state. Therefore, the strong-axial square pyramidal system is treated as in Section 3.4.1.1.

As shown from ligand field calculations of the  $d^6$  orbital splittings (Section 3.2), removal of one octahedral ligand usually produces a weak-axial system, which has a  ${}^5E_g$  ( $d_{xz}$ ,  $d_{yz}$ ) ground state as shown in Fig. 12. This case is equivalent to  $-\Delta$  case as treated in Section 3.4.1.2. Like the corresponding octahedral case, the ground-state spin Hamiltonian parameters  $g_{\parallel}$  and  $\delta$  obtained from the VTVH MCD data of a weak-axial square pyramidal system can be matched to Figs. 33 and 34 to obtain the ligand field parameters  $-\Delta$  and  $V$ . Because removal of a ligand will stabilize the ( $d_{xz}$ ,  $d_{yz}$ ) orbitals more than an axial elongation in a six-coordinate site,  $-\Delta$  is expected to be larger for square pyramidal symmetry ( $-\Delta > \sim 800 \text{ cm}^{-1}$ ) than for octahedral symmetry. Therefore, from Fig. 33,  $g_{\parallel}$  can be as low as  $\sim 8.3$  at the rhombic limit. Large values of  $-\Delta$  will also give small values of  $\delta$ , as shown in Fig. 34(a), and  $\delta$  for square pyramidal sites is expected to be  $< \sim 4 \text{ cm}^{-1}$  for  $-\Delta > \sim 800 \text{ cm}^{-1}$ . Thus weak-axial square pyramidal sites can be distinguished from distorted octahedral sites by the low  $\delta$  values obtained from the ground-state saturation magnetization data.

**3.4.2.2. Trigonal bipyramidal** Unlike the square pyramidal cases, trigonal bipyramidal symmetry cannot be treated as a perturbation of octahedral symmetry. Instead, a trigonal ligand field distortion is applied directly to the  ${}^5D$  free ion state to produce a  ${}^5E''$  ground state with ( $d_{xz}$ ,  $d_{yz}$ ) lowest in energy, a  ${}^5E'$  ( $d_{x^2-y^2}$ ,  $d_{xy}$ ) excited state, and a  ${}^5A_1'$  ( $d_{z^2}$ ) excited state for high-spin  $Fe^{2+}$  complexes in  $D_{3h}$  symmetry [194,195], as shown in Fig. 35. The degeneracies of both  ${}^5E$  states can be removed by rhombic ZFS distortions, which split the  ${}^5E''$  ground state by  $V$  and the  ${}^5E'$  state by  $V'$ . Because the  ${}^5E''$  ground state contains in-state orbital angular momentum, the spin and orbital degeneracies must be coupled and a spin-orbit perturbation applied. Eq. (31) gives the Hamiltonian including spin-orbit coupling, rhombic ZFS, and Zeeman perturbations appropriate for the ground state of a trigonal bipyramidal system [196].

$$\begin{aligned} \mathcal{H}({}^5E'', tbp) = & \lambda(\vec{L} \cdot \vec{S}) + V(\hat{L}_x^2 - \hat{L}_y^2) \\ & + \beta\{(\hat{L}_x + 2\hat{S}_x)H_x + (\hat{L}_y + 2\hat{S}_y)H_y + (\hat{L}_z + 2\hat{S}_z)H_z\} \end{aligned} \quad (31)$$

This Hamiltonian is applied to the  ${}^5E''$  ground state by treating the d-orbitals as linear combinations of the  $M_L = \pm 1$  states, which are coupled with the  $M_S = \pm 2, \pm 1, 0$  states to produce ten eigenstates [196]. In-state spin-orbit coupling perturbs these ten energy levels and produces a manifold of five doublets which are spaced by  $\lambda$ , as shown in Fig. 36(a), similar to the results from the  ${}^5T_{2g}$  Hamiltonian with  $-\Delta$  (Section 3.4.1.2). When a rhombic splitting of the  ${}^5E''$  ground state is included, this manifold of five doublets divides into two clusters of five states each (Fig. 36(a)); the low-energy cluster has a doublet, doublet, singlet splitting pattern which con-

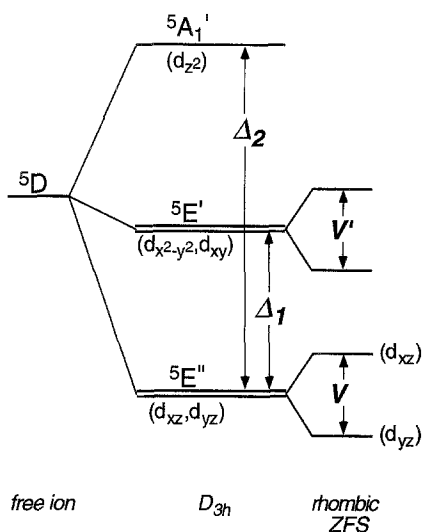


Fig. 35. Splitting pattern of the d-orbitals under trigonal bipyramidal symmetry. The  $d^6$  free ion parent state,  $^5D$ , is split under a trigonal ligand field into a  $^5E''$  ground state with  $^5E'$  and  $^5A_1'$  excited states at energies  $\Delta_1$  and  $\Delta_2$  above the ground state, respectively. A rhombic distortion removes the degeneracy of both  $^5E$  states, splitting the  $^5E''$  ground state by the amount  $V$  and  $^5E'$  by the amount  $V'$ .

verges with the  $S=2$  spin Hamiltonian results for  $-D$ . The magnitude of  $g_{\parallel}$  can be obtained from the solution of Eq. (31) by including the Zeeman perturbation along  $H_z$ . Similar to the  $^5T_{2g}$  with  $-\Delta$  case,  $g_{\parallel}$  is 10.0 at the axial limit and decreases to  $\sim 8.5$  under reasonable rhombic ZFS ( $V$ ), and  $g_{\perp}$  can be approximated as  $\sim 1$  when  $z$ -polarization is present.

Rhombic splitting ( $\delta$  in Fig. 36(b)) of the lowest doublet requires out of  $^5E''$  spin-orbit coupling. A more complete treatment of the trigonal bipyramidal case includes spin-orbit coupling over the entire  $^5D$  manifold of 25 eigenstates (coupling  $L=2$  and  $S=2$ ). Using  $\lambda = -80 \text{ cm}^{-1}$  as the spin-orbit coupling parameter for  $^5D$  and applying a trigonal field corresponds to the energy level diagram in Fig. 35, the trigonal bipyramidal ground-state doublet will split by a small amount ( $< 3 \text{ cm}^{-1}$ ) as indicated in Fig. 36(b). Therefore, like weak-axial square pyramidal geometry, trigonal bipyramidal geometry is characterized by a small value of the ground-state parameter  $\delta$ , with smaller values expected for trigonal bipyramidal symmetry due to the higher energy of the excited state involved in the spin-orbit coupling.

### 3.4.3. Four-coordinate geometry

Four-coordinate  $\text{Fe}^{2+}$  can range from tetrahedral to square planar geometry. Pure tetrahedral symmetry, however, is not observed due to Jahn-Teller distortions which will remove the degeneracy of the ground and excited states. Here we consider the two common tetragonal distortions on four-coordinate tetrahedral geometry, a flattened tetrahedron and an elongated tetrahedron, as well as the ideal square planar geometry.

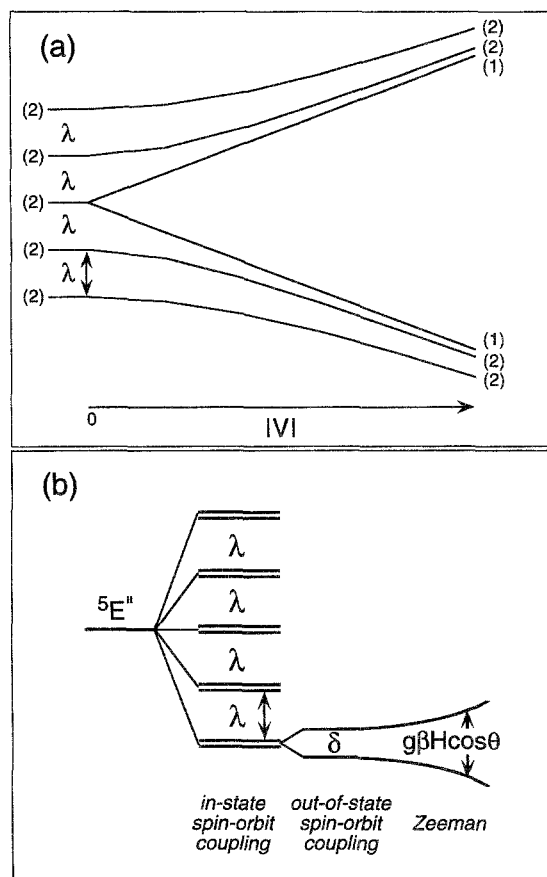


Fig. 36. Ligand field theory for the  ${}^5E''$  ground state in trigonal bipyramidal symmetry. Energy levels obtained from the solution of the  ${}^5E''$  trigonal bipyramidal Hamiltonian. (a) In-state spin-orbit coupling produces a manifold of five doublets spaced by  $\lambda$ , and a rhombic ZFS perturbation ( $V$ ) divides these into two clusters of five levels (degeneracies are given in parentheses). (b) Out-of-state spin-orbit coupling removes the degeneracy of the lowest doublet and splits the two sublevels by  $\delta$ . A Zeeman perturbation continues to split the ground state by the amount  $g\beta H \cos\theta$ .

**3.4.3.1. Distorted tetrahedral (flattened),  ${}^5A_1$  ground state** A tetrahedral ligand field splits the  $\text{Fe}^{2+}$  free ion state into a  ${}^5E$  ground state and a  ${}^5T_2$  excited state, separated by an energy  $10Dq(T_d)$  as shown in Fig. 37, center, where  $10Dq(T_d)$  is of the order of  $4000\text{ cm}^{-1}$  for oxygen and nitrogen ligation. Because the  ${}^5E$  ground state has no in-state orbital angular momentum, an  $S=2$  spin Hamiltonian is used to describe the behavior of the ground state. A positive axial ZFS parameter  $D$  corresponds to a distorted tetrahedron which has been flattened along the  $z$ -axis to produce a  ${}^5A_1$  ground state (Fig. 37, left) [197]. Eq. (32) gives the value of  $D$  for the  ${}^5A_1$  ground state which includes out-of-state spin-orbit coupling between the components of the  ${}^5E$  and  ${}^5T_2$  states; the molecular  $g_{\parallel}$  and  $g_{\perp}$  values are given in Eqs. (33) and (34) [198].

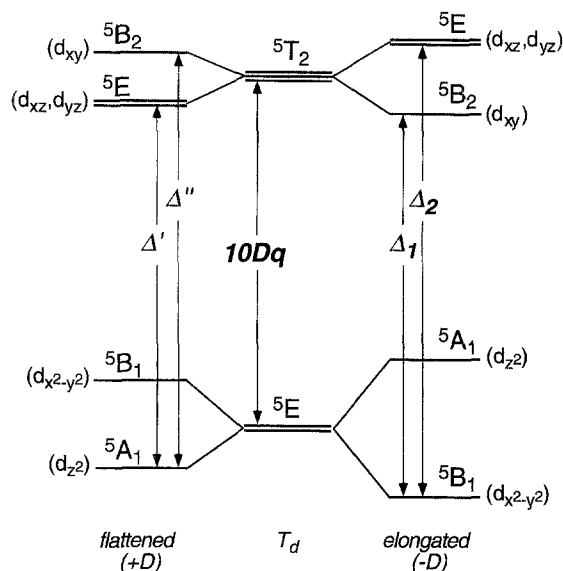


Fig. 37. Splitting pattern of the d-orbitals under distorted tetrahedral symmetry. The d-orbitals split under a tetrahedral ligand field into a  $^5E$  ground state and a  $^5T_2$  excited state, separated by  $10Dq$  (center). A distortion which flattens the tetrahedron along the  $z$ -axis (left) produces a  $^5A_1$  ground state and corresponds to positive ZFS ( $+D$ ). Elongating the tetrahedron (right) produces a  $^5B_1$  ground state and corresponds to a negative ZFS ( $-D$ ).

$$D = \frac{+3\lambda^2}{\Delta'} \quad (32)$$

$$g_{\parallel} = 2.00 \quad (33)$$

$$g_{\perp} = 2 \left( 1 - \frac{3\lambda}{\Delta'} \right) \quad (34)$$

In these equations,  $\lambda$  is the spin-orbit coupling parameter and  $\Delta'$  is the energy difference between the  $^5A_1$  ( $d_{z^2}$ ) ground state and the  $^5E$  ( $d_{xz}$ ,  $d_{yz}$ ) excited state [197], as shown in Fig. 37, left.

**3.4.3.2. Distorted tetrahedral (elongated),  $^5B_1$  ground state** An elongated tetrahedron corresponds to a negative ZFS parameter  $D$  [197] and produces a  $^5B_1$  ground state, as shown in Fig. 37, right. As with the flattened tetrahedral case, a spin Hamiltonian is appropriate where the parameters derive from out-of-state spin-orbit coupling. The resulting expressions for  $D$ ,  $g_{\parallel}$ , and  $g_{\perp}$  are given in Eqs. (35), (36), and (37), respectively [198].

$$D = \left( \frac{-4\lambda^2}{\Delta_1} + \frac{\lambda^2}{\Delta_2} \right) \quad (35)$$

$$g_{\parallel} = 2 \left( 1 - \frac{4\lambda}{\Delta_1} \right) \quad (36)$$



$$g_{\perp} = 2 \left( 1 - \frac{\lambda}{\Delta_2} \right) \quad (37)$$

$\lambda$  is again the spin-orbit coupling parameter,  $\Delta_1$  is the energy corresponding to the transition from the ground state to the second-highest excited state ( ${}^5B_2$ ), and  $\Delta_2$  is the energy to the highest excited state ( ${}^5E$ ) as shown in Fig. 37, right. While little ground-state information is available on four-coordinate complexes, these sites are distinguished from other geometries by their low excited-state energies (see Section 3.2).

**3.4.3.3. Square planar** In the limit of flattening a tetrahedron all the way into the  $xy$ -plane, a square planar geometry is produced. The  $d_{z^2}$  orbital drops down in energy and the ground state of this system is the singly degenerate  ${}^5A_{1g}$  state (Fig. 38) which gives a positive ZFS parameter. There is no in-state angular momentum and the spin Hamiltonian is appropriate, which means that the square planar case can be treated like the  $+D$ /flattened tetrahedral case in Section 3.4.3.1. However, square planar geometry is not expected for protein sites since they contain large degrees of distortion. The mineral gillespite [199] is the only known example of a square planar ferrous site and is characterized by the excited-state transitions observed at  $\sim 8000 \text{ cm}^{-1}$  ( $\Delta''$ ) and  $\sim 20\,000 \text{ cm}^{-1}$  ( $\Delta'''$ ) [170].

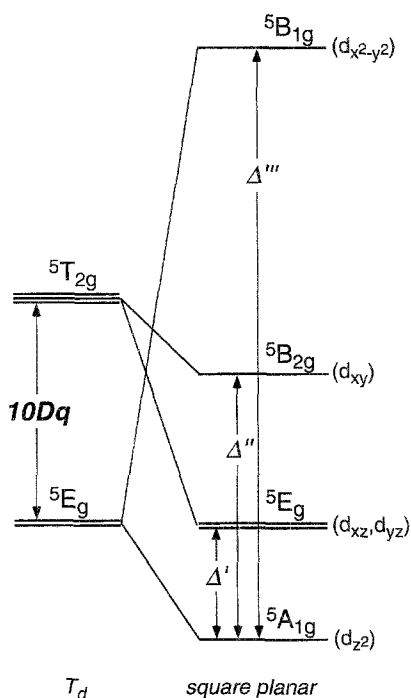


Fig. 38. Splitting pattern of the d-orbitals under square planar symmetry. Flattening a tetrahedron into the  $xy$ -plane produces a square planar geometry, which has a non-degenerate  ${}^5A_{1g}$  ( $d_{z^2}$ ) ground state.

### 3.4.4. FeSOD revisited

The methodology outlined above can now be applied to the FeSOD data in Fig. 7 to obtain an experimentally-derived energy level diagram. In Section 3.2, the geometry of the ferrous center in FeSOD was determined to be five-coordinate square-pyramidal, and the  $^5E_g$  excited state energies are observed at  $\sim 10\,500$  and  $\sim 5000\text{ cm}^{-1}$  (Fig. 7(a–c)). Analysis of the FeSOD saturation magnetization data in Section 3.3.3 gave the parameters  $\delta = 2.9\text{ cm}^{-1}$  and  $g_{\parallel} = 8.78$  for a non-Kramers doublet ground state, indicating a negative ZFS parameter  $D$ . From this information, the appropriate treatment for the ligand field origin of the ground-state spin Hamiltonian parameters is the five-coordinate, square pyramidal, weak-axial case (Section 3.4.2.1), in which  $g_{\parallel}$  and  $\delta$  are related to the ligand field parameters  $-\Delta$  and  $V$  by Figs. 33 and 34. Matching the FeSOD values of  $g_{\parallel}$  and  $\delta$  to these plots gives  $-\Delta = 1000 \pm 300\text{ cm}^{-1}$  and  $V/2\Delta = 0.30 \pm 0.05$ , and thus provides the splitting of the  $t_{2g}$  orbitals. Combining these ground-state d-orbital splittings with the excited-state d-orbital splittings gives a complete energy level diagram for the  $\text{Fe}^{2+}$  site in FeSOD (Fig. 39). The energy splittings of the d-orbitals in Fig. 39 provide detailed insight into the geometric and electronic structure of the ferrous site and can be used to gain molecular-level insight into the catalytic mechanism. This is demonstrated through application to three important enzyme systems in the next section.

## 4. Structure/function applications to mononuclear non-heme ferrous enzymes

Three mononuclear non-heme iron systems (PDO, LOs, and BLM) are presented below as examples for the application of the above methodology which demonstrate its utility in providing structure/function insight into dioxygen reactivity.

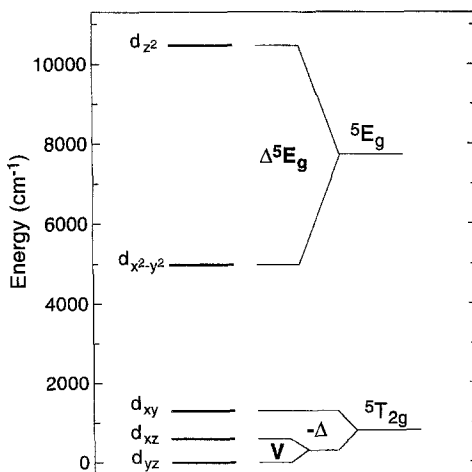


Fig. 39. Experimentally derived energy level diagram for FeSOD. The splitting of the  $^5E_g$  levels is determined from the observed absorption, CD, and MCD transitions (Fig. 7(a–c)). The splitting of the  $^5T_{2g}$  levels is obtained by relating the ground-state spin Hamiltonian parameters  $\delta = 2.9\text{ cm}^{-1}$  and  $g_{\parallel} = 8.78$  to the ligand field parameters  $V$  and  $\Delta$  as described in Section 3.4.

#### 4.1. Phthalate dioxygenase (PDO)

PDO contains two metal centers, the mononuclear non-heme iron site, believed to be the active site in oxygen reactivity [20], and the binuclear  $[2\text{Fe}-2\text{S}]$  Rieske cluster, which complicates spectral studies on the native ferrous center. In its reduced and catalytically active form, the Rieske site contains one high-spin ferric ion and one high-spin ferrous ion antiferromagnetically coupled to produce a paramagnetic, MCD  $\mathcal{G}$ -term-active  $S=1/2$  ground state [70]. In its oxidized form, the Rieske site contains two high-spin ferric ions antiferromagnetically coupled to produce an  $S=0$  ground state that is MCD  $\mathcal{G}$ -term-inactive. Thus MCD should allow one to probe the non-heme ferrous site which is paramagnetic even in the presence of the intense absorption features of the Rieske center [74,75]. However, Fig. 40(a) shows the low-temperature MCD spectrum of apoPDO (no mononuclear iron, but oxidized

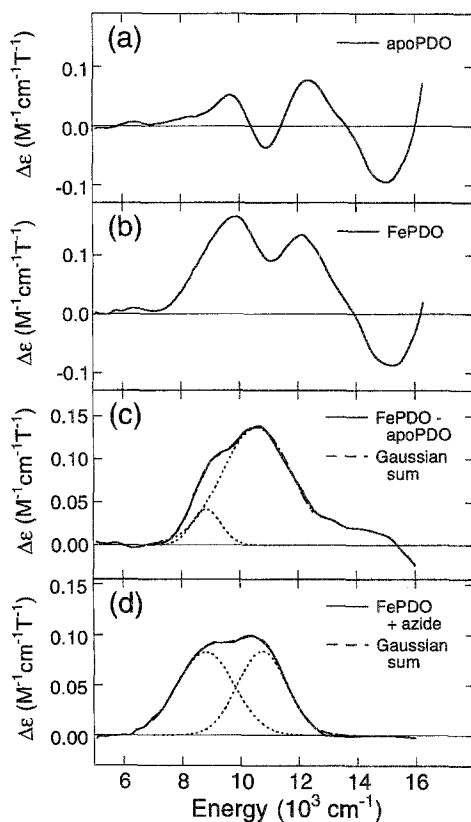


Fig. 40. Low-temperature MCD of apoPDO, FePDO, and FePDO with azide. (a) MCD spectrum of apoPDO. (b) MCD spectrum of FePDO. (c) Difference MCD spectrum of FePDO minus apoPDO; the dashed line shows the best Gaussian fit to the data. (d) MCD spectrum of FePDO +  $160 \times$  azide minus the spectrum of apoPDO +  $160 \times$  azide; the dashed line shows the best Gaussian fit to the data. All spectra were recorded at 5 K and 7 T.

Rieske site intact) which arises from temperature-independent  $\mathcal{B}$ -term intensity resulting from field-induced mixing of electronic states (see Section 3.1.2) and a small paramagnetic impurity in the sample. Therefore, to obtain an accurate spectrum for the native ferrous active site in PDO, the apoPDO spectrum was subtracted from the spectrum in Fig. 40(b) of FePDO (one molar equivalent of ferrous ion added relative to active sites) and the difference spectrum is shown in Fig. 40(c). Gaussian resolution identifies two bands at 8850 and 10 580  $\text{cm}^{-1}$  with  $\Delta^5E_g \approx 1730 \text{ cm}^{-1}$ , which from Section 3.2 is indicative of a six-coordinate, distorted octahedral active site geometry. Azide was used as a small-molecule oxygen analog and the addition of 160 molar equivalents ( $160 \times$ ) to apoPDO alters the MCD spectrum. Subtraction of the matched apoPDO +  $160 \times$  azide sample from the spectrum of FePDO plus  $160 \times$  azide gives the difference spectrum shown in Fig. 40(d). This can be fit with two Gaussian bands at 8810 and 10 740  $\text{cm}^{-1}$ , giving  $\Delta^5E_g \approx 1930 \text{ cm}^{-1}$  and indicating a different six-coordinate geometry from that in the resting enzyme. Therefore azide binds to the ferrous site replacing one endogenous ligand and perturbing the ligand field environment.

The MCD spectrum of FePDO with a five-fold ( $5 \times$ ) molar excess of phthalate substrate was corrected for low-temperature MCD contributions from an apoPDO +  $5 \times$  phthalate sample and the difference spectrum is shown in Fig. 41(a). Three distinct peaks are observed in the ferrous  $d \rightarrow d$  region of the NIR MCD spectrum: one low-energy band at  $< 5000 \text{ cm}^{-1}$  and two high-energy bands Gaussian resolved at 9070 and 11 460  $\text{cm}^{-1}$ , indicating the presence of at least two species. The lowest- and highest-energy bands are split by  $> 6000 \text{ cm}^{-1}$ , which is indicative of a five-coordinate, square pyramidal FePDO–phthalate complex. It has been postulated that the remaining MCD intensity in the 9000–10 000  $\text{cm}^{-1}$  region was due to residual six-coordinate resting enzyme which did not fully convert upon substrate binding even at saturating concentrations [74]. However, this explanation was based on data from which the apoPDO + substrate MCD spectrum was not subtracted. In fact, the simulation shown in Fig. 41(b) (dashed line) which fixes the band energies and widths from the Gaussian analysis of resting FePDO yet allows their intensities as well as a third peak to float freely does not accurately fit the data. This indicates that the 9070  $\text{cm}^{-1}$  band does not originate from residual resting enzyme, but rather from a second iron coordination environment of the FePDO–substrate complex.

Based upon its energy below 10 000  $\text{cm}^{-1}$ , the 9070  $\text{cm}^{-1}$  feature could be assigned as the high-energy spectral component of a five-coordinate, more trigonal bipyramidal ferrous site, in which case a second transition would be expected below the range of the NIR spectrometer (see Section 3.2). Alternatively, this feature could be assigned as the low-energy spectral component of a six-coordinate distorted octahedral ferrous site, in which case a second band would be present at 1000–2000  $\text{cm}^{-1}$  higher energy and overlap the 11 460  $\text{cm}^{-1}$  band of the five-coordinate square pyramidal component. Based on X-ray absorption near-edge spectroscopy (XANES) of the  $\text{Co}^{2+}$ -substituted enzyme which is consistent with a pure five-coordinate mononuclear metal site [73], it is reasonable to assign the 9070  $\text{cm}^{-1}$  band in the MCD spectrum as originating from a five-coordinate, enzyme–substrate complex with a

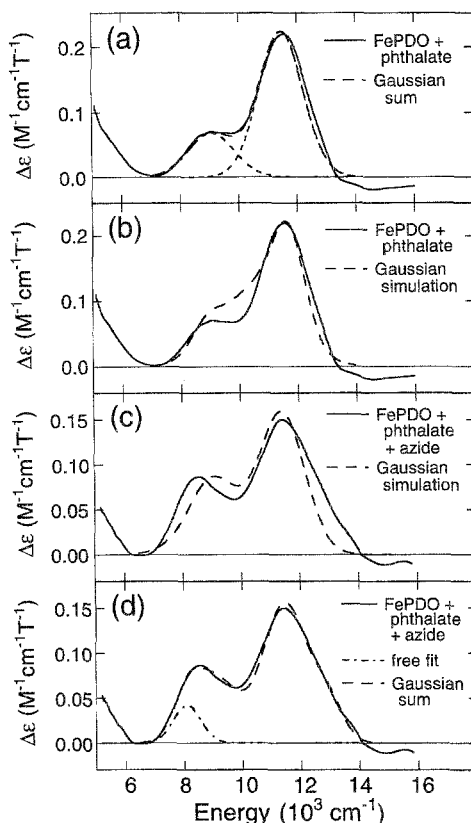


Fig. 41. Low-temperature MCD of the FePDO–substrate complex, with and without azide. (a) MCD spectrum of FePDO +  $5 \times$  phthalate minus the spectrum of apoPDO +  $5 \times$  phthalate; the dashed line shows the best Gaussian fit to the data. (b) Simulation (dashed line) of plot (a) using the two peaks from the best fit of resting FePDO and allowing a third free-floating peak to fit the rest of the spectrum. (c) MCD spectrum (solid line) of FePDO +  $5 \times$  phthalate +  $120 \times$  azide minus the matched apoPDO spectrum. Simulation (dashed line) using the two peaks from the best fit of enzyme–substrate data and the two peaks from the best fit of enzyme–azide data. (d) Second simulation (dashed line) of plot (c) using the two peaks from the best fit of enzyme–substrate data and allowing for an additional free-floating peak to fit the rest of the spectrum.

more trigonal bipyramidal ligand field environment than the predominant five-coordinate, square pyramidal species responsible for the  $<5000$  and  $11\,460\text{ cm}^{-1}$  peaks. Substrate analog studies [20] indicate that phthalate does not bind directly to the iron, but rather induces a conformational change at the ferrous site through hydrogen bonding interactions. Thus, substrate does bind fully to the enzyme and perturbs the mononuclear ferrous site by eliminating an endogenous ligand and thus lowering the coordination number from six to five.

Simultaneous substrate and exogenous ligand binding to FePDO was also investigated for mechanistic insight. Fig. 41(c) shows the low-temperature MCD spectrum of FePDO +  $5 \times$  phthalate with 120-fold molar excess ( $120 \times$ ) of azide, from which

the corresponding apoPDO spectrum was subtracted. The low-energy peak position is shifted and there is  $\sim 25\%$  loss of intensity in the  $11\,460\text{ cm}^{-1}$  band relative to the enzyme–substrate spectrum (Fig. 41(a)), indicating that some of the five-coordinate, square pyramidal ferrous site has converted into another species with different spectral features and coordination environment. Owing to the mixture of species present in the enzyme–substrate complex (*vide supra*), it is difficult to discern whether the trigonal bipyramidal component also reacts with azide.

One possible effect of azide binding is to simply displace substrate and bind to the ferrous site to form the same six-coordinate FePDO–azide complex observed when azide binds to the resting enzyme alone (Fig. 40(d)). A simulation was performed which used the energies and widths from the individual enzyme–azide (Fig. 40(d)) and enzyme–substrate (Fig. 41(a)) Gaussian analyses and is shown by the dashed line in Fig. 41(c). Allowing the transition intensities to vary does not reasonably fit the data, and it can be concluded that addition of azide does not displace substrate, but rather binds to form a ternary enzyme–substrate–azide complex with distinct spectral features. Therefore, a fit was performed assuming only contributions from the five-coordinate, square pyramidal enzyme–substrate complex and allowing for a third free-floating peak corresponding to the ternary enzyme–substrate–azide complex. Fig. 41(d) clearly shows that in addition to residual enzyme–substrate contributions, a third peak at  $\sim 8100\text{ cm}^{-1}$  is required to fit the spectrum and its position suggests that the enzyme–substrate–azide complex is either a five-coordinate, trigonal bipyramidal or a six-coordinate, distorted octahedral complex. It is reasonable to assume that azide binds in the open coordination position created by substrate binding, producing a six-coordinate ferrous center, rather than displaces an additional endogenous ligand. Such a six-coordinate species would require there to be a second band at  $\sim 2000\text{ cm}^{-1}$  higher energy, although this transition would be obscured by the residual intensity from the non-azide-bound enzyme–substrate complexes. The  $\sim 8100\text{ cm}^{-1}$  band is lower in energy than expected for typical oxygen and nitrogen ligation on a six-coordinate complex (see Section 3.2). This indicates a lower ligand field strength at the ferrous site resulting from azide binding weakly to the iron due to reduced sigma overlap because of the azide orientation or a long Fe–N(azide) bond, either of which would occur from steric hindrance between the substrate and the exogenous ligand at the metal center.

The spectroscopically derived changes in the coordination environment at the mononuclear ferrous active site in PDO due to substrate and exogenous ligand binding are summarized in Fig. 42. The resting enzyme contains one six-coordinate species and the binary enzyme–substrate complex consists of a mixture of two different five-coordinate species, one approximately square pyramidal and one more distorted toward trigonal bipyramidal. PDO appears to be the first mononuclear non-heme ferrous enzyme found to exhibit a decrease in the coordination number upon substrate addition, where substrate binds to the protein pocket near the ferrous center and induces a conformation change at the iron site. The loss of one ligand at the active site in PDO when substrate binds may serve to produce a coordinatively unsaturated square pyramidal ferrous center which is then able to bind and activate oxygen, as demonstrated by the formation of a ternary complex upon azide addition.

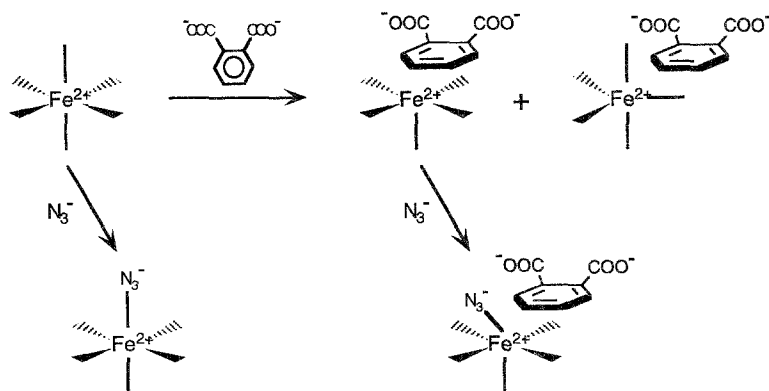


Fig. 42. Proposed changes in the mononuclear  $\text{Fe}^{2+}$  site coordination environment of PDO. The effects of exogenous ligand and substrate binding on the mononuclear non-heme iron site.

The fact that azide binds more weakly to the mononuclear iron in the enzyme–substrate complex relative to the resting enzyme ( $K_B \approx 2 \text{ M}^{-1}$  versus  $300 \text{ M}^{-1}$ , respectively [75]) appears to be due to the presence of substrate which sterically interferes with the open coordination site. Thus, using azide binding to model oxygen interactions, the MCD spectral studies indicate that the oxygen binding site is in close proximity to the aromatic ring of the substrate, positioning the bound oxygen intermediate and substrate for product formation.

#### 4.2. Lipoxygenases (LOs)

The two recent crystal structures of ferrous soybean lipoxygenase-1 (SLO-1) [100,101] and earlier spectral data [33,98,99,137] have generated some inconsistency concerning the metal coordination environment (see Fig. 2(c)). Fig. 43(a) (solid line) shows the 276 K NIR CD spectrum of native SLO-1. There is a low-energy feature below  $6000 \text{ cm}^{-1}$ , a second feature at  $10\,700 \text{ cm}^{-1}$  with a shoulder at  $\sim 8000 \text{ cm}^{-1}$ , and residual negative intensity at  $9200 \text{ cm}^{-1}$ . Addition of glycerol (the usual glassing agent for most low-temperature studies) to native SLO-1 produces the NIR CD spectrum in Fig. 43(a) (dashed line). Gaussian resolution of this spectrum indicates a positive band at  $8600 \text{ cm}^{-1}$  and a negative band at  $10\,300 \text{ cm}^{-1}$  to give  $\Delta^5 E_g \approx 1700 \text{ cm}^{-1}$ . From Section 3.2, this splitting is consistent with a six-coordinate, distorted octahedral geometry. Addition of sucrose (an alternative low-temperature glassing agent) to native SLO-1 reproduced the NIR CD spectrum in Fig. 43(a) (solid line) and resulted in the low-temperature NIR MCD spectrum in Fig. 43(b) (solid line), with three positive peaks at  $< 6000$ ,  $9200$  and  $10\,500 \text{ cm}^{-1}$ . As no ligand field geometry of a single high-spin ferrous site shows more than two  $d \rightarrow d$  transitions in the  $5000\text{--}13\,000 \text{ cm}^{-1}$  region (Section 3.2), native SLO-1 (in sucrose) must exist as a mixture of species. The MCD spectrum of SLO-1 in glycerol is shown in Fig. 43(b) (dashed line) with two positive bands at  $8600$  and  $10\,300 \text{ cm}^{-1}$ , the same energies and  $\Delta^5 E_g$  splitting as in the corresponding CD spectrum. Comparison of

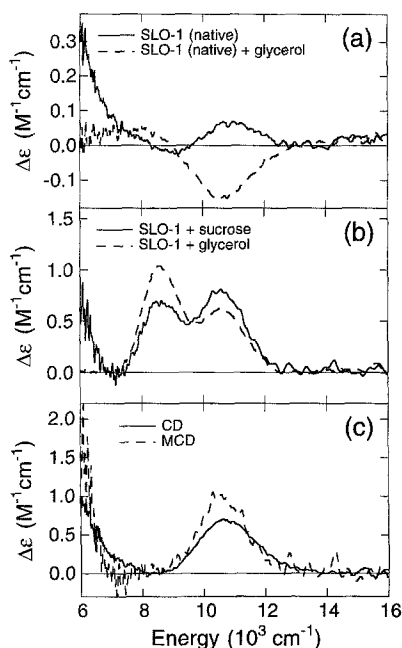


Fig. 43. CD and MCD of SLO-1. (a) CD spectra at 276 K of native SLO-1 (solid lines) and native SLO-1 + 50% (v/v) glycerol (dashed lines). (b) Low-temperature MCD spectra of native SLO-1 in saturated sucrose solution (solid lines) and native SLO-1 + 50% (v/v) glycerol (dashed lines). (c) CD at 276 K (solid lines) and low-temperature MCD (dashed lines) spectra of native SLO-1 (in sucrose) minus 60% (native SLO-1 + 50% glycerol).

the CD and MCD spectra indicates that the six-coordinate species of SLO-1 in glycerol may be contributing to the native SLO-1 (in sucrose) CD and MCD spectra. Subtraction of 60% of this species from the native spectra and renormalization gives the CD (solid line) and MCD (dashed line) spectra in Fig. 43(c) which correspond to the second component in the native enzyme mixture. These spectra have two positive  $d \rightarrow d$  bands at  $\sim 5000$  and  $10\,600 \text{ cm}^{-1}$  which from Section 3.2 indicate a five-coordinate, square pyramidal geometry with  $\Delta^5 E_g \approx 5600 \text{ cm}^{-1}$ . Thus, native SLO-1 exists as a 40/60 mixture of five- and six-coordinate species, respectively.

These spectroscopic results indicate that in addition to the four common ligands of both crystal structures (three His–N and one carboxylate–O), both the five- and six-coordinate sites in solution likely contain a water based ligand (*vide supra*). The main difference between the two crystal structures of SLO-1 is the coordination of the side chain of Asn<sub>694</sub>. The Boyington et al. structure has the Asn<sub>694</sub> side chain at  $3.3 \text{ \AA}$  from the iron [100], while the Minor et al. structure has the O $\delta$ 1 of Asn<sub>694</sub> bound to the iron [101]. The coordination difference between the two forms of native SLO-1 may relate to the difference in binding of Asn<sub>694</sub> which is at the end of a cavity starting at the surface of the enzyme and may be linked to the fatty acid binding site. The addition of ethanol or ethylene glycol to native SLO-1 has the



same effect as the addition of glycerol, namely shifting the five- and six-coordinate mixture to the purely six-coordinate form. Anaerobic addition of substrate (linoleate) gives the same result. Therefore, when linoleate (or alcohols) are present at the fatty acid binding site, a change in the active site environment occurs which may allow the O $\delta$ 1 of Asn<sub>694</sub> to bind to the iron, converting the ferrous site to the pure six-coordinate form.

The ground-state properties of each component of this mixture of sites can be probed independently using VTVH MCD. Saturation magnetization data were collected for the bands associated with the pure five-coordinate (at 5800 cm<sup>-1</sup>) and six-coordinate (at 8600 cm<sup>-1</sup>) sites and are plotted in Fig. 44(a) and 44(b), respectively, as intensity versus  $\beta H/2kT$  for a series of fixed temperatures. The saturation curves exhibit a high degree of nesting, indicating an integer spin  $M_S = \pm 2$  ground state with a large rhombic ZFS (Section 3.3.3). The MCD data were initially fit with Eq. (20), plus the term  $B_0H$  to account for linear  $\mathcal{B}$ -terms, assuming that the transitions were purely  $xy$ -polarized (see Section 3.3.3). A fit to the the saturation magnetization data for the five-coordinate site gives  $-D$  and  $\delta$  parameters at the upper limit of possible values (vide infra), so the  $+D$  model was also considered. Application of the three-level  $+D$  model (Section 3.3.4) to these data gives energy levels at 0, 7, and 15 cm<sup>-1</sup> (Fig. 44(a), lines), which correspond to spin Hamiltonian values of  $D \approx +10$  cm<sup>-1</sup> and  $|E/D| \approx 0.1$ . If an  $xy$ -polarized  $-D$  model is applied to the VTVH MCD data from the six-coordinate site of SLO-1 in glycerol, a 1.5%  $\mathcal{B}$ -term and

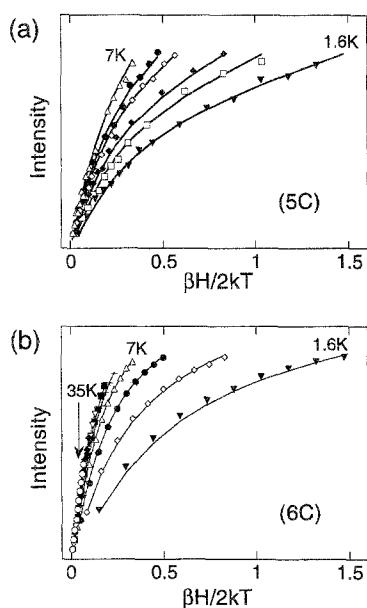


Fig. 44. Saturation magnetization data for native SLO-1. VTVH intensity (symbols) and fits (solid lines) plotted as a function of  $\beta H/2kT$  for (a) the 5800 cm<sup>-1</sup> band of SLO-1 + sucrose, originating from the five-coordinate species and (b) the 8600 cm<sup>-1</sup> band of SLO-1 + glycerol, originating from the six-coordinate species (the 8600 cm<sup>-1</sup> band data of SLO-1 + sucrose fit with the same parameters).

the parameters  $\delta = 10 \text{ cm}^{-1}$  and  $g = 10.5$  are obtained. Neither the  $\delta$  nor  $g_{\parallel}$  values lie in the expected ranges, indicating that a  $+D$  model must also be considered. Application of the three-level  $+D$  model gives an energy level spacing of 0, 10, and  $18 \text{ cm}^{-1}$ , corresponding to  $D = +13 \text{ cm}^{-1}$  and  $E/D = 0.1$ , which are well within the range expected for  $+D$  values (Section 3.4.1.1). This fit, shown in Fig. 44(b), lines, also describes the SLO-1 in sucrose VTVH MCD data, confirming that these two sites are very similar.  $z$ -Polarization contributions were considered for all of the SLO-1 VTVH data, but were not found to substantially improve the fits. The methodology outlined in Section 3.4 can be applied to these ground-state spin Hamiltonian parameters to extract the ligand field parameters  $\Delta = +700 \pm 200 \text{ cm}^{-1}$  and  $|V/2\Delta| = 0.19 \pm 0.05$  for the five-coordinate SLO-1 site and  $\Delta = +450 \pm 200 \text{ cm}^{-1}$  and  $|V/2\Delta| = 0.16 \pm 0.05$  for the six-coordinate SLO-1 site. As predicted from Section 3.4, the five-coordinate species has a larger  ${}^5T_{2g}(\Delta)$  splitting than the six-coordinate species, consistent with the greater distortion from octahedral symmetry.

The studies on the plant 15-LO enzyme SLO-1 have been extended to the mammalian 15-LOs human recombinant (15-HLO) and rabbit reticulocyte (15-RLO). In contrast to the above data on SLO-1, glycerol does not perturb the CD spectra of the mammalian enzymes [103]. The MCD spectra of 15-HLO and 15-RLO in glycerol are shown in Fig. 45(a) and 45(c), respectively. For 15-HLO, a band at  $8750 \text{ cm}^{-1}$  is dominant with a shoulder at  $\sim 10\,700 \text{ cm}^{-1}$  to give  $\Delta^5E_g \approx 2000 \text{ cm}^{-1}$ . Similarly, 15-RLO also exhibits an asymmetric band with a maximum at  $8650 \text{ cm}^{-1}$  and a shoulder to higher energy at  $\sim 10\,300 \text{ cm}^{-1}$  to give  $\Delta^5E_g \approx 1650 \text{ cm}^{-1}$ . Thus, the excited-state splittings are consistent with six-coordinate ferrous active site structures with no evidence for the presence of multiple components. Comparison of the amino acid sequences [200,201] shows that in mammalian 15-LOs, a histidine replaces the Asn<sub>694</sub> present in SLO-1. As histidine is a better ligand for  $\text{Fe}^{2+}$  than asparagine, the pure six-coordinate form would directly result from this substitution. This ligand substitution is supported by the VTVH MCD data collected for the mammalian enzymes at  $8600 \text{ cm}^{-1}$  which is shown in Fig. 45(b) (15-HLO) and 45(d) (15-RLO). The saturation magnetization data of the two different mammalian LOs are extremely similar to each other; however, the mammalian VTVH MCD data are qualitatively quite different from the six-coordinate SLO-1 saturation magnetization data (Fig. 44(b)), showing much less nesting than for the plant enzyme. Assuming an  $M_S = \pm 2$  ground state and purely  $xy$ -polarized transitions, application of the  $-D$  model gives an  $\sim 2.5\%$   $\mathcal{B}$ -term,  $g_{\parallel} \approx 9$ , and  $\delta \approx 4 \text{ cm}^{-1}$  for 15-HLO and 15-RLO. None of the mammalian enzyme fits was improved with the inclusion of  $z$ -polarization. The data are well described by the  $-D$  model, and when a three-level  $+D$  fit was attempted, the energy of the third level floated above the experimental range, further supporting the  $-D$  analysis. Applying the methodology outlined in Section 3.4.1.2, the values of  $\Delta = -500 \pm 200 \text{ cm}^{-1}$  and  $|V/2\Delta| = 0.27 \pm 0.05$  are obtained for both 15-RLO and 15-HLO, giving a  $\Delta$  comparable in magnitude to the value obtained for the six-coordinate form of SLO-1 ( $\Delta = +450 \text{ cm}^{-1}$ ), but with the opposite sign.

The experimental d-orbital energy level diagrams are summarized in Fig. 46(a) for

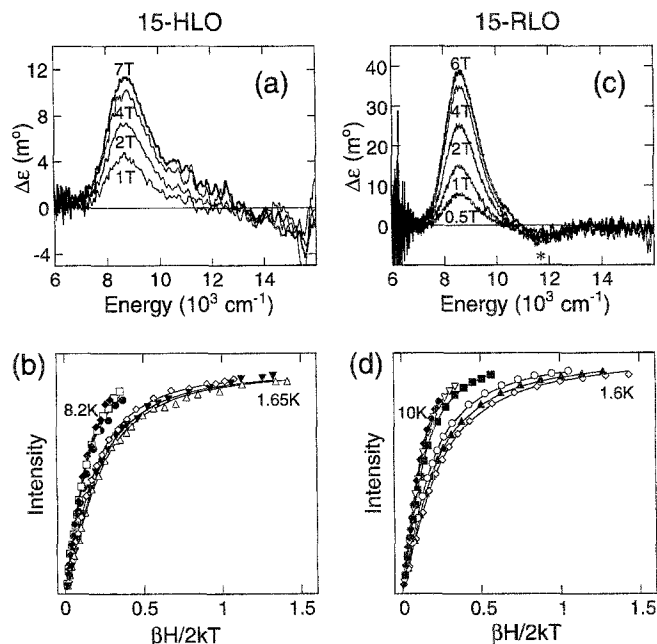


Fig. 45. MCD of 15-HLO and 15-RLO. (a) MCD spectra at 4.2 K of native 15-HLO in 50% (v/v) glycerol (the number on top of each spectrum indicates the magnetic field in Tesla applied to the sample). (b) VTVH intensity (symbols) and fits (solid lines) plotted as a function of  $\beta H/2kT$  for native 15-HLO in 50% (v/v) glycerol obtained for the  $8600\text{ cm}^{-1}$  band. (c) MCD spectra at 4.2 K of native 15-RLO in 50% (v/v) glycerol (the number on top of each spectrum indicates the magnetic field in Tesla applied to the sample). The negative intensity denoted by the asterisks is due to a heme impurity. (d) VTVH intensity (symbols) and fits (solid lines) plotted as a function of  $\beta H/2kT$  for native 15-RLO in 50% (v/v) glycerol obtained for the  $8600\text{ cm}^{-1}$  band.

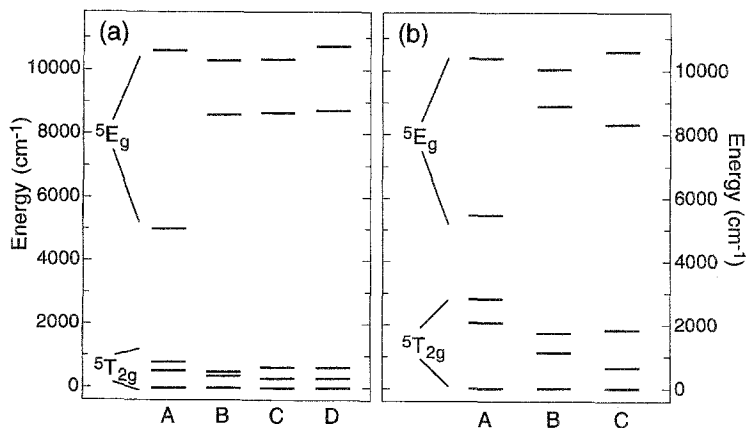
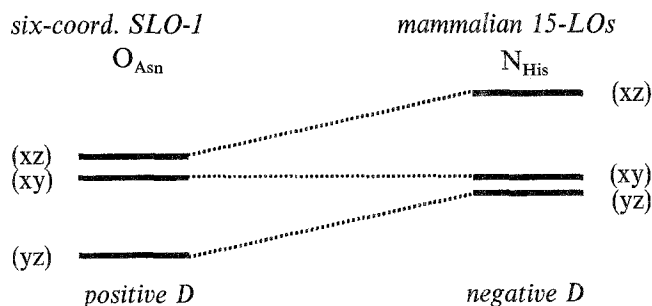


Fig. 46. Energy level diagrams for LOs. (a) Experimental d-orbital splittings for: A, five-coordinate SLO-1; B, six-coordinate SLO-1; C, 15-HLO; D, 15-RLO. (b) The d-orbital splittings obtained through a ligand field calculation for: A, five-coordinate SLO-1; B, six-coordinate SLO-1; C, 15-HLO and 15-RLO.

the five- and six-coordinate SLO-1 components, 15-HLO, and 15-RLO. The five-coordinate SLO-1 species shows dramatically different excited-state splittings compared to those of the mammalian enzymes, while the excited-state splittings of the six-coordinate SLO-1 species are similar to the mammalian species. Ligand field calculations such as those presented in Section 3.2 have been performed on the five- and six-coordinate active site models of SLO-1 built upon the crystallographic results [100,101], where  $z$  lies along the Fe–His<sub>499</sub> bond, and using the  $\alpha_2$  and  $\alpha_4$  parameters listed in Table 3 as starting values [103]. The resulting energy levels are shown in Fig. 46(b), A and B. Comparison to the experimentally observed d-orbital splittings of the two forms of native SLO-1 (Fig. 46(a)) shows that the five- and six-coordinate calculations in Fig. 46(b) accurately model the observed splittings. The distorted tetrahedral four-coordinate ligand field calculations from Section 3.2 predict two low-energy transitions in the NIR region; ligand field calculations on the Boyington et al. structure (a distorted octahedron missing two *cis* ligands) [103] predict a third high-energy transition at  $>13\,000\text{ cm}^{-1}$ . Neither of these patterns is observed experimentally for SLO-1, ruling out a four-coordinate structure for SLO-1 in solution.

A ligand field calculation was also performed on six-coordinate SLO-1 structure from above in which the asparagine-oxygen has been replaced with a histidine-nitrogen to model the mammalian 15-LO ferrous site. Comparison of the resulting calculated d-orbital energy levels (Fig. 46(b), C) to the experimentally observed transitions for 15-RLO and 15-HLO (Fig. 46(a), C and D) shows qualitative agreement for the  $^5E_g$  splittings. The calculated  $^5T_{2g}$  splittings for both the soybean and mammalian enzymes in Fig. 46(b) also show a larger  $^5T_{2g}$  splitting for the five-coordinate SLO-1 site than for the six-coordinate LOs, in agreement with the ground-state splittings obtained through the VTVH MCD analysis (Fig. 46(a)). The six-coordinate SLO-1 and mammalian 15-LOs ligand field calculations, which differ only by the parameters associated with the Asn→His substitution along the molecular  $z$ -axis (with the Asn–O weaker than the His–N), reproduce the  $+D$  ground-state d-orbital pattern for six-coordinate SLO-1 (Fig. 46(b), B, where the two higher-energy  $t_{2g}$  orbitals are closer in energy) and the  $-D$  pattern for the mammalian 15-LOs (Fig. 46(b), C, where the two lower-energy orbitals are closer). Although one might expect the substitution of a stronger histidine ligand for a weaker asparagine ligand would produce a strong-field  $+D$  system for the mammalian LOs and a weak-field  $-D$  system for the six-coordinate SLO-1 (see Section 3.2), the opposite is in fact observed and can be clarified by inspection of the ground state orbitals obtained from the calculations.

The ligand field calculations place the  $x$ -axis as bisecting the two oxygens in the equatorial plane (see Fig. 2(c)) due to the relatively strong ligand field of the *cis* arrangement. The results from these calculations place the  $d_{yz}$  orbital lowest in energy, followed by the  $d_{xy}$  and  $d_{xz}$  orbitals for both six-coordinate sites, as shown in the scheme below ( $d_{yz}$  and  $d_{xz}$  are the main components of these levels; “ $d_{xy}$ ” orbital is a mixture of  $d_{xy}$  and  $d_{x^2-y^2}$ ).



Because the equatorial plane contains two *cis* O and two *cis* N ligands, the  $d_{yz}$  and  $d_{xz}$  orbitals are split in energy. When the weaker asparagine ligand is replaced with the stronger histidine ligand along the *z*-axis, the energy of the  $d_{xy}$  orbital remains unchanged; however, the  $d_{xz}$  and  $d_{yz}$  orbitals both increase in energy by the same amount. This leads to the  $d_{xz}$  and  $d_{xy}$  orbitals being closer together and higher in energy than  $d_{yz}$  for SLO-1 (above, left), corresponding to a strong axial distortion along *x*. For the mammalian 15-LOs, the  $d_{yz}$  and  $d_{xy}$  orbitals are closer together and lower in energy than  $d_{xz}$  (above, right), corresponding to a weak axial distortion along *y*. Because *x* is a strong axis and *y* is a weak axis, having the primary direction along *x* produces a  $+D$  system for six-coordinate SLO-1 and having the primary direction along *y* produces a  $-D$  system for the mammalian 15-LOs. Therefore, although the six-coordinate SLO-1 and mammalian 15-LOs  $^5E_g$  excited-state splittings are very similar, the ground-state saturation magnetization and ligand field analyses demonstrate significant differences in the electronic structure of the ferrous site between the soybean and mammalian enzymes reasonably attributed to the  $Asn \rightarrow His$  ligand substitution. The MCD data thus correlate with the structures determined by X-ray crystallography and can now be used as a basis for comparison with further forms of the active site, particularly those associated with reaction intermediates and perturbed sites obtained by site directed mutagenesis which exhibit differences in reactivity.

#### 4.3. Bleomycin (BLM)

There is little direct spectroscopic information available for  $Fe(II)BLM$  as it does not exhibit an EPR signal and the magnetic Mössbauer spectra have broad unresolvable features [114]. The room temperature CD spectrum in the ligand field region of  $Fe(II)BLM$  is shown in Fig. 47(a), revealing two ferrous  $d \rightarrow d$  transitions which can be fit to Gaussian bandshapes with maxima at 9100 and 13 050  $cm^{-1}$ , giving  $\Delta^5E_g = 3950\text{ cm}^{-1}$ . This splitting is in between that expected from Section 3.2 for six- and five-coordinate geometries and is consistent with a weak-axial ligand in solution. Upon cooling to 1.6 K, the CD bands of  $Fe(II)BLM$  show a reduced splitting attributed to a limited temperature-dependent geometric distortion at the ferrous site. The MCD spectra of  $Fe(II)BLM$  shown in Fig. 47(b) exhibit two Gaussian resolved features at 9400 and 12 050  $cm^{-1}$ , giving  $\Delta^5E_g \approx 2650\text{ cm}^{-1}$ , which

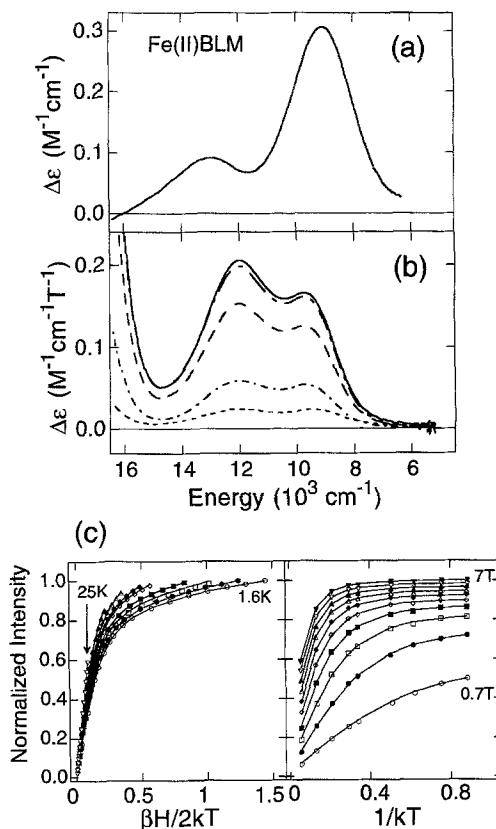


Fig. 47. Ligand field spectral region for Fe(II)BLM. (a) CD spectrum at 278 K. (b) MCD spectra at 7 T and 1.6 K (—), 5.0 K (---), 15 K (···), 50 K (— · —), and 150 K (— — —). (c) Normalized saturation magnetization data (symbols) and fits (lines) recorded at  $\sim 9400 \text{ cm}^{-1}$  plotted versus  $\beta H/2kT$  (left) and  $1/kT$  (right).

from Section 3.2 supports a six-coordinate, distorted octahedral active site geometry. VTVH MCD saturation magnetization data for Fe(II)BLM are plotted as a function of  $\beta H/2kT$  for a series of fixed temperatures in Fig. 47(c), left, and as a function of  $1/kT$  for a series of fixed fields in Fig. 47(c), right. VTVH data were collected on both  $d \rightarrow d$  transitions and produced nearly identical ground-state parameters which can be fit with the  $-D$  non-Kramers doublet model (Section 3.3.3) to:  $g_{\parallel} = 9.3$  and  $\delta = 2.4 \text{ cm}^{-1}$  with a  $B$ -term contribution of 1.5%. The fit improves slightly allowing for  $z$ -polarization; however, the polarization ratio is negligible, and the ground-state parameters remain virtually unchanged. Application of the three-level  $+D$  model (Section 3.3.4) to the Fe(II)BLM (and  $[\text{Fe(II)PMA}]^+$  in solution, vide infra) saturation magnetization data resulted in unphysical parameters.

Due to the complexity of the glycopeptide and the range of possible metal coordinating functional groups in BLM, synthetic models have been prepared in an effort to obtain insight into the active site structure [119,202–204]. The ferrous complex

of PMAH (see Fig. 4(b)) serves as a good model of Fe(II)BLM in that it reacts with dioxygen to generate an analog of activated BLM which has a nearly identical EPR spectrum and causes DNA cleavage with similar specificity [119]. In Fig. 48(a), two ligand field transitions are observed in the MCD spectra of  $[\text{Fe(II)PMA}]^+$  in solution which can be resolved into two Gaussian features at 10 090 and 12 200  $\text{cm}^{-1}$  with  $\Delta^5E_g \approx 2110 \text{ cm}^{-1}$ , indicating a six-coordinate site structure. These transitions are higher in energy and possess a smaller  $^5E_g$  splitting than those of Fe(II)BLM, implying less distortion at the ferrous center. VTVH MCD saturation magnetization data were obtained at 9900  $\text{cm}^{-1}$  (shown in Fig. 48(b)) and 11 900  $\text{cm}^{-1}$ ; the energies are lower than the true transition maxima in order to avoid a significant contribution from the tail of the charge transfer transition (vide infra) at higher energy. The best fit to the saturation data yields the ground-state parameters  $g_{\parallel} = 9.0$ ,  $\delta = 2.4 \text{ cm}^{-1}$ , and a small 0.2%  $\mathcal{B}$ -term using the  $-D$  non-Kramers doublet model (inclusion of  $z$ -polarization did not significantly improve the fit). MCD spectra were also collected for solid microcrystalline samples of  $[\text{Fe(II)PMA}]^+$  and are shown in Fig. 49(a). Three transitions are observed: a charge transfer band highest in energy (vide infra) and two ligand field bands at 5100 and 11 200  $\text{cm}^{-1}$  to give  $\Delta^5E_g = 6100 \text{ cm}^{-1}$ , which from Section 3.2 indicates a five-coordinate, square pyramidal geometry. VTVH MCD saturation magnetization data obtained at 5100  $\text{cm}^{-1}$  are shown in Fig. 49(b) and have been fit to the ground-state parameters  $g_{\parallel} = 8.5$ ,  $\delta = 3.3 \text{ cm}^{-1}$ , and

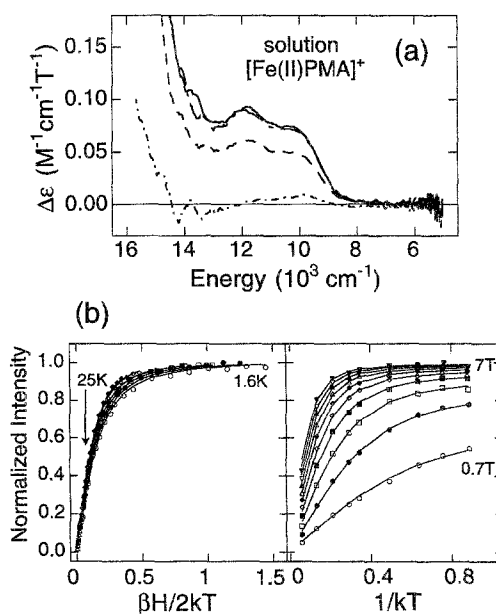


Fig. 48. Ligand field spectral region for  $[\text{Fe(II)PMA}]^+$  in solution. (a) MCD spectra obtained at 7 T and 1.6 K (—), 5.0 K (---), 15 K (— · —), and 50 K (— · — · —). (b) Normalized saturation magnetization data (symbols) and fits (lines) recorded at 9900  $\text{cm}^{-1}$  plotted versus  $\beta H/2kT$  (left) and  $1/kT$  (right).

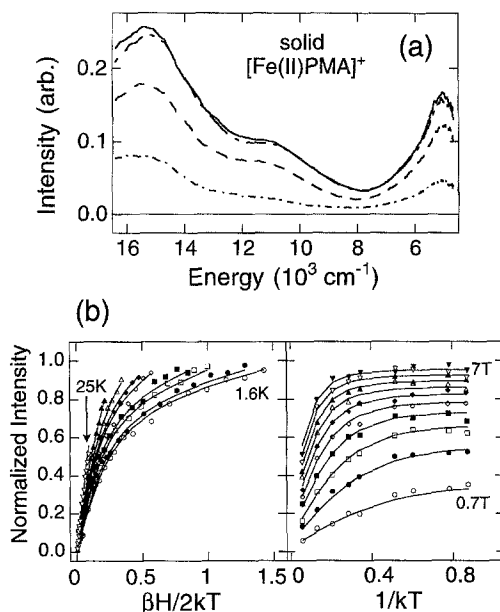


Fig. 49. Ligand field spectral region for  $[\text{Fe(II)PMA}]^+$  solid. (a) Temperature dependence of the MCD spectra at 7 T and 1.6 K (—), 5.0 K (---), 15 K (····), and 50 K (— · — · —). (b) Normalized saturation magnetization data (symbols) and fits (lines) recorded at  $\sim 5100 \text{ cm}^{-1}$  plotted versus  $\beta H/2kT$  (left) and  $1/kT$  (right).

$B_0 = 4.7\%$  using the  $-D$  non-Kramers doublet model. The value of  $g_{\parallel}$  increases slightly (to 8.9) when  $z$ -polarization is included, and a three-level  $+D$  fit gives results consistent with the  $-D$  analysis since both models indicate  $V/2\Delta$  (or  $E/D$ ) at the rhombic limit.

Molecular modeling of  $[\text{Fe(II)PMA}]^+$  has determined the model complex to be most stable with the pyrimidine, imidazole, deprotonated amide, and secondary amine coordinated equatorially, the primary amine bound axially, and a proposed solvent molecule coordinated at the open site in solution [205]. Binding of solvent to the sixth site is confirmed by the large decrease in the  $^5\text{E}_g$  excited-state splitting demonstrated by the ligand field MCD spectra going from solid to solution  $[\text{Fe(II)PMA}]^+$  in Figs. 49 and 48. The similarities in the MCD ligand field spectra and  $^5\text{E}_g$  splitting of  $\text{Fe(II)BLM}$  and  $[\text{Fe(II)PMA}]^+$  in solution suggest that the coordination spheres of the two complexes are not markedly different. A proposed solution structure of  $\text{Fe(II)BLM}$  is given in Fig. 50 which is based on the PMAH ligand set and the MCD spectral evidence that solvent coordinates at the sixth position in  $[\text{Fe(II)PMA}]^+$ .

The value of the rhombic splitting parameter obtained from the MCD saturation magnetization data of solid  $[\text{Fe(II)PMA}]^+$ ,  $\delta = 3.3 \text{ cm}^{-1}$ , is consistent with other five-coordinate species. However, the  $\delta$  value of  $2.4 \text{ cm}^{-1}$  for  $[\text{Fe(II)PMA}]^+$  in solution and  $\text{Fe(II)BLM}$  is unusually small for six-coordinate complexes of similar



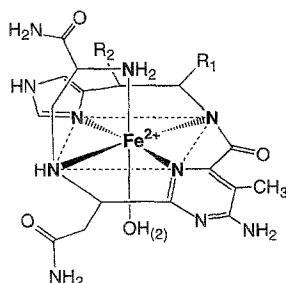


Fig. 50. Proposed solution structure of Fe(II)BLM.  $R_1$  is the linker moiety, bithiazole tail, and terminal amine;  $R_2$  is the mannose sugar moiety (see Fig. 4).

ligation (see Section 3.4.1.2). For  $[\text{Fe(II)PMA}]^+$  in solution,  $-\Delta$  increases by a small amount relative to the solid (from 900 to 950  $\text{cm}^{-1}$ ), which is opposite to the expected decrease in the  $t_{2g}$  (and  $e_g$ ) orbital splitting based on the closer to octahedral symmetry in the six-coordinate site. A decrease in the  ${}^5E_g$  excited-state splitting is, in fact, experimentally observed. Also, the ground-state analysis of the Fe(II)BLM data gave  $-\Delta \approx 800 \text{ cm}^{-1}$ , which is a fairly large axial splitting for a six-coordinate complex. These large  ${}^5T_{2g}$  ground-state splittings for Fe(II)BLM and  $[\text{Fe(II)PMA}]^+$  in solution indicate the presence of significant  $d_\pi$ -orbital interactions which differ from other non-heme ferrous sites, suggesting an unusually strong ligand–metal  $\pi$ -bond for these six-coordinate complexes.

The presence of moderately intense, low-energy metal-to-ligand charge transfer (MLCT) transitions in the low-temperature absorption, CD, and MCD spectra of  $[\text{Fe(II)PMA}]^+$  and Fe(II)BLM presents an important deviation from other non-heme iron centers and reflects the high covalency of the ferrous state associated with the  $\pi$ -bond. The absorption, CD, and MCD spectra of Fe(II)BLM in the charge transfer region are Gaussian resolved in Fig. 51. Iterative fitting of the spectra requires five bands at  $\sim 18\,100 \text{ cm}^{-1}$ ,  $\sim 20\,350 \text{ cm}^{-1}$ ,  $\sim 22\,690 \text{ cm}^{-1}$ ,  $\sim 26\,040 \text{ cm}^{-1}$ , and  $\sim 29\,000 \text{ cm}^{-1}$ . The transitions in the low-temperature absorption and MCD spectra of  $[\text{Fe(II)PMA}]^+$  in solution shown in Fig. 52(a,b) do not correlate with one another as clearly as those of Fe(II)BLM do in Fig. 51. Results of a simultaneous fitting of the five lowest-energy transitions gives peak maxima at  $\sim 13\,120 \text{ cm}^{-1}$ ,  $\sim 14\,430 \text{ cm}^{-1}$ ,  $\sim 15\,650 \text{ cm}^{-1}$ ,  $\sim 17\,960 \text{ cm}^{-1}$ , and  $\sim 20\,265 \text{ cm}^{-1}$ . The two lowest-energy transitions observed in the absorption spectrum have little MCD intensity. The absorption spectrum of solid  $[\text{Fe(II)PMA}]^+$  (not shown due to the effects of scattering on the baseline) exhibits features similar to those of  $[\text{Fe(II)PMA}]^+$  in solution, but the bands are shifted to lower energy. The lowest-energy envelope of the low-temperature MCD spectrum of solid  $[\text{Fe(II)PMA}]^+$  in Fig. 52(c) is also red-shifted and can be individually fit to three intense bands at  $\sim 14\,565 \text{ cm}^{-1}$ ,  $\sim 16\,410 \text{ cm}^{-1}$ , and  $\sim 18\,350 \text{ cm}^{-1}$ . These are assigned as having the same origin as the three transitions in the solution  $[\text{Fe(II)PMA}]^+$  MCD spectrum.

The low-energy charge transfer transitions of Fe(II)BLM and  $[\text{Fe(II)PMA}]^+$  are

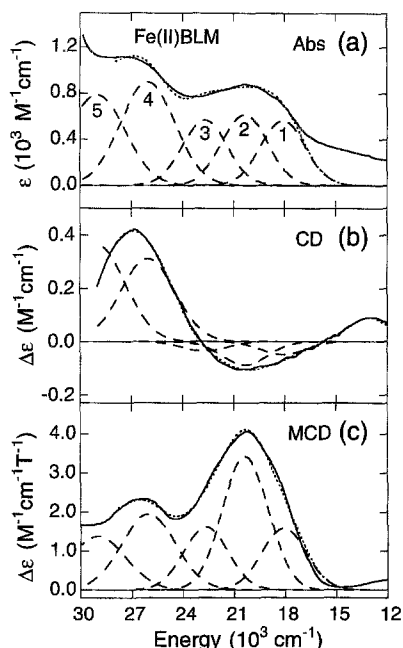
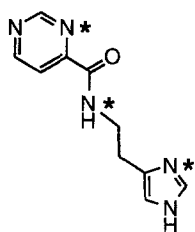
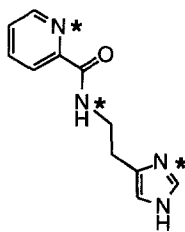


Fig. 51. Gaussian resolution of the Fe(II)BLM charge transfer transitions observed in the absorption, CD, and MCD spectra. (a) Absorption spectrum at 8 K. (b) CD spectrum at 278 K. (c) MCD spectrum at 5 K and 6 T. The experimental spectra (—) were simultaneously fit to individual Gaussian bandshapes (---) and plotted against the resultant sum (.....).

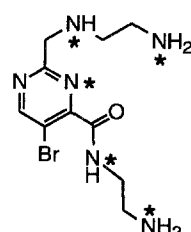
assigned by comparison to the absorption spectra of the structurally perturbed analogs  $[\text{Fe(II)(Prpep)}_2]$ ,  $[\text{Fe(II)(Pyep)}_2]$ , and  $[\text{Fe(II)PMD}]^+$ , shown below.



$[\text{Fe(II)(Prpep)}_2]$



$[\text{Fe(II)(Pyep)}_2]$



$[\text{Fe(II)PMD}]^+$

$[\text{Fe(II)(Prpep)}_2]$  and  $[\text{Fe(II)(Pyep)}_2]$  are *bis*-complexes of a tridentate ligand with the same histidine and deprotonated amide functionalities and differ only in the exchange of pyrimidine with pyridine, respectively.  $[\text{Fe(II)PMA}]^+$  and  $[\text{Fe(II)PMD}]^+$  are 1:1 metal:ligand complexes where the PMDH ligand has the same structure as PMAH (Fig. 4) except for replacement of the imidazole with an  $\text{NH}_2$  group. From a comparison of the absorption spectra in the charge transfer region, shown in Fig. 53,  $[\text{Fe(II)PMA}]^+$  and  $[\text{Fe(II)PMD}]^+$  have the same low-

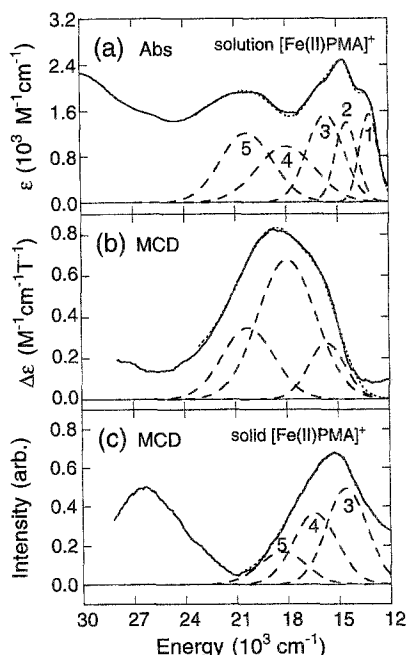


Fig. 52. Gaussian resolution of  $[\text{Fe}(\text{II})\text{PMA}]^+$  solid and solution charge transfer transitions observed in the absorption and MCD spectra. (a) Absorption spectrum of the solution at 8 K. (b) MCD spectrum of the solution at 5 K and 6 T. (c) MCD spectrum of the solid at 5 K and 6 T. The experimental spectra (—) were simultaneously fit to individual Gaussian bandshapes (---) and plotted against the resultant sum (.....).

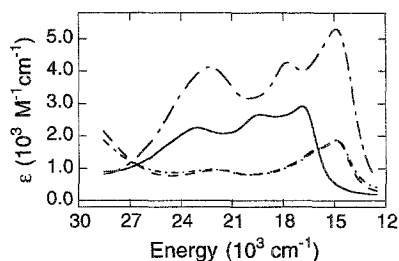


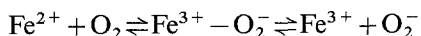
Fig. 53. Room temperature absorption spectra of  $[\text{Fe}(\text{II})\text{PMA}]^+$  and related model complexes. Absorption spectra of  $[\text{Fe}(\text{II})(\text{Pyep})_2]$  (—),  $[\text{Fe}(\text{II})(\text{Prpep})_2]$  (---),  $[\text{Fe}(\text{II})\text{PMA}]^+$  (.....), and  $[\text{Fe}(\text{II})\text{PMD}]^+$  (- · - · -) in methanol (the spectra of  $[\text{Fe}(\text{II})\text{PMA}]^+$  and  $[\text{Fe}(\text{II})\text{PMD}]^+$  superimpose).

energy bands, arguing against histidine contributions to these transitions, while the bands in  $[\text{Fe}(\text{II})(\text{Pyep})_2]$  are shifted by 0.20 eV to higher energy relative to  $[\text{Fe}(\text{II})(\text{Prpep})_2]$  consistent with the increase in the redox potential of 0.21 eV [206]. These comparisons demonstrate that the low-energy spectral features of  $[\text{Fe}(\text{II})\text{PMA}]^+$  and  $\text{Fe}(\text{II})\text{BLM}$  in Figs. 52 and 51 are composed of  $\text{Fe}(\text{II}) \rightarrow \text{pyrimidine}$  charge transfer transitions. The energies and intensities of these

transitions determine the degree of metal–ligand  $\pi$ -backbonding which decreases along the series  $[\text{Fe(II)PMA}]^+$  solid  $> [\text{Fe(II)PMA}]^+$  in solution  $> \text{Fe(II)BLM}$  and is influenced by pyrimidine ring substituents and change in coordination number. The difference in the charge transfer energies directly results from the electron donating ( $\text{NH}_2$  group in BLM) or withdrawing (Br atom in PMAH) nature of the substituents on the pyrimidine ring as they either raise or lower the energy of the  $\pi^*$ -orbitals [207,208]. Also, in contrast to the effects expected based on repulsive interactions, as the coordination number decreases, metal–ligand bonding becomes more covalent, which raises the energy of the predominantly antibonding donor orbital of the metal and induces a shift to lower energy of the charge transfer transitions of the five- versus six-coordinate species.

To account for the presence of at least five  $d_\pi \rightarrow \pi^*$  MLCT transitions in the absorption, CD, and MCD spectra of  $\text{Fe(II)BLM}$  and  $[\text{Fe(II)PMA}]^+$  (Figs. 51 and 52), specific iron and pyrimidine molecular orbital interactions must be considered. The greater the iron  $d_\pi$ - and pyrimidine  $\pi^*$ -orbital overlap, the greater the intensity of the CT transition. As shown in Fig. 54, the two lowest-energy pyrimidine  $\pi^*$ -orbitals,  $3b_1$  and  $2a_2$ , are split in energy by  $\sim 2000\text{--}3000\text{ cm}^{-1}$  [209–213] and are of the appropriate symmetry to overlap with the iron  $d_{yz}$  orbital (the weak molecular  $z$ -axis is defined as the primary amine–solvent direction and the equatorial pyrimidine ligand as the  $y$ -axis). The  $d_{yz}$  orbital is lowest in energy as shown in the initial state bonding diagram in Fig. 54 due to its strong  $\pi$ -bonding interaction with the pyrimidine  $\pi^*$ -levels, and should thus contain the extra electron of the  $d^6$  configuration. Its transition energy to the pyrimidine  $\pi^*$ -orbital will go down, however, relative to the other  $d$ -orbitals due to loss of electron repulsion in the transition, as shown in the final state bonding diagram in Fig. 54. In addition, the  $d_{x^2-y^2}$  and  $d_{z^2}$  orbitals can undergo configuration interaction with the  $d_{yz}$  orbital which gives some intensity to the charge transfer transitions from these  $d$ -orbitals to the pyrimidine  $\pi^*$ -orbitals. Although the MLCT energies and intensities in Figs. 51 and 52 show agreement with the qualitative bonding model illustrated in Fig. 54, rigorous assignment of these transitions requires quantitation of final state relaxation effects and overlap through transition state electronic structure calculations.

These MLCT transitions in  $\text{Fe(II)BLM}$  indicate the presence of significant  $\pi$ -backbonding which mediates the electron density localized on the ferrous center and should contribute to the chemistry and unusual oxygen reactivity of  $\text{Fe(II)BLM}$  relative to other non-heme ferrous sites. The steric constraints of the BLM ligand framework coupled with the labile coordination site occupied by the solvent molecule suggest that oxygen binding to the ferrous center occurs via a dissociative mechanism. Backbonding to the pyrimidine ligand decreases the extent of charge transfer to the oxygen which shifts the equilibrium shown below to the left, making  $\text{FeBLM}$  less likely to dissociate superoxide.



This reduced charge transfer to the bound superoxide also enhances the propensity for further reduction to form the low-spin  $\text{Fe(III)}$ -peroxide site of activated BLM [114–116]. Despite generally being considered a non-heme iron system due to the

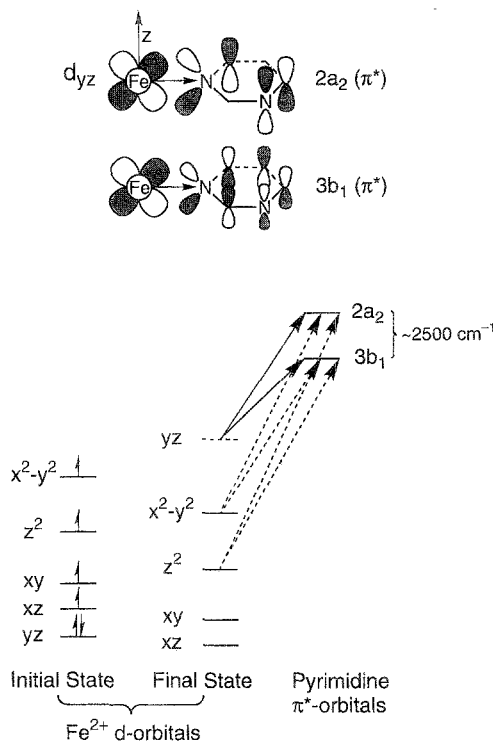


Fig. 54. Qualitative Fe–pyrimidine bonding description and the relative energies and intensities of the resulting metal-to-ligand charge transfer transitions. Molecular coordinate scheme and nodal pattern for the Fe<sup>2+</sup>  $d_{yz}$  orbital  $\pi$ -bonding to the pyrimidine  $2a_2$  and  $3b_1$  ( $\pi^*$ ) orbitals (top). The different lobe sizes indicate that the  $2a_2$  ( $\pi^*$ ) pyrimidine orbital has a larger coefficient of mixing relative to the corresponding  $3b_1$  ( $\pi^*$ ) orbital. Molecular orbital energy level diagram (bottom) for Fe(II)BLM and [Fe(II)PMA]<sup>+</sup> depicting the initial and final state Fe<sup>2+</sup> d-orbital energies prior to and upon metal-to-ligand charge transfer to the pyrimidine  $2a_2$  and  $3b_1$  ( $\pi^*$ ) orbitals which are split by 2000–3000 cm<sup>−1</sup>. The final state order includes the loss of electron repulsion energy on the  $d_{yz}$  orbital. The predicted metal-to-ligand charge transfer transitions based on overlap and symmetry considerations are identified by solid arrows for intense transitions and dashed arrows for weaker transitions.

absence of an extensive delocalized  $\pi$ -network, the existence of moderately intense, low-energy MLCT transitions identifies BLM as an important link bridging the chemistry of non-heme and heme active sites.

## 5. Concluding remarks

The non-heme ferrous sites have been the least spectroscopically accessible; however, the above examples have demonstrated that the combination of CD, MCD, and VTVH MCD spectroscopies provide an effective spectroscopic approach for the study of these sites. The excited-state splittings of the  $e_g$  orbitals can be observed directly through NIR CD and MCD spectroscopies (Section 3.1). Ligand field

calculations (Section 3.2) provide the relation between these  $^5\text{E}$  splittings and the coordination geometry at the ferrous center: six-coordinate complexes show two bands in the region of  $10\,000\text{ cm}^{-1}$  which are split by  $\sim 2000\text{ cm}^{-1}$ , five-coordinate square pyramidal sites exhibit two bands at  $>10\,000$  and  $>5000\text{ cm}^{-1}$ , while trigonal bipyramidal sites exhibit one band at  $<10\,000\text{ cm}^{-1}$  and another at  $<5000\text{ cm}^{-1}$ , and four-coordinate tetrahedral sites show one to two bands at  $4000\text{--}7000\text{ cm}^{-1}$ . The  $S=2$  ground state of high-spin ferrous complexes undergoes axial ZFS into the  $M_S = \pm 2, \pm 1, 0$  components, separated by the energies  $3D$  and  $D$ , respectively. For  $D < 0$ , the doubly degenerate  $M_S = \pm 2$  level is lowest and is further rhombically split ( $\delta$ ) even in the absence of a magnetic field since this ground state is a non-Kramers doublet. Additionally, the ground-state wave functions are dependent on the magnitude of the magnetic field relative to this ZFS. The VTVH MCD behavior of each of the ligand field excited states produces an unusual set of saturation magnetization curves which are explained by this non-Kramers doublet behavior (Section 3.3.3). A fit to these data, including the effects of  $z$ -polarization, linear  $\mathcal{B}$ -terms, and the population of low-lying excited states, provides the spin Hamiltonian parameters for the ferrous ground state even in the absence of an EPR signal (Sections 3.3.1–3.3.3). For  $D > 0$ , the non-degenerate  $M_S = 0$  state is lowest in energy and the effects of off-axis Zeeman terms and  $z$ -polarized electronic transitions must be included in order to describe the resulting saturation magnetization behavior (Section 3.3.4). The spin Hamiltonian parameters are further interpreted in terms of the ligand field splitting of the ground state  $t_{2g}$  orbitals (Section 3.4). For example, the ground-state parameters  $\delta$  and  $g_{\parallel}$  indicate the  $t_{2g}$  d-orbital splittings  $-\Delta$  ( $E_{xz,yz} - E_{xy}$ ) and  $V$  ( $E_{xz} - E_{yz}$ ) for the weak-axial octahedral and square pyramidal cases. Additionally, a large value of  $\delta$  corresponds to a small  $^5\text{T}_{2g}$  splitting, indicating a six-coordinate structure, while a small  $\delta$  requires a large  $^5\text{T}_{2g}$  splitting and a five-coordinate ferrous site. Thus, these spectroscopic studies provide experimental values for the d-orbital splittings of the ferrous center which are a direct probe of the active site geometric and electronic structure.

This review illustrates the utility of MCD spectroscopy as an effective probe of mononuclear non-heme ferrous enzymes for which other spectroscopic techniques have proven less rewarding. From Fig. 1, it is evident that there are a wide variety of enzymes for which the ferrous oxidation state is catalytically relevant in oxygen reactivity. Therefore, it is crucial to have developed a successful method for the investigation of these active sites. The experiments on the plant and mammalian lipoxygenases, which have been used to obtain detailed geometric descriptions of the native active sites (Section 4.2), will now be extended to investigate the structures of oxygen intermediates and of site-perturbed mutants which exhibit differences in reactivity relative to the native forms. In addition, these studies will be combined with SCF-X $\alpha$ -SW electronic structure calculations which will be used to probe the electronic contributions to reactivity. The studies of Fe(II)BLM have defined the geometric and electronic structure of the ferrous center as it relates to the unusual chemistry and reactivity observed for this system (Section 4.3). Due to its clinical application as an anticancer agent, it is of interest to extend the studies of bleomycin to include the interactions of Fe(II)BLM with DNA to probe substrate effects on

the structure of the iron site. Similar enzyme–substrate interactions will be investigated for clavamate synthase, which performs different chemistry (oxidative ring closure, hydroxylation, or desaturation) depending on the substrate, and also will be extended to probe the interaction of the  $\text{Fe}^{2+}$  site with its  $\alpha$ -KG cofactor. An analogous investigation on phenylalanine hydroxylase is required to probe the interactions of the ferrous active site with its pterin cofactor and substrate. Further application of this methodology to the mononuclear non-heme ferrous enzymes illustrated in Fig. 1 will be used to obtain molecular-level insight into the catalytic mechanisms and to understand the differences in the active site geometric and electronic structures which relate to differences in oxygen and substrate reactivity.

## Acknowledgments

This work was supported by the National Institute of Health (GM 40392). E.I.S. expresses his sincere appreciation to all the students and collaborators listed as coauthors in the literature cited for their commitment and contributions to this research.

## References

- [1] P.M. Harrison and T.H. Lilley, in T.M. Loehr (ed.), *Iron Carriers and Iron Proteins*, VCH, New York, 1989, Vol. 5, p. 123.
- [2] E.C. Theil, in A. Meister (ed.), *Advances in Enzymology*, John Wiley, New York, 1990, Vol. 63, p. 421.
- [3] D.C. Harris and P. Aisen, in T.M. Loehr (ed.), *Iron Carriers and Iron Proteins*, VCH, New York, 1989, Vol. 5, p. 239.
- [4] T.G. Spiro (ed.), *Iron–Sulfur Proteins*, John Wiley, New York, 1982, Vol. 4.
- [5] G.L. Eichhorn and L.G. Marzilli (eds.), *Heme Proteins*, Elsevier, New York, 1988, Vol. 7.
- [6] D. Mansuy and P. Battioni, in J. Reedijk (ed.), *Bioinorganic Catalysis*, Marcel Dekker, New York, 1993, p. 395.
- [7] P.R. Ortiz de Montellano (ed.), *Cytochrome P-450: Structure, Mechanism, and Biochemistry*, Plenum Press, New York, 1986.
- [8] G.T. Babcock and M. Wikström, *Nature*, 356 (1992) 301.
- [9] B.G. Malmström, *Chem. Rev.*, 90 (1990) 1247.
- [10] J. Sanders-Loehr, in T.M. Loehr (ed.), *Iron Carriers and Iron Proteins*, VCH, New York, 1989, Vol. 5, p. 373.
- [11] C.A. Brown, G.J. Remar, R.L. Musselman and E.I. Solomon, *Inorg. Chem.*, 34 (1995) 688.
- [12] E.I. Solomon and Y. Zhang, *Acc. Chem. Res.*, 25 (1992) 343.
- [13] L. Que, Jr., in J. Reedijk (ed.), *Bioinorganic Catalysis*, Marcel Dekker, New York, 1993, p. 347.
- [14] A.L. Feig and S.J. Lippard, *Chem. Rev.*, 94 (1994) 759.
- [15] B.L. Stoddard, P.L. Howell, D. Ringe and G.A. Petsko, *Biochemistry*, 29 (1990) 8885.
- [16] J.E. Baldwin and M. Bradley, *Chem. Rev.*, 90 (1990) 1079.
- [17] A.G. Katopodis, K. Wimalasena, J. Lee and S.W. May, *J. Am. Chem. Soc.*, 106 (1984) 7928.
- [18] L. Que, Jr., in T.M. Loehr (ed.), *Iron Carriers and Iron Proteins*, VCH, New York, 1989, Vol. 5, p. 467.
- [19] J.D. Lipscomb and A.M. Orville, in H. Sigel and A. Sigel (eds.), *Metal Ions in Biological Systems*, Marcel Dekker, New York, 1992, Vol. 28, p. 243.
- [20] C.J. Batie, E. LaHaie and D.P. Ballou, *J. Biol. Chem.*, 262 (1987) 1510.

- [21] R. Shiman, in R.L. Blakley and S.J. Benkovic (eds.), *Folates and Pterins: Chemistry and Biochemistry of Pterins*, John Wiley, New York, 1985, Vol. 2, p. 179.
- [22] S.P. Salowe, E.N. Marsh and C.A. Townsend, *Biochemistry*, 29 (1990) 6499.
- [23] B. Samuelsson, S.-E. Dahlén, J.Å. Lindgren, C.A. Rouzer and C.N. Serhan, *Science*, 237 (1987) 1171.
- [24] J. Stubbe and J.W. Kozarich, *Chem. Rev.*, 87 (1987) 1107.
- [25] D.H. Petering, R.W. Byrnes and W.E. Antholine, *Chem.-Biol. Interact.*, 73 (1990) 133.
- [26] P.A. Mabrouk, A.M. Orville, J.D. Lipscomb and E.I. Solomon, *J. Am. Chem. Soc.*, 113 (1991) 4053.
- [27] E.I. Solomon, M.L. Kirk, D.R. Gamelin and S. Pulver, *Methods Enzymol.*, 246 (1995) 71.
- [28] W.C. Stallings, C. Bull, J.A. Fee, M.S. Lah and M.L. Ludwig, in J.G. Scandalios (ed.), *Molecular Biology of Free Radical Scavenging Systems*, Cold Spring Harbor Laboratory Press, New York, 1992, p. 193.
- [29] W. Stallings, C. Bull, K.A. Patridge, T.B. Powers, J.A. Fee, M.L. Ludwig, D. Ringe and G.A. Petsko, in W. Bors, M. Saran and D. Tait (eds.), *Oxygen Radicals in Chemistry and Biology*, Walter de Gruyter, Berlin, 1984, p. 779.
- [30] D. Ringe, G.A. Petsko, F. Yamakura, K. Suzuki and D. Ohmori, *Proc. Natl. Acad. Sci. USA*, 80 (1983) 3879.
- [31] W.C. Stallings, T.B. Powers, K.A. Patridge, J.A. Fee and M.L. Ludwig, *Proc. Natl. Acad. Sci. USA*, 80 (1983) 3884.
- [32] W.C. Stallings, A.L. Metzger, K.A. Patridge, J.A. Fee and M.L. Ludwig, *Free Rad. Res. Commun.*, 12–13 (1991) 259.
- [33] J.W. Whittaker and E.I. Solomon, *J. Am. Chem. Soc.*, 110 (1988) 5329.
- [34] J.E. Baldwin, J.M. Blackburn, J.D. Sutherland and M.C. Wright, *Tetrahedron*, 47 (1991) 5991.
- [35] J.E. Baldwin, G.P. Lynch and C.J. Schofield, *J. Chem. Soc. Chem. Commun.*, (1991) 736.
- [36] J.E. Baldwin, M. Bradley, R.M. Adlington, W.J. Norris and N.J. Turner, *Tetrahedron*, 47 (1991) 457.
- [37] F. Jiang, J. Peisach, L.-J. Ming, L. Que, Jr. and V.J. Chen, *Biochemistry*, 30 (1991) 11437.
- [38] L.-J. Ming, L. Que, Jr., A. Kriauciunas, C.A. Frolik and V.J. Chen, *Inorg. Chem.*, 29 (1990) 1111.
- [39] J.E. Baldwin and E. Abraham, *Nat. Prod. Rep.*, 5 (1988) 129.
- [40] J.E. Baldwin, R.M. Adlington, D.G. Marquess, A.R. Pitt and A.T. Russell, *J. Chem. Soc. Chem. Commun.*, (1991) 856.
- [41] V.J. Chen, A.M. Orville, M.R. Harpel, C.A. Frolik, K.K. Surerus, E. Münck and J.D. Lipscomb, *J. Biol. Chem.*, 264 (1989) 21677.
- [42] L.-J. Ming, L. Que, Jr., A. Kriauciunas, C.A. Frolik and V.J. Chen, *Biochemistry*, 30 (1991) 11653.
- [43] R.A. Scott, S. Wang, M.K. Eidsness, A. Kriauciunas, C.A. Frolik and V.J. Chen, *Biochemistry*, 31 (1992) 4596.
- [44] C.R. Randall, Y. Zang, A.E. True, L. Que, Jr., J.M. Charnock, C.D. Garner, Y. Fujishima, C.J. Schofield and J.E. Baldwin, *Biochemistry*, 32 (1993) 6664.
- [45] A.M. Orville, V.J. Chen, A. Kriauciunas, M.R. Harpel, B.G. Fox, E. Münck and J.D. Lipscomb, *Biochemistry*, 31 (1992) 4602.
- [46] J.E. Baldwin, R.M. Adlington, M. Bradley, W.J. Norris, N.J. Turner and A. Yoshida, *J. Chem. Soc. Chem. Commun.*, (1988) 1125.
- [47] J.E. Baldwin, G.P. Lynch and C.J. Schofield, *Tetrahedron*, 48 (1992) 9085.
- [48] R.T. Ruettinger, G.R. Griffith and M.J. Coon, *Arch. Biochem. Biophys.*, 183 (1977) 528.
- [49] E.J. McKenna and M.J. Coon, *J. Biol. Chem.*, 245 (1970) 3882.
- [50] S.W. May, S.L. Gordon and M.S. Steltenkamp, *J. Am. Chem. Soc.*, 99 (1977) 2017.
- [51] D.A. Bender, *Amino Acid Metabolism*, 2nd edn., John Wiley, New York, 1985.
- [52] D.M. Arciero, A.M. Orville and J.D. Lipscomb, *J. Biol. Chem.*, 260 (1985) 14035.
- [53] D.H. Ohlendorf, J.D. Lipscomb and P.C. Weber, *Nature*, 336 (1988) 403.
- [54] C.A. Earhart, R. Radhakrishnan, A.M. Orville, J.D. Lipscomb and D.H. Ohlendorf, *J. Mol. Biol.*, 236 (1994) 374.
- [55] J.D. Lipscomb, personal communication, 1994.
- [56] H.G. Jang, D.D. Cox and L. Que, Jr., *J. Am. Chem. Soc.*, 113 (1991) 9200.
- [57] T. Funabiki, T. Konishi, S. Kobayashi, A. Mizoguchi, M. Takano and S. Yoshida, *Chem. Lett.*, (1987) 719.
- [58] S. Han, L. Eltis and J. Bolin, personal communication, 1994.



- [59] S.E. Crutcher and P.J. Geary, *Biochem. J.*, 177 (1979) 393.
- [60] M. Yamaguchi and H. Fujisawa, *J. Biol. Chem.*, 255 (1980) 5058.
- [61] B.D. Ensley and D.T. Gibson, *J. Bacteriol.*, 155 (1983) 505.
- [62] K. Sauber, C. Fröhner, G. Rosenberg, J. Eberspächer and F. Lingens, *Eur. J. Biochem.*, 74 (1977) 89.
- [63] D.T. Gibson, W.-K. Yeh, T.-N. Liu and V. Subramanian, in M. Nozaki, S. Yamamoto, Y. Ishimura, M.J. Coon, L. Ernster and R.W. Estabrook (eds.), *Oxygenases and Oxygen Metabolism*, Academic Press, New York, 1982, p. 51.
- [64] C.J. Batie, D.P. Ballou and C.C. Correll, *Chem. Biochem. Flavoenzymes*, 3 (1992) 543.
- [65] A. Markus, D. Krekel and F. Lingens, *J. Biol. Chem.*, 261 (1986) 12883.
- [66] F. Brunel and J. Davison, *J. Bacteriol.*, 170 (1988) 4924.
- [67] F.-H. Bernhardt, E. Heymann and P.S. Traylor, *Eur. J. Biochem.*, 92 (1978) 209.
- [68] D. Kuila, J.A. Fee, J.R. Schoonover, W.H. Woodruff, C.J. Batie and D.P. Ballou, *J. Am. Chem. Soc.*, 109 (1987) 1559.
- [69] D. Kuila, J.R. Schoonover, R.B. Dyer, C.J. Batie, D.P. Ballou, J.A. Fee and W.H. Woodruff, *Biochim. Biophys. Acta*, 1140 (1992) 175.
- [70] R.J. Gurbie, C.J. Batie, M. Sivaraja, A.E. True, J.A. Fee, B.M. Hoffman and D.P. Ballou, *Biochemistry*, 28 (1989) 4861.
- [71] J.F. Cline, B.M. Hoffman, W.B. Mims, E. LaHaie, D.P. Ballou and J.A. Fee, *J. Biol. Chem.*, 260 (1985) 3251.
- [72] H.-T. Tsang, C.J. Batie, D.P. Ballou and J.E. Penner-Hahn, *Biochemistry*, 28 (1989) 7233.
- [73] J.E. Penner-Hahn, *Basic Life Sci.*, 51 (Synchr. Radiat. Struct. Biology) (1989) 177.
- [74] G.T. Gassner, D.P. Ballou, G.A. Landrum and J.W. Whittaker, *Biochemistry*, 32 (1993) 4820.
- [75] E.G. Pavel, L.J. Martins, W.R. Ellis, Jr. and E.I. Solomon, *Chem. Biol.*, 1 (1994) 173.
- [76] S. Kaufman, in B.W. Agranoff and M.H. Aprison (eds.), *Advances in Neurochemistry*, Plenum Press, New York, 1976, Vol. 2, p. 1.
- [77] T.A. Dix, G.E. Bollag, P.L. Domanico and S.J. Benkovic, *Biochemistry*, 24 (1985) 2955.
- [78] J. McCracken, S. Pember, S.J. Benkovic, J.J. Villafranca, R.J. Miller and J. Peisach, *J. Am. Chem. Soc.*, 110 (1988) 1069.
- [79] J. Perkinson, S. Brodie, K. Yoon, K. Mosny, P.J. Carroll, T.V. Morgan and S.J.N. Burgmayer, *Inorg. Chem.*, 30 (1991) 719.
- [80] A. Martínez, C. Abeygunawardana, J. Haavik, T. Flatmark and A.S. Mildvan, *Biochemistry*, 32 (1993) 6381.
- [81] R.T. Carr and S.J. Benkovic, *Biochemistry*, 32 (1993) 14132.
- [82] L.M. Bloom, S.J. Benkovic and B.J. Gaffney, *Biochemistry*, 25 (1986) 4204.
- [83] D.E. Wallick, L.M. Bloom, B.J. Gaffney and S.J. Benkovic, *Biochemistry*, 23 (1984) 1295.
- [84] J.P. Caradonna, personal communication, 1994.
- [85] K.I. Kivirikko and R. Myllylä, in R.B. Freedman and H.C. Hawkins (eds.), *The Enzymology of Post-Translational Modification of Proteins*, Academic Press, London, 1980, Vol. 1, p. 53.
- [86] L.D. Thornburg, M.-T. Lai, J.S. Wishnok and J. Stubbe, *Biochemistry*, 32 (1993) 14023.
- [87] S. Lindstedt, B. Odelhög and M. Rundgren, *Biochemistry*, 16 (1977) 3369.
- [88] J.E. Baldwin, M.D. Lloyd, B. Wha-Son, C.J. Schofield, S.W. Elson, K.H. Baggeley and N.H. Nicholson, *J. Chem. Soc. Chem. Commun.*, (1993) 500.
- [89] S.P. Salowe, W.J. Krol, D. Iwata-Reuyl and C.A. Townsend, *Biochemistry*, 30 (1991) 2281.
- [90] Y.-M. Chiou and L. Que, Jr., *J. Am. Chem. Soc.*, 114 (1992) 7567.
- [91] B. Siegel, *Bioorg. Chem.*, 8 (1979) 219.
- [92] H. Kühn, J. Barnett, D. Grunberger, P. Baecker, J. Chow, B. Nguyen, H. Bursztyn-Pettegrew, H. Chan and E. Sigal, *Biochim. Biophys. Acta*, 1169 (1993) 80.
- [93] M.C. Feiters, R. Aasa, B.G. Malmström, S. Slappendel, G.A. Veldink and J.F.G. Vliegthart, *Biochim. Biophys. Acta*, 831 (1985) 302.
- [94] E.J. Corey and R. Nagata, *J. Am. Chem. Soc.*, 109 (1987) 8107.
- [95] G.A. Veldink and J.F.G. Vliegthart, *Adv. Inorg. Biochem.*, 6 (1984) 139.
- [96] M.J. Nelson, R.A. Cowling and S.P. Seitz, *Biochemistry*, 33 (1994) 4966.
- [97] M.J. Nelson, D.G. Batt, J.S. Thompson and S.W. Wright, *J. Biol. Chem.*, 266 (1991) 8225.

- [98] W.R. Dunham, R.T. Carroll, J.F. Thompson, R.H. Sands and M.O. Funk, Jr., *Eur. J. Biochem.*, 190 (1990) 611.
- [99] L.M. Van der Heijdt, M.C. Feiters, S. Navaratnam, H.-F. Nolting, C. Hermes, G.A. Veldink and J.F.G. Vliegthart, *Eur. J. Biochem.*, 207 (1992) 793.
- [100] J.C. Boyington, B.J. Gaffney and L.M. Amzel, *Science*, 260 (1993) 1482.
- [101] W. Minor, J. Steczko, J.T. Bolin, Z. Otwinowski and B. Axelrod, *Biochemistry*, 32 (1993) 6320.
- [102] M.J. Nelson, *J. Am. Chem. Soc.*, 110 (1988) 2985.
- [103] M.A. Pavlosky, Y. Zhang, T.E. Westre, Q.-F. Gan, E.G. Pavel, C. Campochiaro, B. Hedman, K.O. Hodgson and E.I. Solomon, *J. Am. Chem. Soc.*, 117 (1995) 4316.
- [104] S.K. Carter, S.T. Crooke and H. Umezawa (eds.), *Bleomycin: Current Status and New Developments*, Academic Press, New York, 1978.
- [105] J.C. Dabrowiak, in H. Sigel (ed.), *Metal Ions in Biological Systems*, Marcel Dekker, New York, 1980, Vol. 11, p. 305.
- [106] Y. Iitaka, H. Nakamura, T. Nakatani, Y. Muraoka, A. Fujii, T. Takita and H. Umezawa, *J. Antibiot.*, 31 (1978) 1070.
- [107] M.A.J. Akkerman, E.W. J.F. Neijman, S.S. Wijmenga, C.W. Hilbers and W. Bermel, *J. Am. Chem. Soc.*, 112 (1990) 7462.
- [108] Y. Sugiura, *J. Am. Chem. Soc.*, 102 (1980) 5208.
- [109] N. Hamamichi, A. Natrajan and S.M. Hecht, *J. Am. Chem. Soc.*, 114 (1992) 6278.
- [110] T.T. Sakai, J.M. Riordan and J.D. Glickson, *Biochim. Biophys. Acta*, 758 (1983) 176.
- [111] L.F. Povirk, M. Hogan and N. Dattagupta, *Biochemistry*, 18 (1979) 96.
- [112] R.M. Burger, J. Peisach and S.B. Horwitz, *J. Biol. Chem.*, 256 (1981) 11636.
- [113] R.M. Burger, S.B. Horwitz, J. Peisach and J.B. Wittenberg, *J. Biol. Chem.*, 254 (1979) 12299.
- [114] R.M. Burger, T.A. Kent, S.B. Horwitz, E. Münck and J. Peisach, *J. Biol. Chem.*, 258 (1983) 1559.
- [115] J.W. Sam, X.-J. Tang and J. Peisach, *J. Am. Chem. Soc.*, 116 (1994) 5250.
- [116] T.E. Westre, K.E. Loeb, J.M. Zaleski, B. Hedman, K.O. Hodgson and E.I. Solomon, *J. Am. Chem. Soc.*, 117 (1995) 1309.
- [117] G.H. McCall, L.E. Rabow, G.W. Ashley, S.H. Wu, J.W. Kozarich and J. Stubbe, *J. Am. Chem. Soc.*, 114 (1992) 4958.
- [118] J.H. Dawson, *Science*, 240 (1988) 433.
- [119] R.J. Guajardo, S.E. Hudson, S.J. Brown and P.K. Mascharak, *J. Am. Chem. Soc.*, 115 (1993) 7971.
- [120] M. Otsuka, T. Masuda, A. Haupt, M. Ohno, T. Shiraki, Y. Sugiura and K. Maeda, *J. Am. Chem. Soc.*, 112 (1990) 838.
- [121] K.E. Loeb, J.M. Zaleski, T.E. Westre, R.J. Guajardo, P.K. Mascharak, B. Hedman, K.O. Hodgson and E.I. Solomon, *J. Am. Chem. Soc.*, 117 (1995) 4545.
- [122] S. Sugano, Y. Tanabe and H. Kamimura, *Multiplets of Transition-Metal Ions in Crystals*, Academic Press, New York, 1970.
- [123] A. Abragam and B. Bleaney, *Electron Paramagnetic Resonance of Transition Ions*, Dover Publications, New York, 1986.
- [124] O. Kahn, *Molecular Magnetism*, VCH Publishers, New York, 1993.
- [125] P. Güttlich, R. Link and A. Trautwein, *Mössbauer Spectroscopy and Transition Metal Chemistry*, Springer-Verlag, Berlin, 1978.
- [126] R.J.H. Clark and T.J. Dines, *Adv. Infrared Raman Spectrosc.*, 9 (1982) 282.
- [127] I.W. Johnstone, D.J. Lockwood and G. Mischler, *J. Phys. C: Solid State Phys.*, 11 (1978) 2147.
- [128] V.P. Gnezdilov, V.V. Eremenko, A.V. Peschanskii and V.I. Fomin, *Sov. J. Low Temp. Phys.*, 17 (1991) 130.
- [129] R.S. Rubins and H.R. Fetterman, *J. Chem. Phys.*, 71 (1979) 5163.
- [130] P.M. Champion and A.J. Sievers, *J. Chem. Phys.*, 66 (1977) 1819.
- [131] P.M. Champion and A.J. Sievers, *J. Chem. Phys.*, 72 (1980) 1569.
- [132] C. Butzlaff, A.X. Trautwein and H. Winkler, *Methods Enzymol.*, 227 (1993) 412.
- [133] C.J. O'Connor, *Prog. Inorg. Chem.*, 29 (1982) 203.
- [134] E.P. Day, *Methods Enzymol.*, 227 (1993) 437.
- [135] M.P. Hendrich, L.L. Pearce, L. Que, Jr., N.D. Chasteen and E.P. Day, *J. Am. Chem. Soc.*, 113 (1991) 3039.

- [136] M. Atta, C. Scheer, P.H. Fries, M. Fontecave and J.-M. Latour, *Angew. Chem. Int. Ed. Engl.*, 31 (1992) 1513.
- [137] L. Petersson, S. Slappendel and J.F.G. Vliegthart, *Biochim. Biophys. Acta*, 828 (1985) 81.
- [138] L. Petersson, S. Slappendel, M.C. Feiters and J.F.G. Vliegthart, *Biochim. Biophys. Acta*, 913 (1987) 228.
- [139] G.J. Long (ed.), *Mössbauer Spectroscopy Applied to Inorganic Chemistry*, Plenum Press, New York, 1984.
- [140] R. Zimmermann, B.H. Huynh, E. Münck and J.D. Lipscomb, *J. Chem. Phys.*, 69 (1978) 5463.
- [141] J.F. Gibson, in I. Bertini and R.S. Drago (eds.), *ESR and NMR of Paramagnetic Species in Biological and Related Systems*, D. Reidel, 1979, p. 225.
- [142] W.R. Hagen, *Biochim. Biophys. Acta*, 708 (1982) 82.
- [143] R. Cammack and C.E. Cooper, *Methods Enzymol.*, 227 (1993) 353.
- [144] E. Münck, K.K. Surerus and M.P. Hendrich, *Methods Enzymol.*, 227 (1993) 463.
- [145] M.P. Hendrich and P.G. Debrunner, *J. Mag. Res.*, 78 (1988) 133.
- [146] M.P. Hendrich and P.G. Debrunner, *Biophys. J.*, 56 (1989) 489.
- [147] A.B.P. Lever, *Inorganic Electronic Spectroscopy*, 2nd edn., Elsevier, Amsterdam, 1984.
- [148] B.A. Averill and J.B. Vincent, *Methods Enzymol.*, 226 (1993) 33.
- [149] R.S. Rubins and T.D. Black, *Chem. Phys. Lett.*, 81 (1981) 450.
- [150] L.C. Jackson, *Phil. Mag.*, 4 (1959) 269.
- [151] T. Ohtsuka, *J. Phys. Soc. Japan*, 14 (1959) 1245.
- [152] R. Doerfler, *J. Phys. C: Solid State Phys.*, 20 (1987) 2533.
- [153] J.S. Haynes, S.J. Rettig, J.R. Sams, R.C. Thompson and J. Trotter, *Can. J. Chem.*, 64 (1986) 429.
- [154] F.F. Charron, Jr. and W.M. Reiff, *Inorg. Chem.*, 25 (1986) 2786.
- [155] M. Tinkham, *Proc. R. Soc. (Lond.)*, A236 (1956) 535.
- [156] K.D. Hodges, R.G. Wollmann, E.K. Barefield and D.N. Hendrickson, *Inorg. Chem.*, 16 (1977) 2746.
- [157] D.J. Mackey, R.F. McMeeking and M.A. Hitchman, *J. Chem. Soc. Dalton Trans.*, (1979) 299.
- [158] B.W. Dockum and W.M. Reiff, *Inorg. Chim. Acta*, 120 (1986) 61.
- [159] P.R. Edwards, C.E. Johnson and R.J.P. Williams, *J. Chem. Phys.*, 47 (1967) 2074.
- [160] F.A. Cotton and M.D. Meyers, *J. Am. Chem. Soc.*, 82 (1960) 5023.
- [161] C.D. Burbridge and D.M.L. Goodgame, *Inorg. Chim. Acta*, 4 (1970) 231.
- [162] B.F. Little and G.J. Long, *Inorg. Chem.*, 17 (1978) 3401.
- [163] V.L. Goedken, P.H. Merrell and D.H. Busch, *J. Am. Chem. Soc.*, 94 (1972) 3397.
- [164] M. Ciampolini and N. Nardi, *Inorg. Chem.*, 5 (1966) 1150.
- [165] F. Mani and G. Scapacci, *Inorg. Chim. Acta*, 38 (1980) 151.
- [166] M. Ciampolini and G.P. Speroni, *Inorg. Chem.*, 5 (1966) 45.
- [167] D. Forster and D.M.L. Goodgame, *J. Chem. Soc.*, (1965) 268.
- [168] J.V. Quagliano, A.K. Banerjee, V.L. Goedken and L.M. Vallarino, *J. Am. Chem. Soc.*, 92 (1970) 482.
- [169] C. Furlani, E. Cervone and V. Valenti, *J. Inorg. Nucl. Chem.*, 25 (1963) 159.
- [170] R.G. Burns, M.G. Clark and A.J. Stone, *Inorg. Chem.*, 5 (1966) 1268.
- [171] P.J. Stephens, *Annu. Rev. Phys. Chem.*, 25 (1974) 201.
- [172] S.B. Piepho and P.N. Schatz, *Group Theory in Spectroscopy: With Applications to Magnetic Circular Dichroism*, John Wiley, New York, 1983.
- [173] A.D. Buckingham and P.J. Stephens, *Annu. Rev. Phys. Chem.*, 17 (1966) 399.
- [174] P.J. Stephens, *J. Chem. Phys.*, 52 (1970) 3489.
- [175] P.J. Stephens, *Adv. Chem. Phys.*, 35 (1976) 197.
- [176] S.F. Mason, *Molecular Optical Activity and the Chiral Discriminations*, Cambridge University Press, Cambridge, 1982.
- [177] W.R. Browett, A.F. Fucaloro, T.V. Morgan and P.J. Stephens, *J. Am. Chem. Soc.*, 105 (1983) 1868.
- [178] P.J. Stephens, G.M. Jensen, F.J. Devlin, T.V. Morgan, C.D. Stout, A.E. Martin and B.K. Burgess, *Biochemistry*, 30 (1991) 3200.
- [179] J.C. Collingwood, P. Day and R.G. Denning, *J. Chem. Soc. Faraday Trans.*, 269 (1973) 591.
- [180] G.A. Osborne, J.C. Cheng and P.J. Stephens, *Rev. Sci. Instrum.*, 44 (1973) 10.
- [181] A.F. Drake, *J. Phys. E: Sci. Instrum.*, 19 (1986) 170.
- [182] A.L. Companion and M.A. Komarynsky, *J. Chem. Educ.*, 41 (1964) 257.

- [183] S. Pulver, W.A. Froland, B.G. Fox, J.D. Lipscomb and E.I. Solomon, *J. Am. Chem. Soc.*, 115 (1993) 12409.
- [184] R.S. Berry, *J. Chem. Phys.*, 32 (1960) 933.
- [185] M. Gerloch, *Magnetism and Ligand-Field Analysis*, Cambridge University Press, Cambridge, 1983.
- [186] P.N. Schatz, R.L. Mowery and E.R. Krausz, *Mol. Phys.*, 35 (1978) 1537.
- [187] D.E. Bennett and M.K. Johnson, *Biochim. Biophys. Acta*, 911 (1987) 71.
- [188] Y. Zhang, M.S. Gebhard and E.I. Solomon, *J. Am. Chem. Soc.*, 113 (1991) 5162.
- [189] J.M. McCormick, R.C. Reem and E.I. Solomon, *J. Am. Chem. Soc.*, 113 (1991) 9066.
- [190] A.J. Thomson and M.K. Johnson, *Biochem. J.*, 191 (1980) 411.
- [191] C.L. Hamilton, R.A. Scott and M.K. Johnson, *J. Biol. Chem.*, 264 (1989) 11605.
- [192] C. Corliss and J. Sugar, *J. Phys. Chem. Ref. Data*, 11 (1982) 135.
- [193] J.S. Griffith, *The Theory of Transition-Metal Ions*, Cambridge University Press, Cambridge, 1964.
- [194] M. Ciampolini, *Struct. Bond.*, 6 (1969) 52.
- [195] J.S. Wood, *Prog. Inorg. Chem.*, 16 (1972) 277.
- [196] J.S. Wood and P.T. Greene, *Inorg. Chem.*, 8 (1969) 491.
- [197] F. Hartmann-Boutron and P. Imbert, *J. Appl. Phys.*, 39 (1968) 775.
- [198] F. Varret and F. Hartmann-Boutron, *Ann. Phys.*, 3 (1968) 157.
- [199] A. Pabst, *Am. Mineral.*, 28 (1943) 372.
- [200] D.L. Sloane, M.F. Browner, Z. Dauter, K. Wilson, R.J. Fletterick and E. Sigal, *Biochem. Biophys. Res. Commun.*, 173 (1990) 507.
- [201] E. Sigal, *Am. J. Physiol.*, 260 (1991) L13.
- [202] J.-P. Hénichart, J.-L. Bernier, R. Houssin, M. Lohez, A. Kenani and J.-P. Catteau, *Biochem. Biophys. Res. Commun.*, 126 (1985) 1036.
- [203] T. Sugiyama, M. Ohno, M. Shibasaki, M. Otsuka, Y. Sugiura, S. Kobayashi and K. Maeda, *Heterocycles*, 37 (1994) 275.
- [204] M. Muetterties, P.K. Mascharak, M.B. Cox and S.K. Arora, *Inorg. Chim. Acta*, 160 (1989) 123.
- [205] Y.-D. Wu, K.N. Houk, J.S. Valentine and W. Nam, *Inorg. Chem.*, 31 (1992) 718.
- [206] S.J. Brown, M.M. Olmstead and P.K. Mascharak, *Inorg. Chem.*, 29 (1990) 3229.
- [207] H.E. Toma and J.M. Malin, *Inorg. Chem.*, 12 (1973) 1039.
- [208] J. Hine, *Physical Organic Chemistry*, 2nd edn., McGraw-Hill, New York, 1962.
- [209] B.J. Tabner and J.R. Yandle, *J. Chem. Soc. (A)*, (1968) 381.
- [210] K.K. Innes, I.G. Ross and W.R. Moomaw, *J. Mol. Spectrosc.*, 132 (1988) 492.
- [211] R. Benedix and H. Hennig, *J. prakt. Chem.*, 326 (1984) 962.
- [212] H.H. Jaffé and M. Orchin, *Theory and Applications of Ultraviolet Spectroscopy*, John Wiley, New York, 1962.
- [213] D.K. Lavalley and E.B. Fleischer, *J. Am. Chem. Soc.*, 94 (1972) 2583.